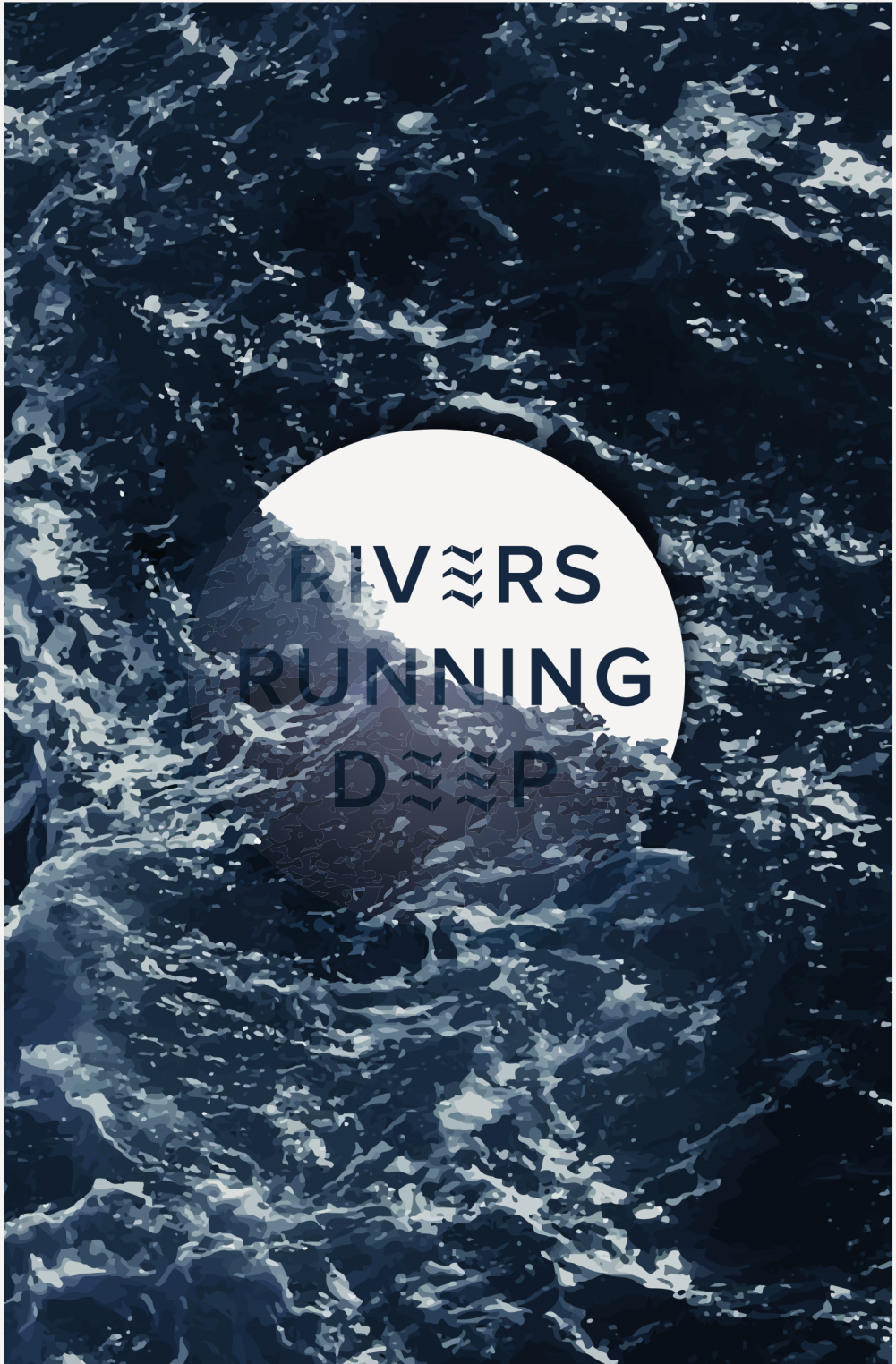


Complex flow and morphology
in the Mahakam River, Indonesia



BART
VERM
EULEN

Rivers running deep

COMPLEX FLOW AND MORPHOLOGY IN THE MAHAKAM RIVER,
INDONESIA

Bart Vermeulen

Thesis committee

Promotor

Prof. Dr R. Uijlenhoet
Professor of Hydrology and Quantitative Water Management
Wageningen University

Co-promotor

Dr A.J.F. Hoitink
Associate professor, Hydrology and Quantitative Water Management
Wageningen University

Other members

Prof. Dr J. Wallinga, Wageningen University
Prof. Dr S.J.M.H. Hulscher, University of Twente, Enschede
Dr K. Blanckaert, Chinese Academy of Sciences, China &
École Polytechnique Fédérale de Lausanne, Switzerland
Dr J.G. Venditti, Simon Fraser University, Burnaby, Canada

This research was conducted under the auspices of the Graduate School for Socio-Economic and Natural Sciences of the Environment (SENSE).

Rivers running deep

COMPLEX FLOW AND MORPHOLOGY IN THE MAHAKAM RIVER,
INDONESIA

Bart Vermeulen

Thesis

submitted in fulfillment of the requirements for the degree of doctor
at Wageningen University
by the authority of the Rector Magnificus
Prof. Dr M.J. Kropff,
in the presence of the
Thesis Committee appointed by the Academic Board
to be defended in public
on Monday 8 December 2014
at 1.30 p.m. in the Aula.

B. Vermeulen

Rivers running deep – Complex flow and morphology in the Mahakam River, Indonesia,

v+154 pages.

PhD thesis, Wageningen University, Wageningen, NL (2014)

With references, with summary in Dutch and English

ISBN 978-94-6257-206-5

Contents

Contents	v
Introduction	1
Multi-scale structure of meanders	15
Sharp bends associated with deep scours	27
Improved flow velocity measurements	53
Flow in a sharp and wide bend	73
Reynolds stress profiles from Coupled ADCPs	91
Bed shear stress monitoring with an HADCP	105
Synthesis	119
Bibliography	125
Acknowledgments	139
Summary	143
Samenvatting	147

Introduction

1.1 Motivation

Rivers have always attracted and sustained life thanks to the availability of water, the fertility of the surrounding soils and their capacity to transport sediments, nutrients, plants and animals. These benefits, however, come at the price of exposure to river induced catastrophes. Floods, soil erosion, and contamination of drinking and irrigation water by salt water can cause great damage to plants, animals and humans. Proper management of rivers is therefore essential to sustain life, and the large number of functions rivers fulfill calls for a solid and reliable knowledge base. Managers and decision makers often rely on predictions of a river system's reaction to human induced or natural changes. Knowledge of rivers is derived from observations of their behavior, which subsequently forms the basis for the development of models useful for engineers and decision makers. Our ability to manage rivers is therefore strongly related to the extent to which we are able to observe and quantify their functioning.

The trouble with the management of natural rivers is that predicting their response to human or natural change is an under-constrained problem, which involves a large number of interrelated variables (Montgomery, 1997). Emergent behavior in rivers, such as mean-

dering, bed-forms, or rates of lateral erosion (Werner, 1999; Hooke, 2003), is very difficult to predict and results from the complex interaction of processes including turbulence, secondary flow and sediment transport. Emergent phenomena are easily observed in the field and their behavior can be captured in empirical relations useful for engineering purposes. The underlying detailed processes are often much harder to observe in the field, due to complex interactions and the lack of instruments and methods that allow to detect small scale processes in large scale systems. Reduced complexity laboratory studies and small-scale field studies have enabled the observation of detailed processes, through the reduction of complexity. These experiments lead to mechanistic descriptions of turbulence, sediment transport and secondary flow, but it is often difficult to translate these results to large, natural rivers, for which we lack the relevant field data.

The aim of the present thesis is to *quantify and understand flow and morphological processes in a river with a complex geometry, by using and improving state-of-the-art measuring and modeling techniques*. This may bridge the gap between experimental laboratory studies, in which the complexity of a problem is reduced, and the empirical field observations of complex phenomena, in which the underlying physical mechanisms are often difficult to unravel.

1.2 Complex river flow and morphology

Complex flow and morphology in rivers result from an intricate interaction of basic processes. In what follows, a brief overview is given of several fundamental processes occurring in rivers, hinting at how they interact. Subsequently, these processes are discussed in more detail for river bends, which form a central topic throughout the rest of this thesis.

Temporal decomposition: mean flow and turbulence

Complex flow in rivers results from the interaction between flowing water and the ambient morphology. The bed and the banks of a river resist the flow, generating fluctuating behavior of the flow known as turbulence. To ease the analysis and modeling of turbulent flow, the flow is generally decomposed in mean flow and turbulence, known as the Reynolds decomposition. This decomposition is based on the

duration and extent of fluctuations in the flow. If we observe a flow for a short period, the flow is very complex, with vortices, boils, etc. – turbulence –, while if we observe it for a longer period the water will be mainly flowing in the same direction with the same velocity – mean flow –. The mean flow “feels” turbulence as viscosity and loses energy to it. Turbulent vortices “extract” this energy from the mean flow. Large vortices create smaller vortices, transferring energy from large to very small vortices, where the energy is transformed into heat by molecular viscosity. This may sound as a one-way process in which mean flow loses energy, which is eventually lost as heat, but in reality turbulence and the main flow interact, creating complex three-dimensional flow structures.

Spatial decomposition: main flow and secondary flow

Complex three-dimensional structures are difficult to analyze and describe as such. For this reason, the flow is often decomposed into main flow and secondary flow. In rivers the water dominantly flows in one direction, i.e. downstream. This direction, although not always easily defined, is called the main flow direction¹. The main flow is usually characterized by a variable velocity throughout the cross-section. Near the boundaries, the flow tends to weaken, while it is strongest further away from the boundaries. Secondary flow refers to the flow across the main flow, i.e. toward the banks and vertical. Two types of secondary flow can be distinguished based on the processes that generate them. Prandtl’s first kind of secondary flows are directly induced by the channel geometry. Prandtl’s second kind of secondary flows are induced by turbulence. The main flow, secondary flow and turbulence interact in ways determined mainly by the geometry of a channel.

Flow in sharp meander bends

Complex flows in rivers are generally classified based on the governing geometries: bends, compound channels, scours, junctions, human structures, bed-forms, vegetation, etc. Other complex flows are the consequence of forcing factors such as tides, density driven flows,

¹Several definitions can be given for the direction of main flow, e.g. based on the thalweg, the river centerline or the cross-section averaged velocity direction.

etc. To elucidate how complex flows are the consequence of intricate interactions between the processes described above we will provide a brief overview of the present knowledge on the functioning of river bends, which are extensively treated in this thesis.

Crucial in river bends is the development of a spiral motion of the flow (Figure 1.1). This spiral motion is primarily generated by

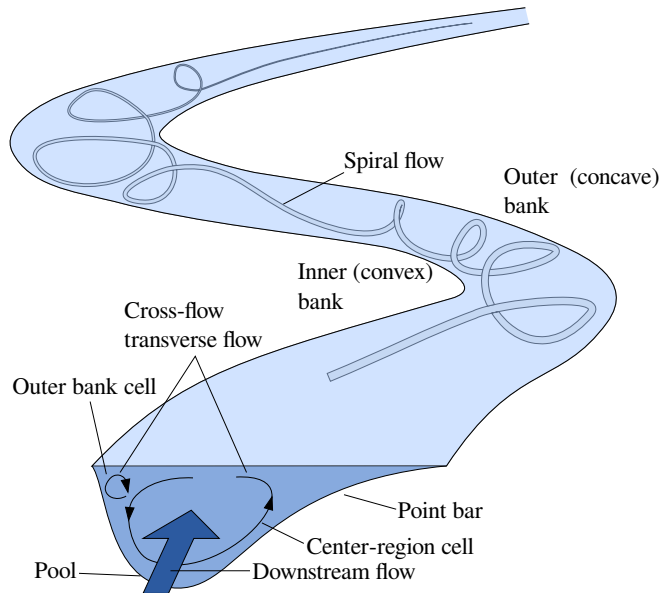


FIGURE 1.1. Spiral motion in a meander bend

an imbalance between the cross-stream pressure gradient and the effect of the centrifugal force. The spiral flow is a secondary flow of Prandtl's first kind, since it is directly induced by the geometry of the channel. The outward motion near the water surface pushes the core of the flow (high downstream momentum) to the outer bank, where the flow accelerates. The inward motion near the bed steers flow with low velocity (low downstream momentum) to the inner bank, where the flow decelerates.

High flow velocity near the outer bank induces erosion and low flow velocity in the inner bank causes deposition. The deep part near the outer bank is called a "pool" and the shallow part at the inner

bank is called a “point bar”. Active river bends tend to gradually sharpen. As bends sharpen, the flow adjusts and flow patterns can change dramatically.

Laboratory studies (Dietrich & Smith, 1983; Blanckaert & Graf, 2001; Abad & Garcia, 2009a,b; Constantinescu et al., 2013) have shed light on the adaptation of the flow patterns in response to bend sharpening. The spiral motion is strengthened as the bend sharpens, but at some point this process saturates. The cross-stream flow starts to significantly influence the downstream flow, slowing it down and forcing the core of the flow to the bed. Lower velocity at the surface will result in weakening of the secondary flow (Blanckaert & de Vriend, 2004).

Next to the main spiral flow, a small circulation cell is often observed near the outer bank. This outer bank cell is generated by other processes than those generating the main spiral flow. Next to the centrifugal force, turbulence is an important forcing contributing factor² (Secondary flow of Prandtl’s second kind). This small outer bank cell may play a crucial role in the morphological development of sharp bends, since it influences the stability of the outer bank and protects it from the direct impact of strong downstream flow (Blanckaert, 2011).

The combined effect of saturation of the main recirculation cell and the action of the outer bank cell provides a possible explanation for an emerging phenomenon that has been observed well before the flow in sharp bends had been analyzed in great detail. Hickin & Nanson (1984) and Hooke (2003) found that lateral migration rates of rivers increase with increasing channel curvature. At high curvatures, migration rates drop again. Field observations taken in inactive, sharp meander bends are required to confirm the processes observed in flume experiments may indeed relate to the ossification of high-curvature meander bends.

Non-harmonic meanders

In sharp bends the cross-sectional area is often large (Blanckaert, 2010), and in several field studies this local increase can even be

²This shows that turbulence is not only dissipating energy from the flow, but sometimes also supplies the main flow with energy.

termed dramatic (Andrle, 1994; Beltaos et al., 2012). Several studies have reported bends in which deposition occurs near the outer bank (Woodyer, 1975; Page & Nanson, 1982; Hickin, 1986; Makaske & Weerts, 2005). Sometimes, bends also tend to develop a non-harmonic shape. This behavior is often observed in tropical lowland rivers. The middle Fly River, Papua New Guinea, flows first in a forested region where characteristic harmonic meander shapes are observed. Downstream of this region, the river reaches a low-slope swamp region where meanders become dogleg shaped, with long straight reaches connected by sharp bends (Dietrich et al., 1999). In this swampy region lateral migration is almost absent and the river appears to be frozen (Dietrich et al., 1999). Similar non-harmonic meanders have also been observed along lowland sections of the Purus and the Juruá Rivers with very high suspended load (Latrubesse et al., 2005). Non harmonic-meanders are also known from temperate regions, where they are found in small, low stream-power systems, often featuring a strong increase in cross-sectional area (Andrle, 1994) and, like in the Fly River, low lateral migration rates. Such observations clearly challenge our current mechanistic understanding of river bends. What does this all mean for our current river management practices?

Nowadays, river management strongly relies on the use of computational models to predict changes in river systems. Ideally, one would use the most detailed model, assuming this would lead to a proper description of the system. For rivers, this is still computationally too demanding, and therefore current operational models are reduced-complexity models. Such models resort to parameterizations for important processes that are lost during the model simplification. For bends this means that the effect of the spiral flow is included in one dimensional and two dimensional-horizontal models through a parameterization (Ottevanger et al., 2013). Such approach will allow to properly deal with bends that function according to the existing theory, but they will be unsuitable to predict the behavior of e.g. bends with a very large increase in cross-sectional area. Since the theory underlying reduced-complexity river flow models is mainly based on laboratory experiments and field observations taken in small streams, the question arises whether they are suitable to predict the behavior of large rivers.

Measuring complex flow and turbulence in large rivers

Improving our understanding and translating this into computational models suitable to predict the behavior of large rivers requires the ability to observe fundamental aspects of the flow and morphology of large scale systems in detail. Over the past decades, the development of new measuring techniques has paved the way for new discoveries in the field of geophysical flows. The development of measuring equipment for laboratory applications, starting around 1970, opened up new possibilities for the study of turbulence in open channel flows. This has lead to extensive investigations of turbulence under a great variety of hydrodynamic conditions (Nezu, 2005) and has strongly improved our understanding of turbulence in open channel flow. Similarly, the development of acoustic techniques for flow measurements has opened up the possibilities to investigate complex flows and turbulence in the field, mainly in small streams (Sukhodolov, 2014). The deployment of acoustic profilers in laboratory experiments has provided a wealth of information on flow in sharp bends (Blanckaert & de Vriend, 2004) and can currently be used to study flow and sediment transport near dunes (Naqshband et al., 2014).

The introduction of acoustic Doppler current profilers (ADCPS) has greatly improved our ability to monitor flow in rivers and the coastal ocean. These instruments have been applied successfully, mainly to monitor mean flow patterns (Muste et al., 2004a,b; Dinehart & Bureau, 2005b; González-Castro & Muste, 2007; Jamieson et al., 2011; Buschman et al., 2013; Sassi et al., 2013) and to monitor discharge (Nihei & Kimizu, 2008; Le Coz et al., 2008; Hoitink et al., 2009; Sassi et al., 2011b; Hidayat et al., 2011). ADCPS can also be used to monitor sediment transport (Reichel & Nacithnebel, 1994; Rennie et al., 2002; Hoitink & Hoekstra, 2005; Sassi et al., 2012; Moore et al., 2012) and to monitor turbulence, finding widest application in estuaries and in the coastal ocean (Lohrmann et al., 1990; Stacey et al., 1999a,b; Lu & Lueck, 1999a,b; Rippeth et al., 2002; Souza et al., 2004; Williams & Simpson, 2004; Peters & Johns, 2006; Whipple et al., 2006; Tarya et al., 2010). The use of ADCPS to measure turbulence is not straightforward, since the instrument measures flow velocity with diverging acoustic beams. The use of the so called “variance method” allows to process raw ADCP data in such a way that turbulence properties can

be retrieved from them. This method, however, cannot be applied under highly stratified conditions, common in the coastal environment. Fluvial environments are rarely affected by stratification and can offer better conditions to apply the variance method. The method, though, has rarely been used in a fluvial context. While stratification rarely occurs in fluvial systems, the smaller scale of rivers compared to the coastal environment might be a problem for ADCP measurements of both flow and turbulence. Large spatial gradients in the flow question the assumptions of flow homogeneity between the acoustic beams (Marsden & Ingram, 2004), which is however widely applied.

1.3 Study Area

Fluvial systems in tropical regions include several of the largest rivers in the world, yet the knowledge base on tropical systems is still limited (Latrubesse et al., 2005). Understanding complex flow and morphology in tropical rivers is essential for ecologists, geologists, decision makers, and engineers which now base themselves on models and concepts from Northern Hemisphere, temperate region systems (Latrubesse et al., 2005). Non-Harmonic meanders (Dietrich et al., 1999; Latrubesse et al., 2005), deep scours (Best & Ashworth, 1997), bifurcating meander bends (Grenfell et al., 2012), and embayments (Darby et al., 2010) are only some examples of morphological features and processes omnipresent in the Tropics that challenge our current understanding of fluvial systems. Tropical rivers are thus particularly suited to study complex river behavior, and in turn, the understanding gained from such a study would be particularly relevant in tropical regions.

The present thesis focusses on the Mahakam River, located in East Kalimantan, Indonesia (Figure 1.2). The Mahakam River flows from the inland mountains of Borneo, through the Tertiary rocks of the Kutei Basin. The river then flows through the Kutei lakes area, which is a very flat, subsiding region, in which thick packs of Quaternary sediments are deposited. The latter area features several lakes and peat bogs, and inundates frequently. The Mahakam meets four of its main tributaries here. Downstream of the Kutei lakes area, the Mahakam flows through a Tertiary mountain range before reaching

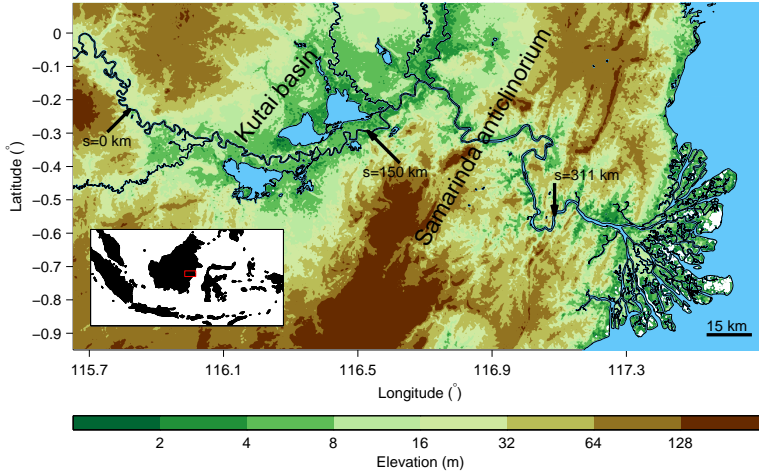


FIGURE 1.2. Overview of the study area. The red rectangle in the inset shows the extent of the map. Elevations are based on SRTM data and are presented in logarithmically spaced contours, to highlight the elevation differences in the lowland areas.

the Mahakam delta.

The lakes play an important role in regulating water and sediment discharge eventually issued to the delta (Storms et al., 2005; Sassi et al., 2011a, 2012; Hidayat et al., 2012). Tie-channels (Rowland, 2007) connecting the lakes to the river regulate the exchange and, depending on the discharge of the river, carry water from the lakes into the river or vice-versa, functioning as a discharge buffer (Hidayat et al., 2011). There are two main lakes north of the river: Lake Semayang and Lake Melintang. Lake Semayang, the easternmost lake, is connected to the river through a tie-channel. Lake Melintang, the westernmost lake is connected on the east side to Lake Semayang while in the south it connects to the river through a small, 10-15 meters wide channel. A third lake, called Lake Jempang, connects to the river through a large tie-channel on the east side, and a small 2-3 meters wide tie-channel on the northern side. The lakes are surrounded by several peat domes with a diameter of around 35 km. These domes are considered to contribute to the discharge buffering capacity (Hidayat et al., 2012), as they can store large amounts

of water. During floods, as much as 91% of the Kutei lakes area is inundated, while during low flows only 12% is inundated (Hidayat et al., 2012).

Proper management of the Mahakam River is crucial, given the increasing number of floods in the city of Samarinda. Engineering works may be needed to prevent land loss due to bank erosion and to sustain timber production, coal mining and shrimp farming, that make the Kutei district the richest in Indonesia (Simarmata, 2010). The Mahakam River is also home to some critically endangered species including the Irrawaddy dolphin (Kreb & Budiono, 2005), and the White-shouldered ibis (Sözer & Nijman, 2005).

1.4 Objectives and research questions

Quantify meander shape properties (Chapter 2)

The planform of the Mahakam River shows to be markedly different from many other rivers, featuring sharp bends and multiple loops interspersed by straight reaches. Objective quantification of the anomalous behavior of meander shape is a particularly challenging task. The preferred approach is not based on any subjective choice, it can deal with non-uniformity in the planform and it allows to characterize multiple spatial scales. This is particularly important when dealing with large tropical rivers, that often cross very different environments (Latrubesse et al., 2005; Ashworth & Lewin, 2012). Several studies have attempted to objectively quantify river shape (O'Neill & Abrahams, 1986; Howard & Hemberger, 1991; Andrieu, 1996; Marani et al., 2002). The methods, however, often involve subjective steps, assumptions of uniformity, do not account for multiple scales in the meandering process and often do not have any metrics to quantify non-harmonic behavior.

Research questions

- How can we objectively quantify meander shape?
- Which parameter is able to capture non-harmonic bend behavior?
- Is it possible to capture the multi-scale structure of meandering in a simple way?

- How can we effectively visualize the multi-scale behavior of meanders?

Investigate if planform geometry relates to scour in the Mahakam River (Chapter 3)

Tropical rivers can sometimes develop extremely deep scours (Best & Ashworth, 1997) which can reach up to five times their average depth. The Mahakam River is no exception to this. The functioning of autogenic scours and their development as a product of flow processes is poorly understood. In tropical rivers this phenomenon is rarely observed. In moderate climate regions deep scours have been found in small streams in non-harmonic sections called circular meander pools, where the flow often recirculates (Andrle, 1994; Hodskinson & Ferguson, 1998; Nanson, 2010). In large rivers, such scours have only been observed in a sharp bend in the Mackenzie delta (Gharabaghi et al., 2007; Beltaos et al., 2012).

Research questions

- Where does scour occur along the Mahakam river?
- How does scour relate to planform curvature?
- At what rate is the Mahakam river migrating?
- How do the scours and the planimetry relate to geomorphology, land cover and vegetation?
- Are there any morphological regime changes along the Mahakam River?
- How large is the meander belt of the Mahakam?

Improve mean flow measuring techniques (Chapter 4)

The processes shaping autogenic scours in large rivers are poorly understood. This is partly related to the difficulty to study the flow at such depths. Acoustic Doppler Current Profilers (ADCPS) are acoustic instruments which can measure flow at large distance from the sensor with a high spatial and temporal resolution. One of the main shortcomings of standard ADCP processing is the need to assume homogeneous flow between the acoustic beams. This widely applied assumption (Marsden & Ingram, 2004; Kawanisi, 2004; Kim et al., 2009; Le Bot et al., 2011; Parsons et al., 2013; Tokyay et al., 2009;

Muste et al., 2010; Nystrom et al., 2007; Gargett, 1994) is likely to fail, especially in large systems with deep scours.

Research questions

- Is it possible to estimate mean flow from ADCP measurements without assuming flow homogeneity between the beams?
- How can mean flow, turbulence and noise in ADCP data best be separated?
- How many repeat transects are needed to separate mean flow and turbulence?

Enhance understanding of flow in sharp bends (Chapter 5)

Several studies have shown that a large increase in cross-sectional area in a bend often leads to the development of horizontal flow separation. Existing criteria to predict the possibility of horizontal flow separation are based on the generation of a longitudinal adverse slope at the water surface (Blanckaert, 2010). This adverse slope is created in bends as a result of transverse tilting of the water surface. For a given curvature, the transverse water surface will stabilize at some slope such that the centrifugal force is balanced. When curvature increases, the transverse slope increases as well, causing a decrease of the longitudinal water surface gradient at the outer bank. This may eventually lead to an adverse gradient, and possibly to horizontal flow separation. Such a separation occurs in several bends along the Mahakam River.

Research questions

- What does the flow pattern look like in sharp bends of the Mahakam?
- Which are the main drivers of the observed flow pattern?
- Is it possible to model the flow patterns using a state of the art computational model?

Improve turbulence measuring techniques (Chapter 6 and Chapter 7)

In sharp bends, turbulent stresses are known to play a crucial role in the generation of secondary flow patterns (Blanckaert & de Vriend,

2004). In particular the outer bank cell is strengthened by turbulence anisotropy (Blanckaert & de Vriend, 2004). Studies quantifying these effects are rare due to the difficulty to measure Reynolds stresses, particularly in large scale flows. Bottom mounted ADCPs allow to process the raw data, using a technique called the variance method, to obtain estimates of the Reynolds stresses (Lohrmann et al., 1990; Stacey et al., 1999a; Lu & Lueck, 1999a). This technique, however, only delivers three of the six independent terms in the Reynolds stress tensor, requiring assumptions on turbulence anisotropy ratios to estimate turbulent kinetic energy and to study effects of gradients in turbulence stresses.

Research questions

- Which measuring strategy can be used to obtain all six terms in the Reynolds stress tensor?
- How do turbulence measurements from large rivers compare with results from laboratory and small scale field experiments?
- How do existing boundary layer models perform in large rivers?

1.5 Thesis outline

Chapter 2 introduces a new method to quantify the shape of the plan-form of a river, using a wavelet based, non-uniform approach. The morphology of the Mahakam is explored in Chapter 3. In Chapter 4, a novel technique to process ADCP data is presented, which allows to reduce the extent over which the flow needs to be assumed homogeneous. The novel technique is particularly suited to monitor flow in deep scours. The flow in a sharp bend, where the cross-sectional area increases dramatically, is studied in Chapter 5 based on detailed flow measurements combined with results from Large Eddy Simulations. Chapter 6 presents a novel technique which allows profiling all terms in the Reynolds stress tensor using two coupled ADCPs. In Chapter 7 a calibrated boundary layer model, previously used for discharge estimates (Sassi et al., 2011b), is now applied to estimate time series of bed-shear stress profiles, which yields insight into the temporal dynamics of the forcing functions of river morphological change.

Multi-scale structure of meanders

Abstract

River meander planforms can be described based on wavelet analysis, but an objective method to identify the main characteristics of a meander planform is yet to be found. Here we show how a set of simple metrics representing meander behavior can be retrieved from a continuous wavelet transform of a planform geometry. We construct a synoptic multiple looping forest to establish the meander structure, revealing the embedding of dominant meander scales in larger-scale loops. The method can be applied beyond the case of rivers, to unravel the meandering structure of lava flows, turbidity currents, tidal channels, rivulets, supra-glacial streams and extraterrestrial flows.

2.1 Introduction

Meandering is a common geophysical process that is often described in fluvial context, while it can be the consequence of a wide variety

This chapter is based on: B. VERMEULEN, A.J.F. HOITINK, G. ZOLEZZI, J. ABAD & R. AALTO, Multiscale structure of meanders

of processes occurring on earth, including (submarine) lava flows (Fornari, 1986), submarine turbidity-currents (Peakall et al., 2000; Abreu et al., 2003; Kolla et al., 2007), tidal channels (Marani et al., 2002), rivulets (Le Grand-Piteira et al., 2006), supra-glacial streams (Karlstrom et al., 2013) and on the surface of other planets in the solar system (Greeley, 1971; Komatsu & Baker, 1994; Baker, 2001; Malin & Edgett, 2003). Several underlying processes and principles governing meander shape have been proposed and may include: self-organization (Hooke, 2007), flow dynamics (Seminara, 2006), directed Brownian walk (Lazarus & Constantine, 2013), heritage from older geomorphological forms (Harden, 1990) and substrate heterogeneity (Güneralp & Rhoads, 2011). The large complexity and variety of meandering makes the task of unraveling the genesis and functioning of these features a challenging one.

The parametric description of meander shape is an important challenge in geomorphology (Schumm, 1967), environmental engineering (Rinaldi & Johnson, 1997) and climate studies (Stark et al., 2010). The complexity of a meander train is reflected in upstream or downstream skewness (Parker et al., 1983; Seminara & Tubino, 2001; Marani et al., 2002; Güneralp & Rhoads, 2011), fattening (Parker et al., 1982, 1983), curvature peaks (Chapter 3), compound loops (Brice, 1974; Frothingham & Rhoads, 2003; Hooke, 2003) and double headings (Thompson, 1986). Descriptive studies of river meanders tend to classify individual meander bends on subjective grounds, restricting the analysis to meander bends with a clear topology. Signal processing techniques can objectively characterize the structure of a meander train at the scale of the entire planform.

Typical measures to characterize meanders are sinuosity and meander wavelength. In a multi-scale planform the value of sinuosity will depend on the scale at which the meandering feature is analyzed (Andrle, 1996). Determining meander wavelength involves the detection of inflection points of the planform (corresponding to zero crossings in curvature), which is a subjective process that can suffer from irregularities in meander shape and sampling of the planform (Andrle, 1996). An alternative approach is to consider the direction change of a planform at fixed distances (O'Neill & Abrahams, 1986). This methodology however is not able to appreciate processes at different scales. The angle change can also be observed at different scales (Andrle, 1996), but the neglect of non-stationarity remains.

The result of this latter technique is similar to what is obtained by applying Fourier Transforms to curvature series. This can be done on a meander by meander basis (Marani et al., 2002), which however involves the detection of inflection points first. The use of wavelets transforms of curvature series has been employed to qualitatively detect changes in meandering behaviour (van Gerven & Hoitink, 2009).

In this contribution we propose a quantitative method to study the planform shape of meandering features. The method (Section 2.2) consists of defining the curvature from which a continuous wavelet transform is computed and used as a basis to construct a scale-space tree. The scale-space tree is used to identify the local meander scale and location. Eventually the shape of the meanders is quantified by two parameters and the relation of the meanders with the larger scale features is identified. The method is tested on synthetic planforms (Section 2.3) and three rivers (Section 2.3) followed by conclusions (Section 2.4).

2.2 Method

Meander planforms are multi-scale, non-stationary features. Therefore they are analyzed on the basis of a continuous wavelet transform (CWT) of their curvature. Peaks in the wavelet spectrum are detected and hierarchically ordered in a tree. The tree is crossed from smallest to largest scales to identify the most powerful peaks that define the local scale and location of meanders. Detected meanders are linked to larger scale structures, or multiple-loops, through the tree. The wavelet spectrum at sub-meander scales characterizes meander shape that is quantified with two parameters: skewing and fattening.

Curvature

Given the x and y coordinates of a meander we non-dimensionalize these coordinates:

$$\hat{x} = \frac{x - x_0}{W}, \quad \hat{y} = \frac{y - y_0}{W} \quad (2.1)$$

where x_0 and y_0 are the starting x and y coordinates of the planform, respectively, and W is the average width of the meandering form. \hat{x} and \hat{y} can be expressed as a function of the distance along the

planform, non-dimensionalized with the width, $\hat{s} = s/W$. The non dimensional curvature (C) of the planform is the ratio of the width and the inverse of the local radius of curvature (R) and is computed as (Legleiter & Kyriakidis, 2006):

$$C = \frac{W}{R} = \frac{\frac{d\hat{x}}{d\hat{s}} \frac{d^2\hat{y}}{d\hat{s}^2} - \frac{d\hat{y}}{d\hat{s}} \frac{d^2\hat{x}}{d\hat{s}^2}}{\left(\left(\frac{d\hat{x}}{d\hat{s}} \right)^2 + \left(\frac{d\hat{y}}{d\hat{s}} \right)^2 \right)^{\frac{3}{2}}} \quad (2.2)$$

All planforms were sampled with a resolution of one fifth of the width, enough to appreciate smaller scale oscillations.

Continuous wavelet transform

A CWT of a spatial series of curvature represents a meander shape in terms of spectral density distributed over space and scale. The mother wavelet used in wavelet analysis sets the resolution of the spectrum (Torrence & Compo, 1998). Complex wavelet functions return amplitude and phase information, and are best suitable to reveal gradual variation of multiple harmonics, for example in a tidal signal (Sassi et al., 2011a). The real wavelet function used here to represent a meandering planform is based on a derivative of a Gaussian or “Mexican-hat” wavelet, which allows to capture abrupt changes between neighbouring meander bends.

Scale-space trees

The CWTs of the curvature series feature several local extremes, connected by ridges of high spectral density and surrounded by zero-crossing lines. Proceeding from larger to smaller scales, the number of zero-crossings increases at singular points, where a spectral region bounded by zero-crossings and lines of constant scale split into three or more regions at smaller scale (Figure 2.2a,b and Figure 2.4a).

From the decomposed CWT plane we construct a scale-space forest in a procedure based on graph theory (Witkin, 1984; Harris et al., 2008). The spectral regions are structured in rooted trees in which they are represented as interconnected nodes, located where the local spectral density peaks as detected using a hexagonal lattice (Kuijper,

2004). All regions are crossed in a loop from the largest to the smallest scales, to identify parent nodes and child nodes. Nodes found in unclaimed reaches are called root-nodes and nodes without child nodes are called “leaves” (Harris et al., 2008). The total of nodes and interconnections linked to a root node defines a scale-space tree, and the trees in a cwt plane occupy the scale-space forest.

Meander identification

An interconnected series of nodes from leaf to root in a space-scale tree is called a “branch”. For each branch the node with the highest corresponding spectral density is defined as the meander node. All parent nodes of the meander node are defined as multiple-loop nodes. When performing this for all branches in the cwt plane, a node can be identified as both a meander-node and a multiple-loop node, in overlapping branches. All nodes with a double identity give up their identity as a meander node. In branches where a meander node is redefined as a multiple-loop node, a new meander node is selected corresponding to the highest spectral density among the super-scale nodes in the branch. Again, this can result in nodes with a double identity. The procedure is repeated until all nodes have a single identity. The reaches corresponding to meander-nodes at the end of the iteration are defined as meander bends, with length equal to the scale of the meander-node.

Multiple looping tree

After removing all child nodes of the meander nodes from the scale space forest determined in Section 2.2, a multiple looping forest remains yielding a synoptic view on the multiscale meander structure. The branching complexity at any location along the original meander reach can be quantified by the Strahler number of the corresponding reduced tree. The multiple looping forest can be projected onto the meander planform to reveal the meander planform structure (Figure 2.4).

Meander shape parameterization

The Kinoshita function describes the development of the angle of the planform along the s coordinate and is given by:

$$\theta(s) = \theta_0 \cos \phi - \theta_0^3 (c_f \cos(3\phi) + c_s \sin(3\phi)) \quad (2.3)$$

in which θ_0 is the amplitude of the planform angle and $\phi = 2\pi s / \lambda_m$, where λ_m is a typical meander wavelength. The parameters c_f and c_s control fattening and skewing of the meander, respectively.

The curvature generated by the Kinoshita function reads:

$$\begin{aligned} C(s) &= W \frac{d\theta(s)}{ds} = \\ &= -\frac{2\pi W}{\lambda_m} \left(\theta_0 \sin \phi + 3\theta_0^3 (c_s f_S - c_f f_F) \right) \end{aligned} \quad (2.4)$$

where:

$$f_F = \sin(3\phi) \quad (2.5)$$

$$f_S = \cos(3\phi) \quad (2.6)$$

The peaks of curvature at the main scale occur for $\phi = \phi/2 + n\pi$ (Figure 2.1). The exact location of meander-nodes corresponds with the location of the meander apex. The third modes in Equation 2.4 define the shape of the meander. For a downstream skewed meander bend two peaks in the third mode occur at $\phi = 1/3\pi + n\pi$ and $\phi = 2/3\pi + n\pi$, with respectively an opposite and equal sign as the main mode peak (Figure 2.1). For upstream skewed meander bends, the signs of these peaks are reversed.

For fat meanders, two peaks occur at $\phi = 1/6\pi + n\pi$ and at $\phi = 5/6 + n\pi$, with equal sign as the main mode peak, and one peak at $\phi = \pi/2 + n\pi$, with opposite sign as the main mode (Figure 2.1). For meanders with a sharp bend, these peaks are reversed. The angularity of a meander is used here to refer to meanders that have previously been named as “dog leg shaped”, “male meanders” or “hairpin bends”.

A half-meander or meander bend spans a distance corresponding to half of the scale of the meander-node. The left side of this meander reach is assigned $\phi = 0$ and the right side $\phi = \pi$. The cwt plane

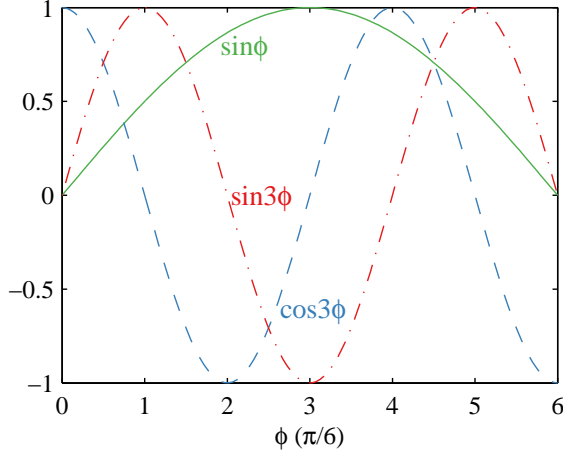


FIGURE 2.1. Trigonometric functions in Equation 2.4 generating the main meander mode (green, solid line) and two third modes to include fattening (red, dash-dotted line) and skewing (blue, dashed line) effects for $\phi \in [0, \pi]$.

at one third of the meander scale ($\Psi_s(\phi)$) defines the shape of the meander. Based on $\Psi_s(\phi)$ the shape parameters \mathcal{S} and \mathcal{F} are defined:

$$\mathcal{S} = \frac{|\Psi_s|_{\max}}{\Psi_m} \frac{\int_0^\pi \Psi_s f_{\mathcal{S}} d\phi}{\int_0^\pi f_{\mathcal{S}}^2 d\phi} \quad (2.7)$$

$$\mathcal{F} = \frac{|\Psi_s|_{\max}}{\Psi_m} \frac{\int_0^\pi \Psi_s f_{\mathcal{F}} d\phi}{\int_0^\pi f_{\mathcal{F}}^2 d\phi} \quad (2.8)$$

A positive \mathcal{S} corresponds to a downstream skewed meander, while a negative \mathcal{S} implies an upstream skewed meander. A positive \mathcal{F} corresponds to a fat meander, while a negative \mathcal{F} quantifies bend sharpness.

2.3 Results

Synthetic rivers

Kinoshita generated planforms obtained from equilibrium conditions of meander bends (Ikeda et al., 1981; Kinoshita, 1961) are considered to evaluate the performance of the shape parameters. Two planforms have been generated: one transitioning from upstream skewing to downstream skewing (Figure 2.2a), and one transitioning from fat meanders to angular meanders (Figure 2.2b). The wavelet spectra feature characteristic signatures typical for the different types of bends (Figure 2.2a,b). All half-meanders have the wavelet peak at a wavelength corresponding to the meander wavelength. The peaks have alternating sign, coinciding with a curving of the river to the right or to the left. At one third of the meander scale secondary peaks appear. For skewed and fat meanders there are always two equally signed peaks. For upstream skewed meanders a stronger peak is found at the upstream side, while for downstream skewed meanders this peak is found on the downstream side (Figure 2.2a). The location of the secondary peak for upstream or downstream skewed meanders always occurs at a fixed location with respect to the meander peak. This is a direct consequence of the phase-locking in the Kinoshita curve. The intensity of the secondary peaks increases for increasing skewness. Fat meanders feature two peaks with almost equal intensity at a fixed location (Figure 2.2b). The intensity of the peaks directly relates to the intensity of fattening. Sharply curved meanders with straight reaches in between feature one equally signed peak at the same location as the main meander peak (Figure 2.2b). Meanders in the central region of the two series have very low power in the secondary peaks.

Real world examples

The analysis is applied to the planform of three rivers: Red River, River Purus and River Mahakam. The Red River flows in a temperate region while the latter two in tropical regions. Most meanders in the three rivers are neither skewed nor fat (Figure 2.3). All three rivers have mostly upstream skewed meanders, but the Red River also has some downstream skewed ones. Fattening is strongest the Red River

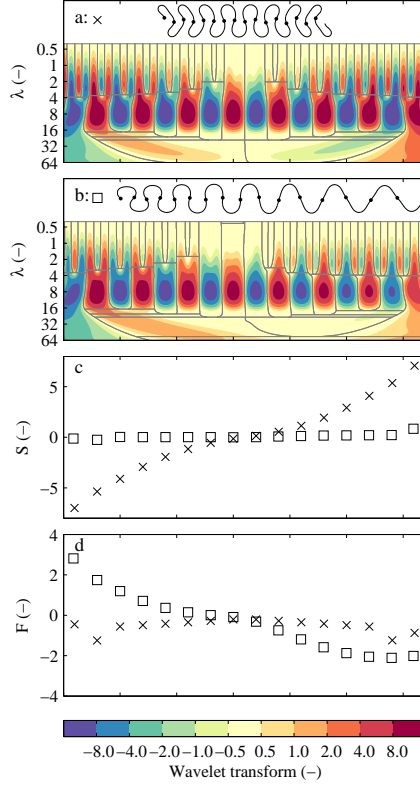


FIGURE 2.2. Two Kinoshita generated planforms, the first with gradual transition from upstream to downstream skewing (a) and the second one with gradual transition from fat meanders, to angular meanders (b). For both planforms the cwt is also shown as a contour. The vertical gray lines indicate the zero crossings of the cwt. The horizontal straight gray lines are the upper and lower boundaries of the scale-space intervals corresponding to the tree nodes. The two planforms are characterized in the bottom two panels and are represented by crosses and squares for the planforms in (a) and (b) respectively. The bottom two panels show the skewing parameter (c) and the fattening parameter (d).

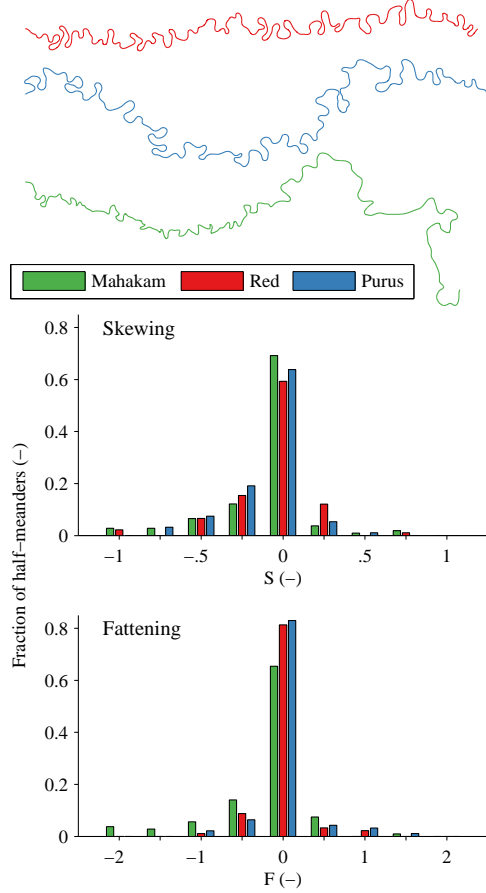


FIGURE 2.3. Histograms for the occurrence of skewing (a) and fattening (b) parameters for the Mahakam River (green), Red River (blue) and Purus River (red).

and the Purus River. Angularity (negative fattening) is strongest for the Mahakam River, which is known (Chapter 3) to feature sharp bends surrounded by relatively straight reaches (Figure 2.3).

The multiple looping forest for the Mahakam River shows the co-existent scales of looping (Figure 2.4). The largest-scale loop of the

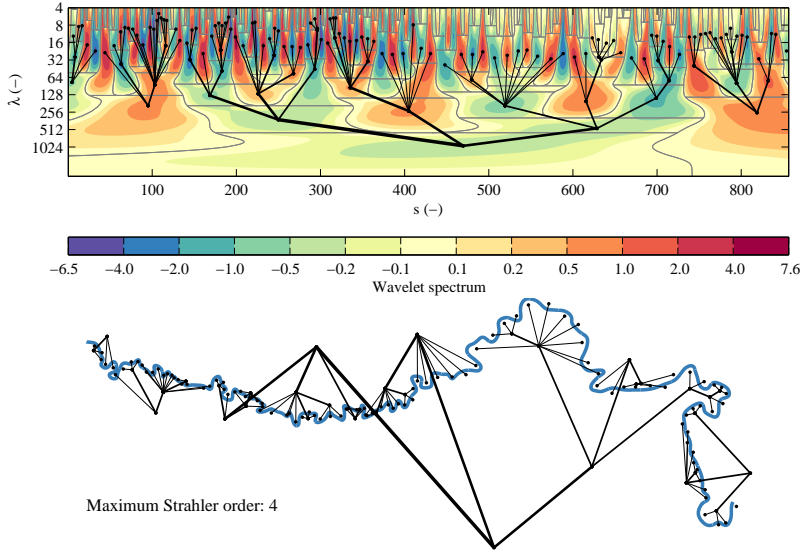


FIGURE 2.4. Multiple loop tree for the Mahakam River. In the top panel the multiple loop tree is displayed on top of the cwt it was derived from. The vertical gray lines indicate the zero crossings of the cwt. The horizontal straight gray lines are the upper and lower boundaries of the scale-space segments corresponding to the tree nodes. In the lower part the same tree is displayed in connection with the planform of the river. The position of each of the nodes is determined based on the corresponding scale and the center of curvature of the corresponding river reach. The width of the edges of the tree is based on the Strahler number.

Mahakam River can be interpreted as the valley axis curvature controlled by the local geology and land cover (Chapter 3). A multiple loop composed of only three meander bends can be interpreted as what is referred to as double heading (Thompson, 1986). The transition from a “fat” meander to a double headed meander is gradual. The corresponding classification depends on the scale at which the spectral density in the cwt plane is strongest. When the curvature peak of a minor head in a fat meander exceeds the peak at the meander scale, a new meander bend is established and the former meander bend becomes a multiple loop, featuring two bends.

2.4 Conclusions

In this contribution we address the lack of an objective, quantitative method to characterize meandering which is able to include the multi-scale nature and the non-stationarity of the phenomenon. The proposed method uses curvature series, which are analyzed by continuous wavelet analysis. Typical meander wavelength and intensity of the meandering are determined, along with three parameters that quantify the shape of the meanders: sharpness, fattening and angularity. The latter parameter is able to quantify the non-roundedness or ruggedness of meanders.

A tree is subsequently obtained for all super-meander scales, called the multiple loop tree. This tree describes the interrelation between all processes occurring at scales ranging from double-heading up to valley curvature. Each node in the tree connects to nodes at smaller scales and represents a curving feature in the planform. The end-nodes of the tree represent single half-meanders which are interrelated through larger scale features.

Sharp bends associated with deep scours

Abstract

Autogenic scouring in sharp river bends has received ample attention in laboratory and modelling studies. These studies have significantly advanced our understanding of how flow processes are influenced by strong curvature and how they affect the bathymetry. Here we present a 300 km reach of the Mahakam River in Indonesia, which features several sharp bends ($W/R > 0.5$), providing a unique field dataset to validate existing knowledge on sharp bends. Scour depths were found to strongly exceed what can be expected based on existing understanding of sharp bends, and are highly correlated with curvature. A comprehensive stream reconnaissance was carried out to compare the occurrence of sharp bends and deep scours with lateral bank migration. Histograms of the occurrence of erosive,

This chapter is based on: VERMEULEN, B., A. J. F. HOITINK, S. W. VAN BERKUM & HIDAYAT, 2014, Sharp bends associated with deep scours in a tropical river: the river Mahakam (East Kalimantan, Indonesia), *J. Geophys. Res.: Earth Surf.*, 119, 1–14, doi:10.1002/2013JF002923.

stable, advancing and bar-type banks as a function of curvature quantify the switch from a mildly curved bend regime to a sharp bend regime. In mild bends, outer banks erode and inner banks advance. In sharp bends the erosion pattern inverts. Outer banks stabilize or advance, while inner banks erode. In sharply curved river bends, bars occur near the outer banks that become less erosive for higher curvatures. Inner banks become more erosive for higher curvatures, but nevertheless accommodate the larger portion of exposed bars. No relation was found between the land cover adjacent to the river and the occurrence of sharp bends. Soil processes may play a crucial role in the formation of sharp bends, which is inferred from iron and manganese concretions observed in the riverbanks, indicating ferric horizons and early stages of the formation of plinthic horizons. Historical topographic maps show the planform activity of the river is low, which may relate to the scour holes slowing down planimetric development.

3.1 Introduction

Most natural river bends are mildly curved and deposit sediment at point bars at the inner bank, and excavate pools at the outer bank. River bends, however, can also develop a completely different morphology. In small streams, with erosion resistant banks and mild channel slopes, bends can become remarkably sharp, with an increased depth and width resulting in an exceptionally high cross-sectional area (Alford et al., 1982; Andrle, 1994; Hodkinson & Ferguson, 1998; Nanson, 2010). The water flowing through this large cross-section, often recirculates horizontally (Andrle, 1994; Hodkinson & Ferguson, 1998; Nanson, 2010) near one or both banks. These recirculations help maintaining high velocities through the large cross-section, while the average velocity decreases.

Several laboratory studies have investigated the flow through sharp bends in detail. Bend sharpening increases the depth of outer bank scours, that can reach up to three times the average depth (Blanckaert, 2010). This strong scouring in sharp bends is often associated with down-welling near the outer bank caused by the impinging flow on the outer bank and the development of horizontal recirculation (Hodkinson & Ferguson, 1998; Ferguson et al., 2003; Blanckaert, 2010; Blanckaert et al., 2013). Vertical cross-stream secondary

circulation gradually increases with sharpening of a bend, until it saturates due to interactions between primary and secondary flows (Blanckaert, 2009; Ottevanger et al., 2012). Next to this secondary circulation, a secondary counter-rotating cell can develop, which slows down the main flow near the outer bank. Although these results are valuable to the understanding of the flow through sharp bends, it remains difficult to generalize them to natural streams, and especially to large rivers.

In large rivers sharp bends have only been observed occasionally (Gharabaghi et al., 2007; Beltaos et al., 2012). Flow in sharp bends of the Mackenzie delta also features two horizontal recirculation zones in a cross-section which is remarkably large (Beltaos et al., 2012). The scarcity of field based evidence of deeply scoured sharp bends in large rivers suggests that these features are rare and only occur in an arctic region. The conditions and processes leading to the formation of such large cross-sections with the corresponding flow patterns remain largely unexplored. In this study we show that deep scours in sharp bends are ubiquitous in an alluvial reach in the Mahakam River, a large tropical river located in East Kalimantan, Indonesia. In this reach several very sharp bends are found, which are unaffected by consolidated outcrops, offering the opportunity to study self-formed high-curvature meanders. We analyse the river planform in relation to the channel bathymetry, width of the river corridor and the presence of eroding, stable or advancing banks.

Section 3.2 introduces the central Mahakam area and offers background on the geological setting. In Section 3.3 the methods for analysis of topographic maps and remotely sensed images, bathymetry and stream reconnaissance data are presented. The results are described in Section 3.4 for the planimetry and slope of the river, the delineation of the alluvial corridor, and the river bank characteristics. The results are discussed in Section 3.5. Section 3.6 summarizes the main findings of this study.

3.2 Study Area

The Mahakam River is a large tropical river with an average discharge of $3000 \text{ m}^3 \text{ s}^{-1}$, a catchment area of 77150 km^2 and a mild longitudinal slope. In-channel sediments range between fine to medium

sands (Sassi et al., 2013). Annual rainfall is bimodal as is the discharge. The Mahakam flows from its source in the mountainous inland of Kalimantan to the Kutei basin, an intermontane depression separated from the Barito basin by a hilly area in the south (van Bemmelen, 1949). The Kutei basin was formed by rifting during the middle-Eocene. Folding of the Kutei basin until the early Miocene caused fluvio-deltaic sediments to be deposited in the basin. The long term subsidence of the basin is estimated to be around 0.2-0.5 m/ky (Storms et al., 2005). The Mahakam cuts through the Samarinda anticlinorium and eventually debouches into the Makassar Strait where it forms the Mahakam Delta (Sassi et al., 2012).

The reach considered in this study is characterized by a very mild channel slope of about 10^{-5} (Sassi et al., 2011a), which allows the tides to sometimes reach the upstream end of the Kutei basin (Hidayat et al., 2011). With an average width of 300 m the river has a unit stream power of about 1 W/m^2 . The average depth of the river is about 15 m.

The present work focuses on the lakes area within the Kutei basin (Figure 1.2). Most analyses are performed on the reach between the upstream boundary of the Kutei basin ($s = 0 \text{ km}$), with s being the along channel coordinate) and the delta apex ($s = 311 \text{ km}$) (Figure 1.2). Considering the geomorphology of the area, we can distinguish two main reaches: an upstream reach between $s = 0$ and 150 km, and a downstream reach between $s = 150$ and $s = 311 \text{ km}$. The upstream reach flows through alluvial, unconsolidated sediments in the sedimentary basin, and the downstream reach through alluvial material and consolidated outcrops from the Samarinda anticlinorium.

In the upstream reach several lakes and peat domes have formed. The lakes play an important role in regulating water and sediment discharge eventually issued to the delta (Storms et al., 2005; Sassi et al., 2011a, 2012; Hidayat et al., 2012). Small channels connecting the lakes to the river (termed tie-channels by Rowland et al. (2009)), regulate the exchange and, depending on the hydrograph of the river, carry water from the lakes into the river or vice-versa, functioning as a discharge buffer (Hidayat et al., 2011). There are two main lakes north of the river: Lake Semayang and Lake Melintang. Lake Semayang, the easternmost lake, is connected to the river through a tie-channel. Lake Melintang, the westernmost lake is connected on

the east side to Lake Semayang while in the south it connects to the river through a small, 10-15 meters wide channel. A third lake, called Lake Jempang, connects to the river through a large tie-channel on the east side, and a small 2-3 meters wide tie-channel on the northern side. The lakes are surrounded by several peat domes with a diameter of around 35 km. These domes are considered to contribute to the buffering effect on discharge (Hidayat et al., 2012; Sassi et al., 2013), as they can store large amounts of water.

In the lakes area the river is mainly single threaded and meandering. At one location, near the large southern lake, a reach of the river shows signs of anastomosis, having two long channels. This, however, is the result of a meander cutoff. The northern of these two channels is now slowly silting up. Four main tributaries are found in the area. The River Pahu connects to the Mahakam upstream of the lakes at the southern side of the river. The rivers Belayan, Kepala and Rantau are found downstream of the lakes and connect to the river at the northern side.

3.3 Methods

Topographic maps and satellite remote sensing

Planimetric information was obtained from analysis of Landsat ETM+ satellite imagery using the pan-sharpened RGB bands (15 m resolution). We extracted the color values best resembling water and manually brushed away clouds and cloud shadow. Bank lines were obtained by delineating the parts marked as water in the images. No bars were visible in the images, making the vegetation line coincide with the boundary of flooded areas. The centerlines were obtained by determining the midpoints between the banks through a digitization toolbox called ArcSCAN. The along-channel coordinate s is directed seaward and has its origin just upstream of the lakes (Figure 1.2). Most parameters were determined for a stretch reaching until the city of Samarinda ($s = 311$ km), just upstream of the delta apex.

The river centerline was re-sampled to an interval of 50 m. Given the Cartesian coordinates of the centerline x and y as a parametric function of s , the curvature C normalized by the width W is com-

puted as (Legleiter & Kyriakidis, 2006):

$$C = W \frac{x'y'' - y'x''}{(x'^2 + y'^2)^{\frac{3}{2}}}, \quad (3.1)$$

in which the prime (') denotes a derivative with respect to s . Following the definition of Hickin & Nanson (1984), bends are considered sharply curved when C exceeds a value of 0.5. Before computing the curvature, the centerline was smoothed using a cubic spline with tension (De Boor, 1978). Inflection points were detected at the zero-crossing locations of the curvature. Each portion of the river between two consecutive inflection points is called a half-meander. Two consecutive half-meanders form a meander, the length of which can be computed along the Cartesian (x, y) or the intrinsic (s, n) coordinates, where n is the cross-channel coordinate. The ratio of the intrinsic meander length L_i and Cartesian meander length L_c defines the sinuosity σ .

A continuous wavelet analysis was performed on the normalized curvature series. The continuous wavelet analysis was performed with a second order differential of Gaussian function wavelet, also known as a “Mexican hat” wavelet. This is a real valued wavelet which therefore is mostly suitable to detect peaks and discontinuities (Torrence & Compo, 1998). Subsequent meanders with opposite curvature will display in the power spectrum as two different peaks, which would not be the case when using a complex wavelet, where such subsequent and opposed meanders would appear as a single peak (Torrence & Compo, 1998). This wavelet is also known to result in a high spatial resolution, while the frequency resolution will be low (Torrence & Compo, 1998). In the present case the high spatial resolution is preferable to a high frequency resolution since we expect only a limited number of scales in the frequency domain.

Topographic maps based on aerial images from 1981 were compared with Landsat ETM+ images from the year 2000. This comparison was performed to estimate the migration rates of the river-banks during a period of 19 years. The lateral deposition rates were determined as the Euclidean distance between the river polygon from the topographic maps and the nearest banklines from the Landsat images. Similarly, the erosion rates were determined as the Euclidean distance between the banklines from the Landsat images and the

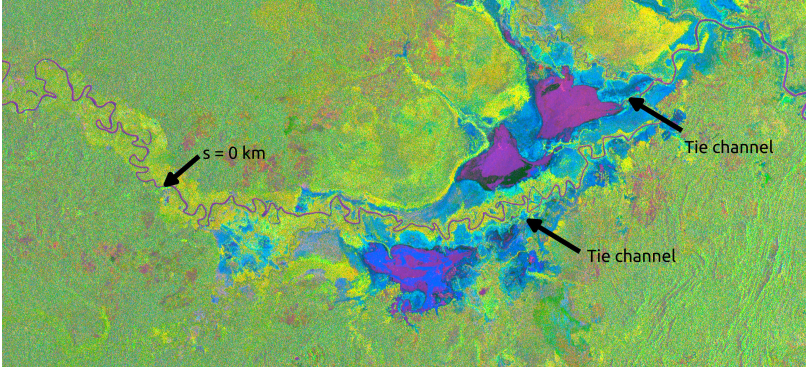


FIGURE 3.1. Principal component analysis of 12 PALSAR images (Red: Third component, Green: First component, Blue: Second component). Pronounced levees can be distinguished as yellow areas among the blue floodplains. The lakes and the river have a pink to black color. In the upstream area, the meandering belt is highlighted. The tie channels are indicated by the arrows.

nearest banklines from the topographic maps. This resulted in a map with the total erosion and aggradation rates. A basic assumption in this method is that total erosion and deposition do not exceed the width of the river during the period under consideration. There is no doubt this condition is satisfied. Bank change can only be detected when it exceeds a detection threshold which corresponds to the resolution (30 m) used in the analysis.

A series of 12 Phased Array L-band Synthetic Aperture Radar (PALSAR) images, collected during the years 2007 and 2008 and covering a wide range of hydraulic conditions (Hidayat et al., 2012), were included in a principal component analysis (PCA). This allows to convert the images in a set of independent images, such that the three images representing the three principal components capture the largest variance of the original set. PCA maximizes the amount of information than can be contained in a color composite image. The first three components were used to create a color composite of the lakes area (Figure 3.1). The results of the PCA can be interpreted as different flooding conditions and allow to distinguish features such as levees and floodplains, revealing the alluvial corridor of the river.

Bathymetry mapping

The bathymetry of the river was determined with a single beam, dual frequency echo-sounder, which in the area under consideration mostly operated at a frequency of 200 MHz. The depth soundings were collected along cross-river transects, with a spacing of, on average, one river width in the longitudinal direction. The sounding data were corrected for the depth of the transducer, and for the fluctuations in water level, measured with nearby pressure sensors. The obtained corrected depth is therefore the depth of the river relative to the seasonally averaged water level.

To interpolate cross-section profiles of depth onto a regular grid, the Cartesian coordinates were first transformed to a channel fitted coordinate system. The centerline was re-sampled to a resolution small enough to ensure minimal curvature changes over each segment on the centerline. Each vertex of the centerline can be described by a vector $\vec{r}(s)$, with s being the length along the centerline. The tangential (\vec{T}) and normal unit vectors (\vec{N}) are defined as (Legleiter & Kyriakidis, 2006):

$$\vec{T}(s) = \frac{\vec{r}(s)'}{|\vec{r}(s)|} \quad (3.2)$$

$$\vec{N}(s) = \frac{\vec{T}(s)'}{|\vec{T}(s)|} \quad (3.3)$$

A nearest neighbor search was performed to determine which points are closest to a certain centerline point. Considering a point \vec{P} nearest to the centerline point \vec{r} , the channel fitted coordinates s and n of that point are defined as:

$$\vec{P}_{(s,n)} = \begin{pmatrix} r_s \\ 0 \end{pmatrix} + \begin{pmatrix} (\vec{P} - \vec{r}) \cdot \vec{T} \\ (\vec{P} - \vec{r}) \cdot \vec{N} \end{pmatrix} \quad (3.4)$$

where r_s is the s component of vector \vec{r} . Since we expect anisotropy in the depth, with a greater variance in the n -direction, we multiply the n coordinates with an anisotropy factor which was attributed a value of five. Eventually, the collected depths were interpolated to a channel fitted anisotropic regular grid with natural neighbor

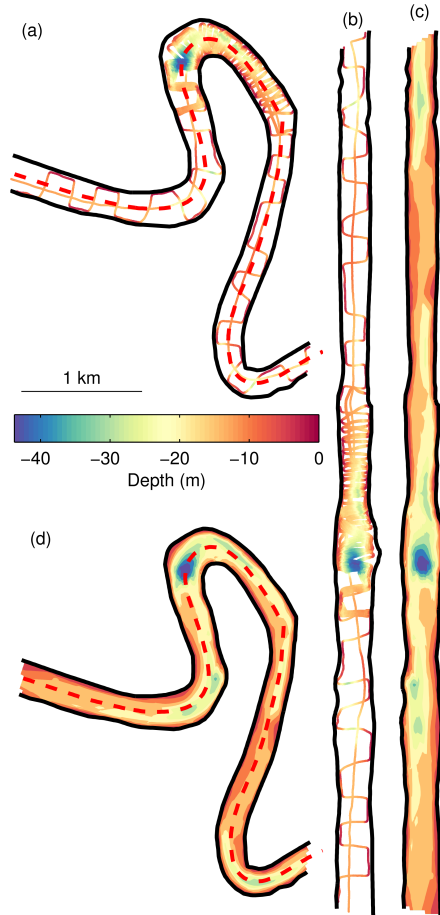


FIGURE 3.2. Example of the bathymetric interpolation procedure. The bathymetric cross-sections (a) were transformed to a channel-fitted coordinate system (b), the data were interpolated to a regularly spaced grid (c) and transformed back to cartesian coordinates (d).

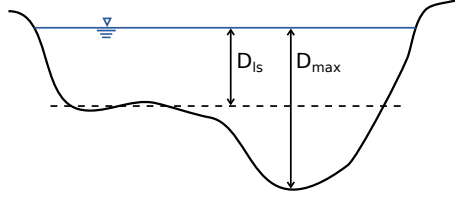


FIGURE 3.3. Metrics used for the calculation of the depth excess, to quantify the magnitude of a scour in relation to the mean depth over the cross-section. D_{ls} is the regional mean depth, i.e. the mean depth low-pass filtered to retain the regional mean-depth fluctuations and D_{max} is defined as the local maximum depth.

interpolation (Figure 3.2). To characterize scouring in the bathymetry a “depth-excess” parameter D_e was defined as:

$$D_e = \text{sign}(C) \left(\frac{D_{max}}{D_{ls}} - 1 \right) \quad (3.5)$$

where D_{ls} is the regional mean depth, i.e. the mean depth low-pass filtered to retain the regional mean-depth fluctuations and D_{max} is defined as the local maximum depth. For example, this means that when this parameter is equal to one, the maximum depth is double the mean depth (Figure 3.3).

In several previous studies the bed slope has been related to the radius of curvature through a parameter referred to as the scour factor (Odgaard, 1981; Ikeda et al., 1981; Blanckaert et al., 2013):

$$\frac{\partial z_b}{\partial n} = -A \frac{D_{ls}}{R} \quad (3.6)$$

where z_b is the bed elevation, A is the scour factor and R the planimetric radius of curvature. To obtain a proxy of A from the bathymetry data of the Mahakam, we first determined the apices of the bends as the locations of maximum curvature between two inflection points. Subsequently, the bend scour depth was determined as the deepest point in the surrounding of the bend apex (i.e. the streamwise domain reaching one river width upstream and downstream from the apex). At the scour location the transverse bed slope was determined by fitting a line to the central 10% of the bathymetry.

Stream reconnaissance

A stream reconnaissance has been performed following the procedure outlined by [Thorne \(1998\)](#). The reconnaissance was performed along the upstream reach characterized by the presence of natural levees and lower floodplains located behind those. The data-collection consisted of a systematic inventory of bank characteristics, soil types, and bankface vegetation, and taking a set of photographs. The spacing between the surveyed banks was dependent on visible changes in bank type. At several banks, samples were collected to determine the grain size distribution taking into account possible vertical stratification. For some of the samples the total iron and manganese contents were determined through digestion with perchloric and nitric acid followed by atomic adsorption spectrometry. The total amount of iron and manganese was used to establish the possible presence of plinthite in the soil ([IUSS Working Group WRB, 2007](#)). Soil profiles were sampled with a hand auger and qualitatively described in terms of texture, redoximorphic properties, presence of iron and manganese concretions and the portion of the profile containing organic material.

Recorded bank characteristics included a bank profile, containing the height of the bank, distinguishable layers, the slope of the layers and bed material in these layers. Other important features such as bank failures and toe sediment accumulation were all described. The data collection was performed for the visible part of the banks above the water level. By performing the reconnaissance survey during the dry season the visible part of the bank was maximized. The disadvantage of sampling in the dry season is that the river is dormant in terms of morphology, allowing for new vegetation to grow on the banks. The resulting data were digitized in a GIS.

3.4 Results

Geometric analysis

The width of the river remains relatively uniform (about 250 m) in the lakes area. A slightly decreasing trend can be observed, which may be related to the presence of the lakes. Downstream of the lakes, the river width increases reaching a width of about 500 m near the delta

apex (Figure 3.4). The sinuosity has the highest peaks in the lakes area. Downstream of the lakes the sinuosity decreases and features smaller peaks, which may be associated to the orographic controls on the channel. The normalized curvature C has the highest peaks in the lakes area, with several peaks exceeding a curvature value of 2.

Based on the depth excess parameter, 35 scours were identified that exceed three times the river depth. Four scours exceed four times the average depth, with the deepest scour reaching a depth of 60.2 m. Deep scours are often located in the middle of the channel forming nearly symmetric cross-sections. Shallower scours are more asymmetric (Figure 3.5). At the scours the river is usually much wider compared with straight or mildly curved bends. Sharp bends with deep scours usually lack a point bar. To test the relation between curvature and the presence of scours, the depth excess was compared with the normalized curvature (Figure 3.6). These two series show a striking similarity, which is quantified based on cross-correlation. The normalized cross-correlation peaks ($\rho = 0.7$) at a lag of about half a river width (150 m), indicating that scours systematically occur upstream of the point of highest curvature.

Previous findings suggest that values of A decrease with increasing curvature. Typical values range between 2 and 5 for natural rivers (Odgaard, 1981; Ikeda et al., 1981), but laboratory experiments in sharp bends resulted in smaller values (Blanckaert et al., 2010, 2013). Our results confirm the existing hypothesis of lower scour factors for higher curvature, but this result is statistically insignificant. Scour factors for mild bends in the Mahakam range between 1 and 10, while for bends with higher curvature A remains below 2 (Figure 3.7). The large scour holes found in sharp bends in the Mahakam often feature a symmetric shape, with the deepest point near the centerline. The transverse slope near the centerline will therefore be small, decreasing the value of the scour factor. Considering this, it can be considered inappropriate to parameterize scours of the Mahakam with a single scour factor based on the transverse bed slope at the centerline. The mid-channel scours are inherently different from pools in outer bends.

In the lakes area, typical meander lengths are in the order of 8 km (Figure 3.8). Hardly any downstream skewed meanders are found, while most mild meanders are upstream skewed. Several sharply curved meanders are found, often surrounded by low curva-

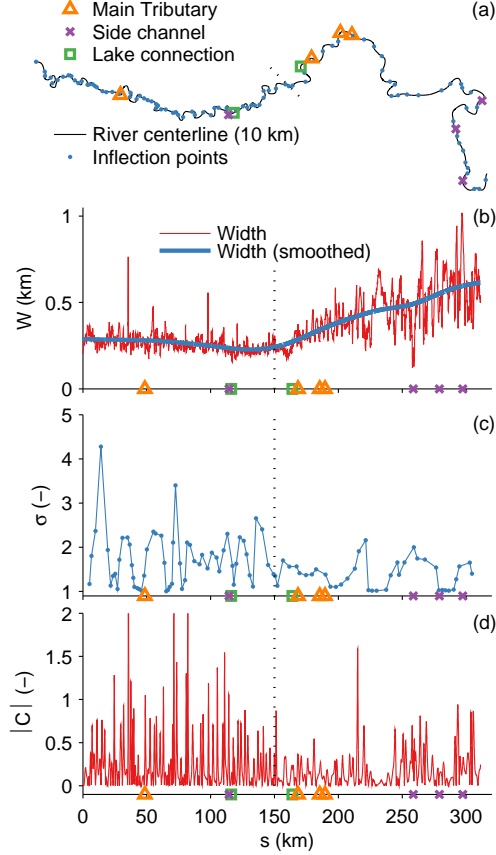


FIGURE 3.4. (a) Centerline with inflection points used to determine half-meanders. (b) The raw river width (red) and the smoothed river width (blue) showing a slightly decreasing trend in the lakes area followed by an increase in width in the downstream part. (c) Every two consecutive half-meanders were used to determine the sinuosity (σ) that decreases downstream. (d) The centerline curvature was normalized with the channel width ($C = W/R$). The dotted lines indicate the transition from the upstream reach, in the sedimentary basin, to the downstream reach, in the uplifted hilly area.

3. SHARP BENDS ASSOCIATED WITH DEEP SCOURS

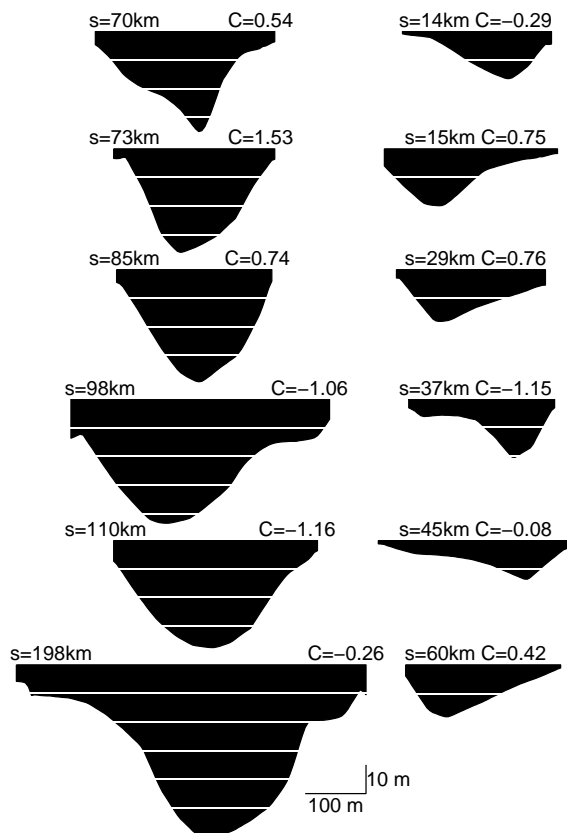


FIGURE 3.5. Impression of cross-sections at a number of deep (left) and shallow (right) scour holes. The white lines are spaced 10 m. At each cross-section the normalized curvature and the location is indicated. Several deep scours are found at low curvature sections (such as the scour in the bottom left), which are mainly located in the hilly area.

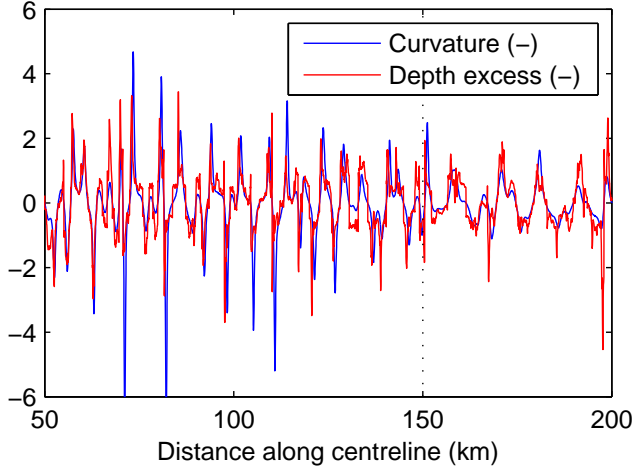


FIGURE 3.6. Series of normalized curvature and normalized depth excess. These two parameters are highly correlated (normalized cross correlation $\rho = 0.70$) at a lag of 150 m, indicating scouring generally occurs at a length that corresponds to half a river width upstream of the point of highest curvature). The dotted line indicates the transition from the upstream reach to the downstream reach.

ture stretches, giving these stretches a characteristic zigzag shape. A few double looped meanders are observed. Larger scale curving of the river, often referred to as multiple looping, is ubiquitous in the area and increases in strength from upstream to downstream (Figure 3.8), featuring a strong large-scale turn in the Samarinda anticlinorium. Such complex meander structure can be related to the floodplain erosional heterogeneity (Güneralp & Rhoads, 2011; Limaye & Lamb, 2014), to complex non-linear interactions between the flow and morphology (Zolezzi & Seminara, 2001; Güneralp & Rhoads, 2009) and to vegetation density and topography induced flow resistance (Lazarus & Constantine, 2013). In this area, the meander behavior differs significantly from meandering in the lakes area (Figure 3.8). Here, the typical meander length increases, and meandering zones alternate with relatively straight, low curvature sections (Figure 3.8). Although difficult to determine exactly, the transition in meander behavior occurs somewhere around $s = 130$ km, which is

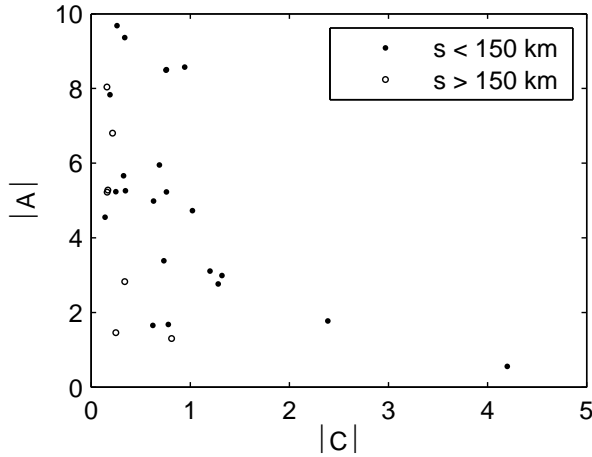


FIGURE 3.7. Scour factor based on the local transverse slope at the centerline, as a function of normalized curvature. Full dots are located in the upstream reach, and empty dots are located in the downstream reach

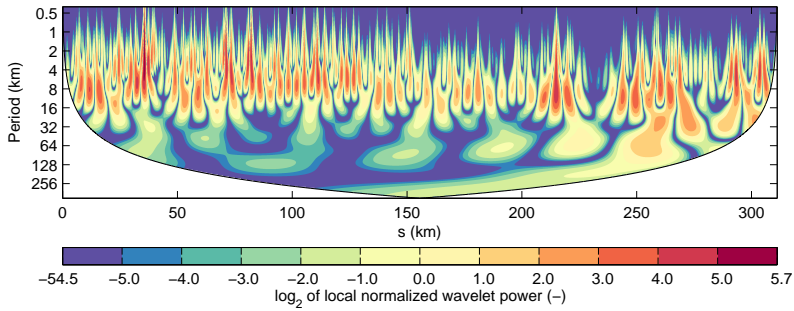


FIGURE 3.8. Local wavelet power spectrum of the normalized centerline curvature. The highest peaks in the spectrum, with a period of about 4-8 km, correspond to half meanders. The somewhat smaller peaks at larger periods (16-256 km) resemble multiple loops, which contain several half-meanders.

located near the first tie-channel junction.

The comparison of old topographic maps and recent Landsat images revealed limited planimetric development in the area. Erosion and deposition rates established from the images hardly ever exceed the detection threshold for erosion and deposition in the available imagery, apart from a few exceptions at the apex of river bends. The expected erosion and deposition rates are therefore low in the area (below 30 m over a period of 20 years). These results indicate the Mahakam river planform is virtually fixed in the lakes region, although some bend extension may occur.

Delineation of the alluvial corridor

Pronounced levees are present in the lakes area (Figure 3.1), especially in the stretch of the river north of the tie channel between the southern lake and the river, and the tie channel connecting the river to the northern lakes. In the area surrounded by the lakes, the levees closely follow the river planimetry and hardly any abandoned channel or old meanders can be found, apart from those at a few locations where bends were artificially cutoff. This confirms that this stretch of the river is morphologically dormant. Also upstream of the lakes region, floodplains can sharply be distinguished where inundation under vegetation occurs. This area corresponds to the meander belt of the river. In most of the upstream reach, the floodplains are very wide (40-50 km).

Given the complex nature of the land cover and vegetation types occurring in the Mahakam lakes area (Figure 3.9), there is no apparent relation between the morphology and the surrounding land cover. The proximity of large peat domes may influence the river morphology, but nowhere in the Mahakam lakes area does the river cut through the peat. It is therefore unlikely that the presence of peat is directly influencing the morphology of the river.

Characterization of river banks and bars

From the information gathered during the stream reconnaissance, eight different bank types were determined in the reach under consideration (Table 3.1). We will briefly give an overview of the charac-

3. SHARP BENDS ASSOCIATED WITH DEEP SCOURS

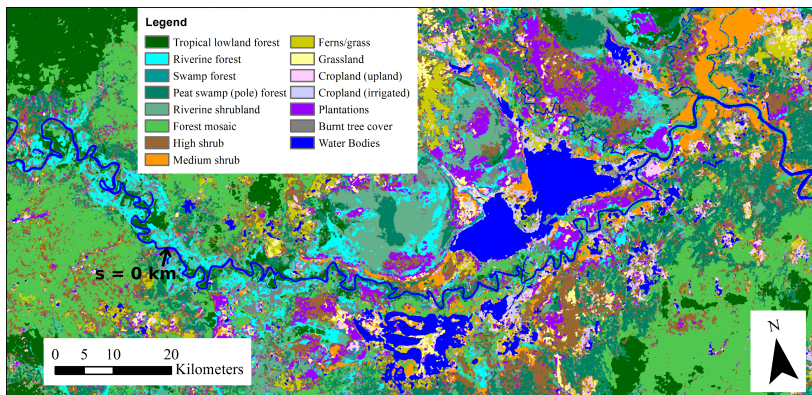


FIGURE 3.9. Land cover map based on an unsupervised mixture modelling, followed by a Markov Random Field classification of Fine Beam Single and Fine Beam Dual polarization path PALSAR image pairs (Hoekman et al., 2010).

TABLE 3.1. Bank types used for classification.

Bank type	Bank description
Canal	Location with/near junctions
Bank Protection	River training structures present
Erosive	Unstable bank with erosion
Erosive stable	Both stable and erosive features
Stable	Bank which is neither advancing nor eroding
Advancing stable	Both stable and advancing features
Advancing	Actively advancing banks
Bar	Sandy deposits on the banks

teristics of the main bank types, before presenting some quantitative results on the occurrence of the different bank types.

Erosive banks

Most erosive banks consist of silty clay. The texture of the sediment is usually coarsening upward. Gley spots are found in the entire soil column up to a depth of four meters with the strongest gley formation at a depth of about two to three meters, which is about one meter above the mean water level during the dry season.

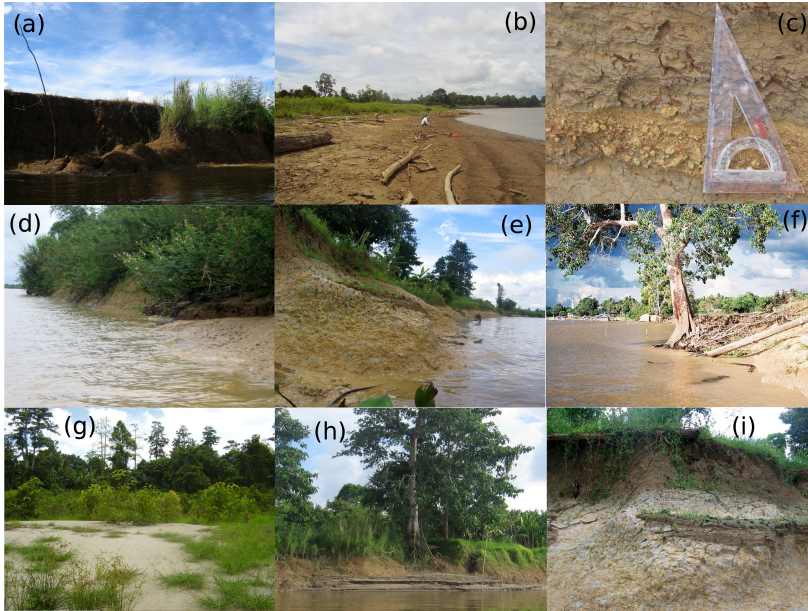


FIGURE 3.10. Typical bank types and features found in the Mahakam lakes area: (a) eroding bank with a bank failure; (b) advancing bank; (c) iron and manganese concretions (d) stable bank; (e) embayments with iron and manganese concretions; (f) eroding bank; (g) point bar; (h) reattachment bar; (i) Gley formation at the lower bank.

Erosive banks feature a fallow bank-face. On top of the bank a mixture of forest and agricultural fields is found. The forest vegetation is dense and mature. Trees near the bank-face feature exposed roots and lean over on the bank as a result of undercutting (Figure 3.10f). Exposed roots growing back into the banks indicate inactive erosion. Exposed roots sometimes reach such a high density that they protect the upper bank from erosion. Total iron amounts in combination with the physical properties of the concretions and nodules found in the banks, indicate the presence of plinthite (Division of Soil Survey, 1993; IUSS Working Group WRB, 2007). These nodules and concretions give additional strength to the soil matrix.

Erosive banks along the Mahakam are generally taller than stable or advancing banks with angles reaching 100 degrees in the upper

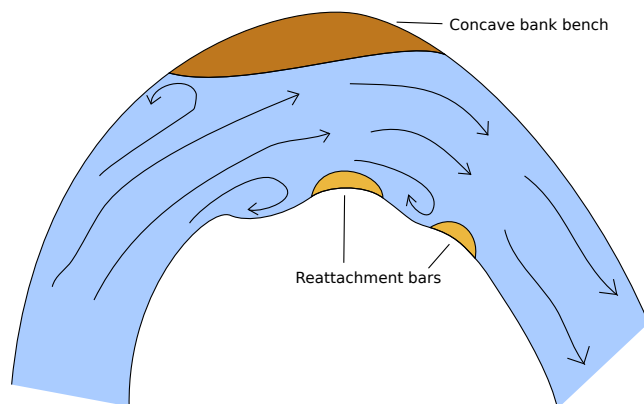


FIGURE 3.11. Sketch of reattachment bars and outer bank benches as commonly found along the Mahakam river.

part of undercut banks. The middle and lower part of the banks feature an angle of approximately 35 to 50 degrees. The bank toe usually has an angle of 30 degrees or is nearly horizontal. Banks on which agriculture takes place often feature a steeper and more distinct upward concave profile, while banks covered with forest have a slight concave upper part and a convex toe. This may be caused by a stabilizing effect of the forest vegetation on the upper part of the bank, which is absent in the case of agriculture because of shallower root depths.

In erosive sections of the river Mahakam, half-moon shaped embayments are often found (Figure 3.10e). These embayments occur most frequently at the inner bank of usually quite sharply curved banks. They mostly occur at the upstream end of the concave bank. At these embayment locations, flow recirculation is often observed and at the downstream end of the embayments small reattachment bars (Rubin et al., 1990) develop (Figure 3.11). Further away from the bend, embayments are also observed, but these are usually smaller in size with shallower incisions into the bank. Similar features have been previously observed in tropical systems (Coleman, 1969; Darby et al., 2010). The embayments are known to increase form roughness of the banks, thereby decreasing lateral erosion (Darby et al., 2010).

Bank failures were observed, constituting the main process gov-

erning erosion. They were present on most banks, and did not seem to be related to any specific condition in the surroundings. This suggests that the failures observed are mainly caused by fluvial action. Cantilever failures were frequently encountered, mostly in association with non-agricultural vegetation. This suggests that the roots stabilize the top of the banks, while below the layers are eroded, causing undercutting and eventually bank failure. At locations covered with agricultural vegetation, the main process of erosion is bank failure and shear failure visible in pop-out and slab failures. Another main type of bank erosion occurs as a result of rotational slip failure, which is commonly found in highly cohesive sediment (Thorne, 1998).

Stable banks

The observed soils on stable banks are generally composed of clayey silt or silty clay, and are usually coarser than sediments in eroding banks. Vegetation is often dominated by a dense mix of shrubs and reed. Bamboo was often found near agricultural fields. Trees are sparse and the toe of the bank is often fallow or sparsely covered by vegetation. The shape of stable banks is quite consistent along the river, with a general slope of about 20 degrees. Although these banks are classified as stable, they are often found with subtle signs of erosion or sedimentation.

Advancing banks

Advancing banks are generally found to be composed of alternating layers of silt and sand, with a coarsening upward trend in the middle of the bank, and a fining upward trend on top of the bank. The material on the banks is unconsolidated, indicating freshly deposited sediments. Pioneer vegetation is found near the toe of the bank, while the middle and upper bank are densely covered with grasses, saplings, shrubs and bushes, fringed by mature vegetation further from the river. Woody debris is largely deposited on parts of the banks that were exposed during low flow conditions.

Slopes on advancing banks are mild, with angles up to 15 degrees. Heights are generally lower than two meter. Profiles can sometimes be stepwise, which is attributed to ship induced wave erosion. Typ-

ical for these banks is a strongly cracked, blocky layer composed of silty material.

Bars

In the section of the Mahakam we considered, three types of bars can be distinguished: point bars, found at convex inner banks, reattachment bars (Figure 3.11), found at locations where small regions of flow separation occur, and concave bank benches found at the outer, concave side of a bank (Figure 3.11). Bars are characterized by a sandy composition, with very low vegetation cover, which usually consists of grasses. Reattachment bars were usually much smaller than point bars, with a stepwise profile on the upstream side featuring a slowly transition to a mild slope on the downstream side. Point bars were only observed in two bends in the entire reach under consideration. The apparent absence of point bars is attributed to the impossibility to observe these features due to high water levels (Figure 3.5). Ship induced wave action erodes the bars during the dry seasons, but to a very limited extent. Also, piping and sapping (Thorne, 1998) occurs in the bars, when they are not submerged causing some additional erosion.

Occurrence of bank types and bars

After classifying the banks according to Table 3.1, we performed an analysis of the occurrence of the banks in relation to the centerline curvature. To this end, the banks were subdivided in inner or convex banks, and outer or concave banks. Based on the centerline curvature the banks were subdivided in 20 inter-percentile range classes, spanning 5% of the banks each. Although high curvature classes span a higher range of curvature (see Figure 3.12), the classes based on percentiles ensure a comparable statistical significance of the results, for each of the classes. For each class, the relative occurrence of each bank type was determined. Eroding and eroding/stable banks were considered as one class in this analysis, and so were advancing and advancing/stable banks.

Eroding banks occur most commonly on the outer bends, but for high curvature classes, the occurrence of eroding banks at the inner bends increases significantly (Figure 3.13a). An opposite trend is ob-

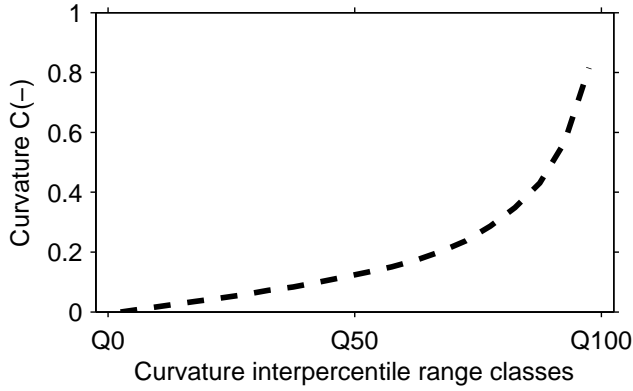


FIGURE 3.12. Curvature for each of the curvature interpercentile range classes. Low curvature classes span a smaller range of curvature, since low curvature reaches are more common than high curvature reaches.

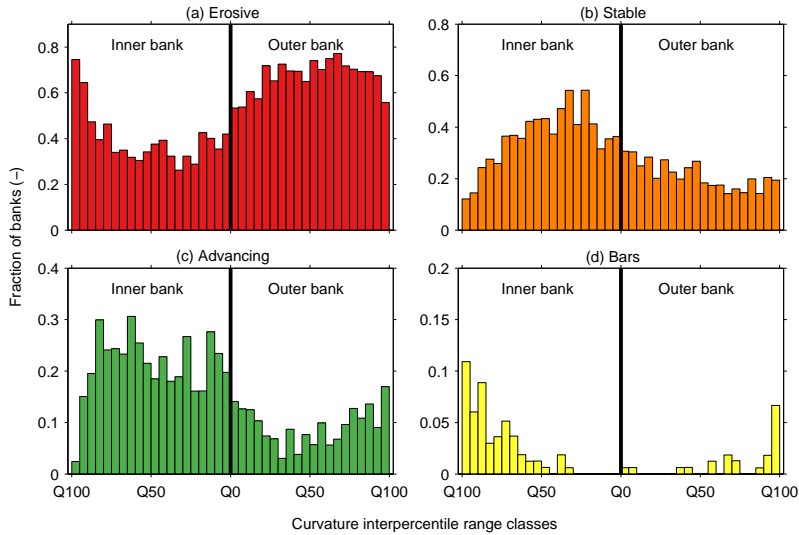


FIGURE 3.13. Histograms of the relative occurrence of a certain bank type within a curvature interpercentile range class. The left side of each panel shows the distribution of bank types for the inner banks or convex banks and the right side corresponds to the outer or concave bank.

served for advancing banks that are most common at inner bends, except for high curvature classes, where most advancing banks are observed at the outer bends. While advancing banks at sharply curved inner bends are hardly found, bars are still present. An explanation for their occurrence could be the replacement of point bars by reattachment bars (Figure 3.11), mostly on eroding banks. In the highest curvature class several bars are observed in the outer banks. These bars are also referred to as concave or outer bank benches (Figure 3.11). Stable banks occur mostly at low curvature banks and mostly on the inner banks.

3.5 Discussion

Scours in sharp bends of the Mahakam river exceed three to four times the average river depth. This result is surprising when considering earlier laboratory studies that found scour depths reaching two times the average depth (Blanckaert, 2010; Blanckaert et al., 2013). The shape of the scours, being deep and wide and lacking a point bar, resemble the shape of circular meander pools (Andrle, 1994; Alford et al., 1982) or bends in peat areas (Nanson, 2010; Nanson et al., 2010). A common characteristic shared by the Mahakam and the rivers described in the studies of Andrle (1994); Alford et al. (1982); Nanson (2010); Nanson et al. (2010) is a low channel gradient and cohesive floodplain material. All of these bends are also associated with horizontal flow recirculation in the inner bank and sometimes also in the outer banks.

An inversion of the erosional and depositional processes was observed in the Mahakam lakes area, which is related to high channel curvature. The river alternates between two distinct bend regimes. In mild bends, outer banks erode and inner banks advance. In sharp bends, the inverted processes feature stable or advancing outer banks and eroding inner banks. Since high curvature stretches are related to the presence of deep scours, there might be a relation between the deep scours and the change in erosional and depositional patterns. Previous studies also found a changing morphological behavior for increasing curvature and very sharp bends (or hairpin bends (Woodyer, 1975)). Lateral migration is in fact known, for some rivers, to increase for increasing values of C , until a certain threshold

is reached, after which migration rates decrease (Hickin & Nanson, 1984; Page & Nanson, 1982; Güneralp & Rhoads, 2009). The systematic analysis of the Mahakam River seems to confirm these previous findings, as high values of curvature are found in areas with limited lateral erosion..

Morphological features found in the Mahakam lakes area are in some respect similar to what was found in Mekong River, especially regarding the embayments (Darby et al., 2010). The Mekong River also features deep pools and limited lateral migration, but these processes can be the consequence of structural constraints (Meshkova & Carling, 2012). Similar to the Strickland River, lateral migration may be limited to the apices of bends, while the largest part of the river is relatively fixed (Aalto et al., 2008). Similar low lateral erosion rates were also observed along the Fly River which did not migrate over a period of investigation of 50 years (Dietrich et al., 1999). Bends in the Mahakam are found to show common features with many highly curved bends found in usually small streams with a small stream power in temperate regions (Andrle, 1994; Nanson, 2010).

Cohesiveness of the banks, low longitudinal slopes, wide floodplains and dense vegetation are hypothesized to be the main ingredients leading to the anomalous morphology found in the Mahakam lakes area. The pronounced differences in morphology suggest the occurrence of anomalous flow patterns creating the scours. The large depth variations associated to the scours present challenges for monitoring and modeling of rivers such as the Mahakam. The excessive depths have motivated the development of a new technique to process repeat-transect acoustic Doppler current profilers (ADCPS) data (Chapter 4), which allows monitoring of flow in the scours. The abrupt bed level changes may cause a strong vertical flow component, invalidating the assumption of a hydrostatic pressure distribution in common Reynolds-averaged Navier Stokes (RANS) models.

3.6 Conclusions

In the Mahakam river, sharp bends are systematically related to deep scours located upstream of the point of highest curvature. The scours occur at a distance upstream of the bend apex which corresponds to half the local river width. At high-curvature sections, patterns of ero-

3. SHARP BENDS ASSOCIATED WITH DEEP SCOURS

sion and deposition invert, and new features develop such as embayments in the inner banks and cohesive bars at the outer banks. The lack of old channels in the floodplains, suggests that the planimetric development is limited. This can be caused by the presence of the embayments or by the non-harmonic type of meandering behavior the system develops, creating scours that counteract meander migration, or by a combination of both. Contrary to expectations, the scour holes did not coincide with local bank characteristics, such as highly resistant bluffs. The scours can be considered a product of autogenic processes, which may be typical for tropical lowland areas. Low stream power and wide floodplains, combined with erosion resistant material and vegetation in the area, may cause the river planform to freeze, and a zig-zagged meander pattern to develop with very deep scours.

CHAPTER 4

Improved flow velocity estimates from moving-boat ADCP measurements

Abstract

Acoustic Doppler current profilers (ADCPs) are the current standard for flow measurements in large scale open water systems. Existing techniques to process vessel mounted ADCP data assume homogeneous or linearly changing flow between the acoustic beams. This assumption is likely to fail, but is nevertheless widely applied. We introduce a new methodology that abandons the standard assumption of uniform flow in the area between the beams and evaluate the drawbacks of the standard approach. The proposed method strongly reduces the extent

This chapter is based on: VERMEULEN, B., M. G. SASSI, AND A. J. F. HOITINK, 2014, Improved flow velocity estimates from moving-boat ADCP measurements, *Water Resour. Res.*, doi:10.1002/2013WR015152

over which homogeneity is assumed. The method is applied to two field sites: a mildly curved bend near a junction featuring a typical bend flow and a sharply curved bend that features a more complex sheared flow. In both cases, differences are found between the proposed method and the conventional method. The proposed technique yields different results for secondary flow patterns compared with the conventional method. The velocity components estimated with the conventional method can differ over 0.2 m/s in regions of strong shear. We investigate the number of repeat transects necessary to isolate the mean flow velocity vector from the raw ADCP signal, discarding the influences of noise, positioning and projection errors, and turbulence. Results show that several repeat transects are necessary. The minimum number of repeat measurements needed for robust mean velocity estimates is reduced when applying the proposed method.

4.1 Introduction

Acoustic Doppler current profilers (ADCPs) are the current standard for flow measurements in large scale open water environments (Dinehart & Burau, 2005b; Buschman et al., 2013; Sassi et al., 2013; Jamieson et al., 2011). Current techniques to process ADCP data (Kim et al., 2009; Le Bot et al., 2011; Parsons et al., 2013) assume homogeneous flow between the measured radial components of velocity, often referred to as radial velocities (Figure 4.1a). This homogeneity assumption is often questionable (Marsden & Ingram, 2004), but, nevertheless, widely applied. We propose a technique to process vessel mounted ADCP data that reduces the volume in which the flow is considered homogeneous. This volume is reduced by abandoning the standard procedure of combining inclined ADCP beams that measure simultaneously. Instead, we combine radial velocities based on their position within a predefined mesh (Figure 4.1a,b). The combination of several radial velocities leads to one, best fitting velocity, estimated with a least squares method. The velocity achieved by this approach can differ up to 40% from that obtained with the conventional approach.

ADCPs do not directly measure the Cartesian components of a velocity vector. The velocity vector can only be reconstructed by combining several radial velocities. This necessarily leads to the common

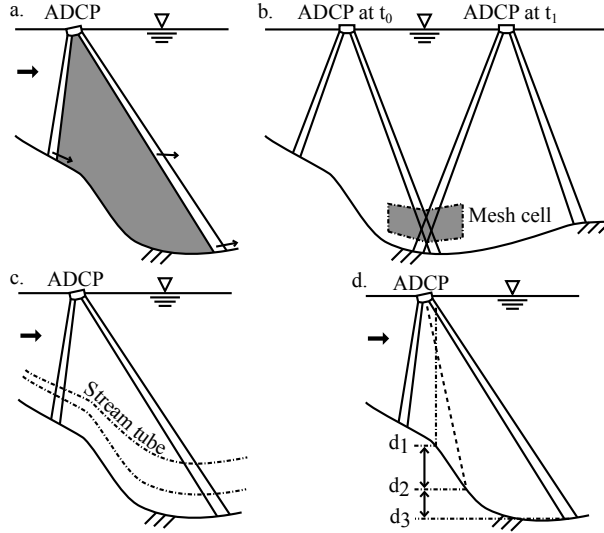


FIGURE 4.1. Tilting strongly affects the location where velocity is sampled (a). The large spread of the beams implies that, when combining velocity samples from different beams directly, the sampling volume is very large (gray area in a). This renders the location of the velocity estimate to be unclear. The assumption of flow homogeneity also fails due to the large sampling volume (a). A better approach is to combine velocity sampled in the same location (e.g. in a mesh cell indicated as the grey area in b) instead of combining velocity sampled simultaneously by the acoustic beams of the ADCP. When bed gradients are present, it is better to combine velocity samples from the same relative depth. Based on a continuity consideration, a stream-tube approach can be adopted (c). To determine the relative depth, the actual depth of the velocity sample (d_1 in d) must be determined. This can differ significantly from the depth at the end of an acoustic beam (d_3) or the average depth of the acoustic beams (d_2).

assumption of a homogeneous flow between the measuring locations of the radial velocities. The set of radial velocities that leads to a flow velocity estimate directly determines the extent over which the flow is assumed homogeneous.

At present, vessel mounted ADCP data processing techniques typically solve for the velocity based on - generally three to four - radial velocity components. These radial velocity measurements originate from the three or four available acoustic beams and are collected during one measuring cycle, and at one specific depth (Marsden & Ingram, 2004; Kawanisi, 2004; Kim et al., 2009; Le Bot et al., 2011; Parsons et al., 2013; Tokyay et al., 2009; Muste et al., 2010; Nystrom et al., 2007; Gargett, 1994). Since acoustic beams diverge with distance from the ADCP, the distance among the measured radial velocities increases when moving away from the ADCP (Figure 4.1a). This results in an increase of the volume in which the flow is assumed homogeneous. Although this homogeneity assumption is widely applied, it is likely to fail.

A way to deal with this inhomogeneity is to apply a correction to account for first order shearing in the flow (Marsden & Gratton, 1997; Marsden & Ingram, 2004; Kawanisi, 2004). This correction is achieved by Taylor expansion of the solution of the velocity vector. These corrections were derived for three beams (Kawanisi, 2004) and four beams systems (Marsden & Gratton, 1997; Marsden & Ingram, 2004). With these corrections, the flow is no longer assumed to be constant, but may vary linearly within the measuring volume. The volume in which linear change of the flow is assumed remains, however, unchanged.

There are several conditions that may lead to flow inhomogeneity. Turbulence causes both spatial and temporal variations in the flow. An instantaneous ADCP velocity measurement therefore contains contributions by the mean flow, turbulence and instrumental noise. Typically, the contribution by turbulence overwhelms the noise effect (Lu & Lueck, 1999a, Chapter 4). Turbulence-induced time variations require vessel mounted ADCP transects to be navigated repeatedly at the same cross-section (Szupiany et al., 2007; Tarrab et al., 2012). This allows to isolate the mean flow contribution. Turbulence-induced spatial variations affect the quality of velocity estimates by introducing flow inhomogeneity, when the scales involved are smaller than the distance between the acoustic beams (Marsden & Ingram, 2004).

Other sources of inhomogeneity include large gradients in bed topography, mixing layers at confluences and secondary flows at river bends, which can result in considerable spatial gradients in the mean flow velocity field (Figure 4.1c).

We introduce a generic approach to estimate flow velocity given an arbitrary set of radial velocities in Section 4.2. We explain how to estimate the variance in flow velocity and we define the mesh in which we estimate velocity. Subsequently we give more details about the estimation of ship velocity, defining sections, positioning the velocity data and non-dimensionalizing the depth. The method is applied to two field cases, yielding results presented in Section 4.3. These results specifically address the homogeneity assumption and the role of turbulence. We discuss the results and draw conclusions in Section 4.4.

4.2 Method

Estimating velocity

Given an arbitrary set of measured radial velocities, we intend to find a ‘best fit’ mean velocity vector, representing the average over the time span of available transect data. Radial velocities measured within a predefined volume contain information about the average velocity of the flow in that volume. The radial velocity measured by an ADCP is the projection of the velocity vector in the direction of the acoustic beam. The direction of the acoustic beam can be described by a unit vector \mathbf{q} . The measured radial velocity b relates to the velocity \mathbf{v} as:

$$b = \mathbf{v} \cdot \mathbf{q} = \mathbf{q}^T \mathbf{v} \quad (4.1)$$

If we consider a set of N radial velocity samples we can write:

$$\begin{pmatrix} b_1 \\ \vdots \\ b_N \end{pmatrix} = \begin{pmatrix} \mathbf{q}_1^T \\ \vdots \\ \mathbf{q}_N^T \end{pmatrix} \mathbf{v} \iff \mathbf{b} = \mathbf{Q} \mathbf{v} \quad (4.2)$$

where \mathbf{v} may be replaced with a Taylor expansion around the center of the volume spanned by a set of radial velocities (Marsden

& Ingram, 2004; Kawanisi, 2004) to account for remaining inhomogeneities. In practice, the radial velocity will be affected by instrument noise, the effect of turbulence, spatial inhomogeneity and other errors:

$$\mathbf{b} = \mathbf{Q}\mathbf{v} + \boldsymbol{\epsilon} , \quad (4.3)$$

in which $\boldsymbol{\epsilon}$ is the combined effect of all errors. The solution for the velocity is found in such a way that the sum of squared errors $\hat{\mathbf{e}}^T \hat{\mathbf{e}}$ is minimized. The estimate of the velocity \mathbf{v} reads (Johnson & Wichern, 2007, Chapter 6):

$$\hat{\mathbf{v}} = \mathbf{Q}^+ \mathbf{b} , \quad (4.4)$$

in which $\mathbf{Q}^+ = (\mathbf{Q}^T \mathbf{Q})^{-1} \mathbf{Q}^T$ is the generalized inverse of \mathbf{Q} . The matrix \mathbf{Q} can be rank deficient when the number of radial velocity estimates included is too small. A single repeat-transect already yields sufficient samples to invert \mathbf{Q} , provided the vessel speed is not too high.

Estimating velocity variance

The residuals $\boldsymbol{\epsilon}$ can be estimated as

$$\hat{\mathbf{e}} = \mathbf{b} - \mathbf{Q}\hat{\mathbf{v}}. \quad (4.5)$$

From this we can also obtain the covariance matrix of the velocity estimator (Johnson & Wichern, 2007)

$$\text{var}(\hat{\mathbf{v}}) = \frac{\hat{\mathbf{e}}^T \hat{\mathbf{e}} (\mathbf{Q}^T \mathbf{Q})^{-1}}{N - 3} . \quad (4.6)$$

This relates to the velocity covariance as in:

$$\text{var}(\hat{\mathbf{v}}) = \frac{\text{var}(\mathbf{v})}{N} . \quad (4.7)$$

The estimate of residuals in radial velocity can be used to remove possible outliers.

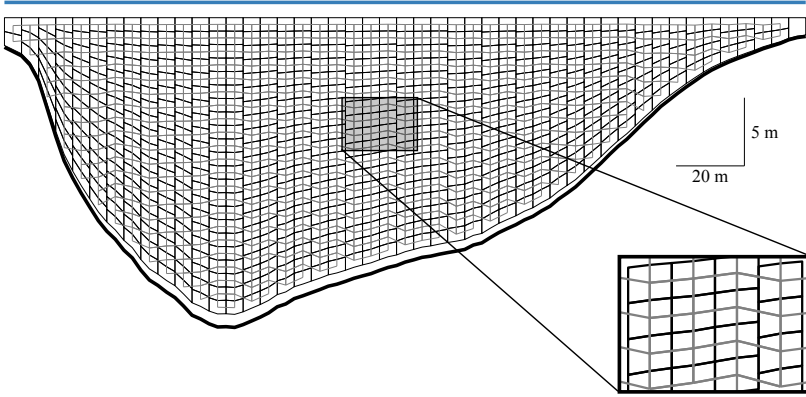


FIGURE 4.2. Example of a mesh generated for velocity processing at section 8 (Figure 4.4). The mesh follows in each vertical the bed in the same way a σ -mesh would do, but has a varying number of cells in the vertical, to ensure a nearly equal number of velocity samples in each mesh cell. The gray lines indicate the connectivity between the cells, necessary for the computation of derivatives.

Meshing

The navigated section during a repeat transect can be subdivided in small volumes by defining a mesh. All radial velocities within a mesh cell, from several repeat transects, are used to solve for the flow velocity according to Section 4.2.

The mesh generation procedure starts by subdividing the section in vertical slices with a user-defined width (Δn). The lower boundary of the mesh is set to the lowest part of the water column not influenced by side-lobes (in our case 0.06 of the water depth). The upper boundary is determined by the highest location where a radial velocity sample is available.

Subsequently, each of the vertical slices is split in several cells. The available vertical distance is subdivided in an integral number of parts such that the given vertical mesh size (Δz) is best resembled. A mesh cell will have six edges, two on the left side, two in the middle and two on the right side (see mesh in Figure 4.2). Eventually, the vertical z coordinates of the mesh are converted to non-dimensional coordinates σ , as defined in Equation 4.11. The

mesh itself defines an intrinsic coordinate system (v, ζ) , corresponding to rows and columns. The connectivity of neighboring cells is chosen such that the vertical coordinate z remains relatively constant for a constant value of ζ (Figure 4.2). Since this is not everywhere the case, we need to apply a correction to the computation of the derivatives. The gradient of a quantity defined on the mesh can be computed as:

$$\begin{pmatrix} \frac{\partial}{\partial n} \\ \frac{\partial}{\partial z} \end{pmatrix} = \begin{pmatrix} \frac{\partial v}{\partial n} & \frac{\partial \zeta}{\partial n} \\ \frac{\partial v}{\partial z} & \frac{\partial \zeta}{\partial z} \end{pmatrix} \begin{pmatrix} \frac{\partial}{\partial v} \\ \frac{\partial}{\partial \zeta} \end{pmatrix} \quad (4.8)$$

where n is the horizontal coordinate on the section plane. All derivatives are approximated based on central differences.

Estimating ship velocity

The raw radial velocity samples have to be corrected for the ship velocity. One way to estimate ship velocity is to use a so-called bottoming, which estimates the vessel speed with respect to the river bed, assumed to be fixed. This method fails when the range to the bed is too high, or when the river bed is moving due to bed-load sediment transport (Rennie et al., 2002; Sassi et al., 2011b). An alternative method requires the use of an accurate GPS to estimate ship velocity. In this study, all raw radial velocities were corrected for the ship velocity, transformed to radial components, based on differential GPS data. The use of GPS as a reference is not a prerequisite for the application of the proposed method.

Transect splitting and section definition

The track navigated by the vessel during data collection is defined by all positions of the ADCP, p_a , expressed in a projected geographic coordinate system (x, y, z) , and usually collected with a GPS device (The vertical component z of p_a is set to the draft of the ADCP transducers). The track is split into single crossings, each belonging to a river section (Figure 4.3 and Figure 4.4), based on which the data will be further processed. For each section we define a direction, which together with the vertical (k), defines a plane on which the

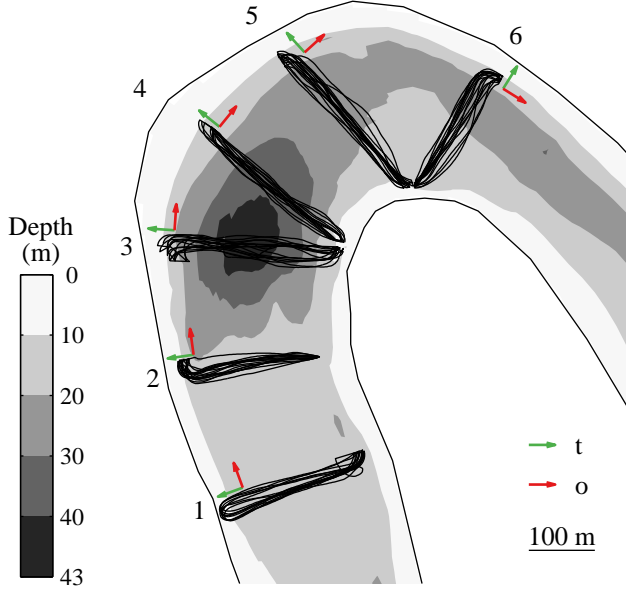


FIGURE 4.3. Track navigated by the vessel, included in the data processing at a sharp bend exemplifying the new method. The flow in the figure is in the direction of the o vectors. The track is divided in several sections indicated by a number. For each section the along section direction t and orthogonal direction o is indicated by the arrows in the colors green and red, respectively.

data will be projected. The direction of a section t is determined as the largest eigenvector of the covariance matrix of p_a . The horizontal direction, orthogonal to t , is defined by the unit vector o (Figure 4.3 and Figure 4.4). Any position p is transformed to a coordinate system defined on the section plane

$$\begin{pmatrix} s \\ n \\ z \end{pmatrix} = \begin{pmatrix} (p - \overline{p_a}) \cdot o \\ (p - \overline{p_a}) \cdot t \\ p \cdot k \end{pmatrix}, \quad (4.9)$$

where $\overline{p_a}$ denotes the average of all track positions belonging to a certain section.

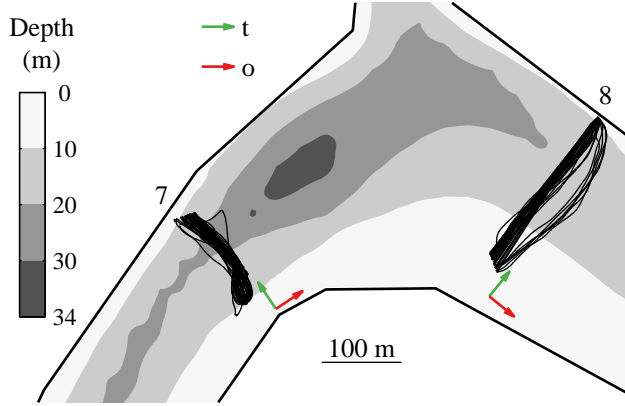


FIGURE 4.4. The track navigated by the vessel is divided in two sections indicated by numbers. The flow in the main channel at the bottom of the figure is in the direction of the o vectors. The flow in the side-channel at the top is from top to bottom. For each vector, the along section direction t and the orthogonal direction o is indicated by the arrows in the colors green and red, respectively.

Positioning of radial velocities

The location of the radial velocity sample determines which mesh cell the radial velocities belong to. In an ADCP centered coordinate system, the spatial orientation of the acoustic beams of an ADCP can be described by a unit-vectors \tilde{q} for each beam. To account for the orientation of the ADCP during data collection, we need to rotate the coordinate system to the projected geographic coordinate system $q = \mathbf{T}\tilde{q}$. The rotation matrix \mathbf{T} is usually composed of three consecutive rotations in space that transform the ADCP-fitted coordinate system to a projected geographic coordinate system. The definition of \mathbf{T} will mainly depend on the way the instrument measures the three consecutive rotations. The position of a radial velocity measurement at a range r from the instrument is

$$p = p_a + rq. \quad (4.10)$$

The same approach is followed to determine the position of the bed based on the range to the bed measured by the ADCP.

Non dimensional depth

Commonly, when processing ADCP data, the depth detected at the end of the beam is considered representative for all measurements performed along that beam. This can be correct when the gradient in the bed elevation is limited. When strong bed level gradients are present, the depth at a velocity measurement can be quite different from the depth at the end of the acoustic beam (see [Figure 4.1d](#)). The proper depth at each radial velocity is found by interpolation from a pre-determined bathymetry. This bathymetry is constructed using all depth measurements obtained with the ADCP. For each velocity measurement position, p_v , we therefore find the corresponding bed position p_b . With the obtained bed position we non-dimensionalize the vertical coordinate:

$$\begin{pmatrix} s \\ n \\ \sigma \end{pmatrix} = \begin{pmatrix} (p_v - \overline{p_a}) \cdot o \\ (p_v - \overline{p_a}) \cdot t \\ 1 - \frac{p_v \cdot k - \eta}{p_b \cdot k - \eta} \end{pmatrix}, \quad (4.11)$$

where η is the fluctuation of water level around the mean water level at which $z = 0$.

4.3 Results

We process two datasets according to the proposed method. The data were collected at two locations along the Mahakam River, East Kalimantan, Indonesia. This river features several bends with very deep scour holes often exceeding three times the average depth, reaching depths of typically 45 m ([Chapter 3](#)). We selected two locations, one featuring a strongly sheared flow near a sharp bend ([Figure 4.3](#)) and another at a mild bend near a junction ([Figure 4.4](#)).

The two datasets are processed both according to the proposed method and according to the conventional processing approach. The conventional method differs from the proposed method only in the way velocity vectors are estimated, i.e. directly from simultaneously measured radial velocities, from each of the four ADCP beams.

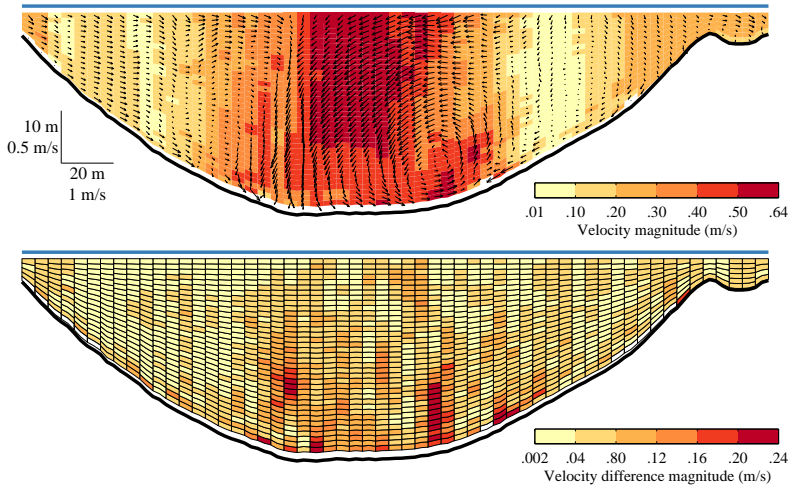


FIGURE 4.5. The top panel shows the flow pattern at section 3 (Figure 4.3) based on the proposed method. The colors indicate the longitudinal velocity component, while the arrows indicate the velocity components in the section-plane. In horizontal direction, there is a strong shearing in the flow. This results in large differences between the conventional processing method and the method proposed.

Flow inhomogeneity

At large distance from the ADCP, differences between the two methods are most pronounced, because the beam spreading increases with depth from the surface. The difference between the two methods reaches in some areas values of 0.24 m/s, which is a significant portion of the total magnitude of the estimated velocity (Figure 4.5). These large differences not only occur in sections with complex flows. Also at section 7, with a relatively simple flow pattern including a secondary circulation cell due to curving of the river, differences are high compared to the total magnitude of the velocity (Figure 4.6). The vertical component in the uppermost velocity estimates appears to be biased low. This can be attributed to the effect of the vessel interfering with the flow (Tokyay et al., 2009; Muste et al., 2010; Jamieson et al., 2011).

Thirty percent of the cells have a relative difference in longitu-

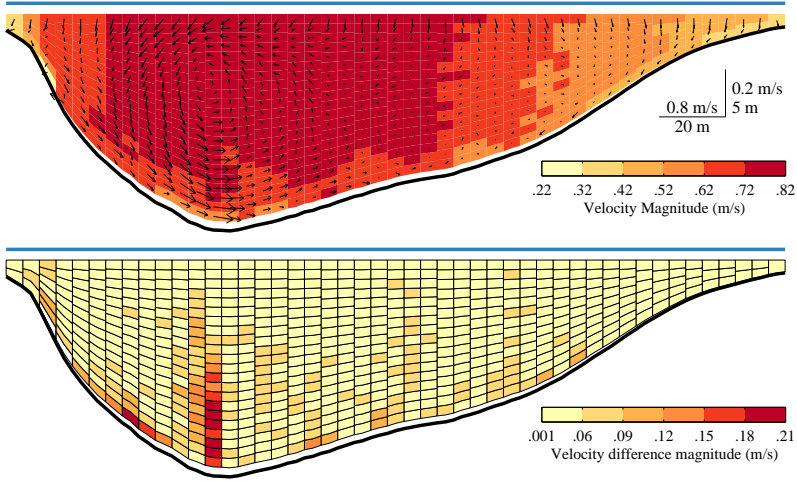


FIGURE 4.6. Secondary flow at section 8 (Figure 4.4) based on the proposed method (top panel). The flow is typical for a mildly curved bend. The magnitude of velocity differences between results from the proposed and the conventional methods shows large differences where the flow is inhomogeneous over the area between the acoustic beams (bottom panel).

dinal velocity between 0 and -10% (Figure 4.7). The difference in longitudinal velocity between the two methods can exceed 20 cm/s. When integrated over the cross-section, differences become insignificant. This shows that the conventional method acts as an effective smoother, such that variance is reduced, but the longitudinal flow is preserved.

Velocity estimates differ most in the cross-stream and vertical direction (Figure 4.7b,c). Only about 15% of the cross-sections have a relative difference in velocity magnitude of less than 10%. The remainder of the cross-sections show larger differences. The new method results in secondary flow velocity estimates which are markedly different from those obtained with the conventional method. The large number of samples with differences exceeding 100% is mainly resulting from low values of secondary velocity.

The streamwise vorticity of the flow (Figure 4.8) seems smoother in the conventional method compared to the proposed method. The reason for this can be the fact that the conventional method com-

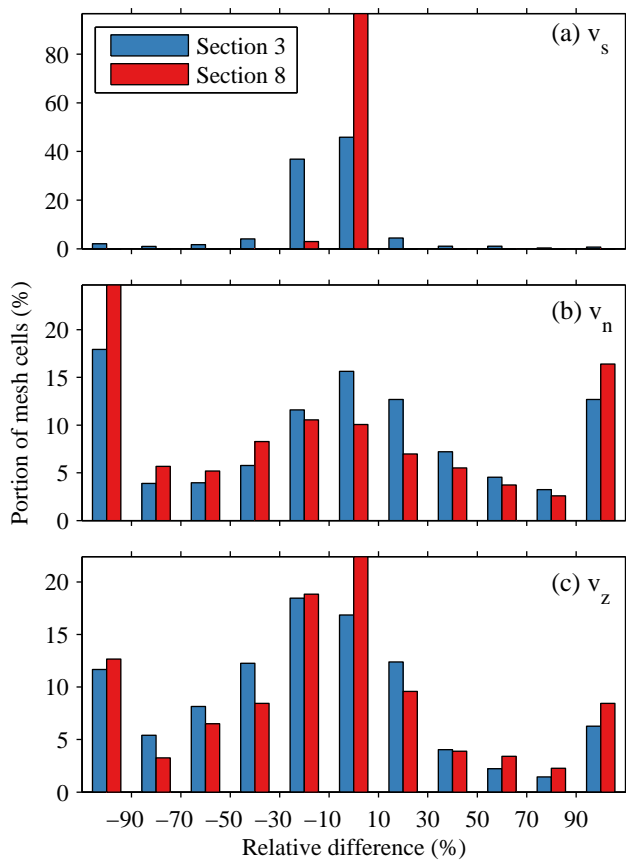


FIGURE 4.7. Histograms of relative error in the streamwise (a), cross-stream (b) and vertical (c) velocity components at section 3 and section 8. A positive error indicates an overestimation based on the conventional method.

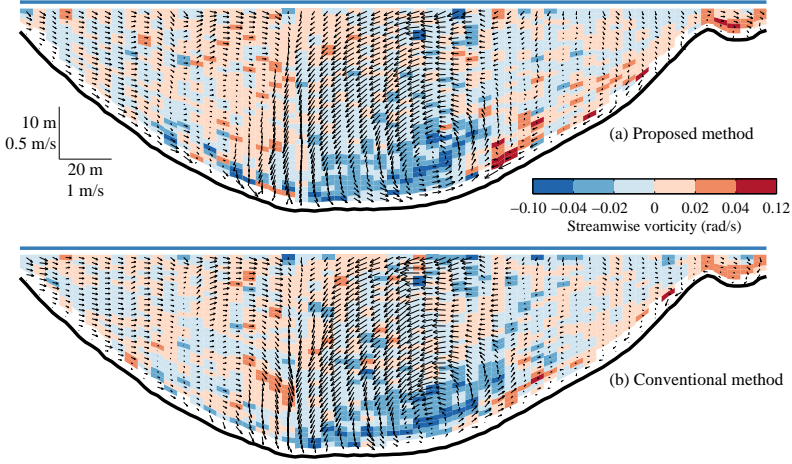


FIGURE 4.8. Streamwise vorticity for section 3, determined with the proposed method (a) and with the conventional method (b).

bines velocity samples collected at much larger distances than the proposed method, introducing spatial smoothing. The secondary flow patterns are different between the two methods. A secondary flow cell clearly visible in the results obtained with the proposed technique is resolved differently in the results obtained with the conventional method (Figure 4.8). The core of the secondary flow cell is located closer to the bed in the conventional method and below the core no flow toward the inner bank (to the right in Figure 4.8) is observed. The largest differences in secondary flow occur at locations with strong shearing.

Turbulence and inhomogeneity

The estimated variances (Equation 4.6 and Equation 4.7) of the velocity are strongly influenced by the flow inhomogeneity within a mesh cell. The estimated variance for the conventional method is determined as the variance of the Cartesian estimators of velocity within a mesh cell. We can expect this variance to be biased low, compared to the variance estimated for the proposed method, since we do not take into account the variance in the initial radial velocities.

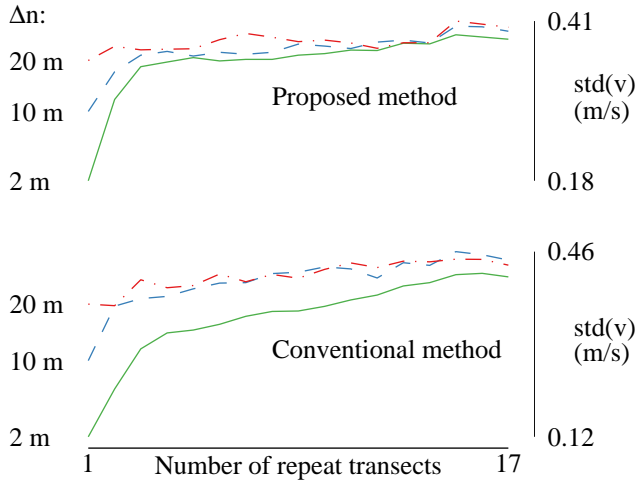


FIGURE 4.9. Standard deviation of the velocity estimated at section 3. The top graph is based on results from the proposed method. The lower graph is based on results from the conventional method. River crossings were progressively included to estimate the standard deviation in velocity, for different horizontal mesh cell sizes.

When more repeat transects are included in the estimate of the velocity variance we expect the variance to increase until enough repeat transects are included. The variance will only reach a stable value under steady flow conditions (Soulsby, 1980). Once a stable value of the variance estimate is obtained, it is reasonable to conclude that enough data were collected to obtain a robust estimate of the mean velocity vector. This analysis was performed with different cell sizes (Figure 4.9).

For section 3, the variance is increasing when more repeat transects are included. This is attributed to a higher temporal coverage of turbulence induced fluctuations. At a certain number of repeat transects, the estimated variances in velocity stabilize. Typically, four to five repeat transects are needed when using the proposed method, while many more transects are needed when the conventional method is adopted. The improvement in variance convergence is most pronounced for smaller mesh cell sizes. This can be explained

by the fact that the current method provides the largest improvements when the cell size is much smaller than the beam spread.

The estimates of variance, which is mostly caused by turbulence, benefit more from the inclusion of additional repeat transects than from a larger mesh cell size. These results confirm earlier findings by [Tarrab et al. \(2012\)](#). Increasing the mesh cell size, or applying a spatial smoother, only improves the estimates of the spatially induced variance. The temporal component of the variance is strongly improved when including more repeat transects. Due to ship motions, this variance cannot be used to estimate turbulence properties ([Lu & Lueck, 1999a](#)).

4.4 Discussion and conclusions

A new method is proposed to yield improved velocity estimates from moving boat measurements. The new method abandons direct combination of velocity estimates from the four acoustic beams to a Cartesian velocity vector, which is intuitively appealing, and has gained wide acceptance. Since the acoustic beams are divergent and sample synchronously, velocity estimates from three beams at the same horizontal level yield the instantaneous Cartesian velocity vector, provided that the instantaneous velocity field between the three beams at that level is spatially homogeneous. The latter assumption is largely valid for the mean flow, but not for turbulence-induced velocity fluctuations ([Chapter 6, Stacey et al., 1999a](#)). To some degree, the fourth acoustic beam can be used to reduce the effect of spatial inhomogeneity of turbulent fluctuations, but repeat transects are indispensable to remove it completely, and to take out the effect of temporal variation. In the new method, the mean Cartesian velocity vector is retrieved in a single step based on a least squares procedure.

The proposed method reduces the spatial extent of the region over which turbulence-averaged properties are assumed to be homogeneous, which applies both to the conventional and to the proposed method. In the conventional approach, the quality of the velocity estimates generally deteriorates with distance from the transducer, because of the increasing aperture between the beams. Also, instrument tilts directly lead to a loss of accuracy, depending on the distance to the transducer. The new approach features a very generic way of

dealing with beam spreading and instrument tilts, and can be applied to any beam configuration. It can also be extended to perform a first order correction for the inhomogeneity (Marsden & Ingram, 2004; Kawanisi, 2004).

The method is shown to provide results that differ from results obtained with conventional processing methods. The method allows to better recognize secondary flow cells. Beam divergence acts as a spatial filter (González-Castro & Muste, 2007), with a filtering window that increases with distance from the ADCP transducer. This leads to a reduction of the variance in velocities, but leaves the cross-section integrated velocity unaffected.

Our results confirm earlier findings of Szupiany et al. (2007) and Tarrab et al. (2012), who argue that several repeat transects are needed to obtain robust estimates of the turbulence averaged velocity. The proposed method seems to reduce the minimum number of repeat transects needed. When estimating the variance in velocity, progressively including more repeat transects is shown to be an effective method to assess the effect of turbulence-induced inhomogeneities on the estimated velocity. A single repeat-transect already yields sufficient data to estimate the velocity vector, which holds both for the proposed method and for the conventional method. The inclusion of a larger number of repeat-transects serves to isolate the mean velocity vector, but is not a prerequisite to apply the proposed method. Mean velocity estimates obtained either from the conventional method or from the new method suffer from errors in positioning and projection, essentially in the same way. The solution to the problem of beam divergence presented here comes at no extra cost other than restrictions to the mesh, to guarantee enough velocity samples in each mesh cell.

The new method can have far-reaching implications for those using vessel mounted ADCPs for flow velocity measurements. The relevance for procedures to obtain river discharge (e.g. Gordon, 1989; Le Coz et al., 2008; Nihei & Kimizu, 2008; Sassi et al., 2011b; Hidayat et al., 2011) is limited, since cross-section averaged velocity is largely unaffected. Secondary flow patterns appear to be different with the proposed method, resulting in different positioning of the core of secondary recirculations. It will be particularly relevant for studies of complex geophysical surface flows, focusing on sediment transport (e.g. Rennie et al., 2002; Thorne & Hanes, 2002; Hoitink,

2004; Hoitink & Hoekstra, 2005; Kostaschuk et al., 2005; Parsons et al., 2005; Buschman et al., 2012; Moore et al., 2012; Sassi et al., 2012; Szupiany et al., 2012), flow division at bifurcations (e.g. Richardson & Thorne, 2001; Dinehart & Burau, 2005a; Sassi et al., 2012; Buschman et al., 2013) or detailed flow patterns related to channel junctions (e.g. Rhoads & Sukhodolov, 2001; Dinehart & Burau, 2005a; Lane et al., 2008) and near obstacles (e.g. Jamieson et al., 2011; Le Coz et al., 2010).

4.5 Software availability

The methods presented have been implemented in a set of open-source MATLAB functions. They have been made available [online](http://adcptools.googlecode.com) (<http://adcptools.googlecode.com>). Processing is performed combining binary input files and NMEA based ASCII input files.

Flow in a sharp river bend with a local increase in cross-sectional area

Abstract

Horizontal flow recirculation is often observed in sharp river bends, causing a complex three-dimensional flow structure with large implications for the morphological and planimetric development of meanders. Several field observations in small scale systems show that sharp bends are often found in association with a strong increase in cross-sectional area, the deposition of outer bank benches and reattachment bars near the inner bank. Recent studies show that these bends can also occur in large scale systems. In this study, we present field measurements of a sharp bend in the Mahakam River, East Kalimantan, Indonesia. The cross-sectional area increases by a factor three compared with the reach averaged cross-sectional area. The field

This chapter is based on: VERMEULEN, B., A.J.F. HOITINK, R.J. LABEUR, Flow in a sharp river bend with a local increase in cross-sectional area, *Submitted to J. Geophys. Res.: Earth Surf.*

measurements are analysed together with the results from numerical simulation with a 3D finite element model. The results show the importance of the increase in cross-sectional area in the development of horizontal recirculation. Strong downflow (12 cm s^{-1}) alters the hydrostatic pressure distribution and advects longitudinal momentum towards the bed, causing the flow to concentrate in the lower part of the cross-section. This increases the bed shear stress, which is expected to maintain the large scour depth found in several bends along the Mahakam River.

5.1 Introduction

Horizontal flow recirculation is often observed in sharp river bends (Carey, 1969; Woodyer, 1975; Page & Nanson, 1982; Hickin, 1986; Andrle, 1994; Ferguson et al., 2003; Blanckaert et al., 2013; Beltaos et al., 2012). Separation can occur near the inner bank or at the outer bank, and has large implications for the morphological development of river meanders. Separation at the outer bank can drive the deposition of a concave bank bench (Page & Nanson, 1982). At the inner bank, separation directs the flow to the outer side of the bend, resulting in strong vertical flow impinging on the bed (Hodkinson & Ferguson, 1998; Blanckaert, 2010). In sharp bends the cross-sectional area often increases (Blanckaert, 2010), sometimes dramatically (Andrle, 1994; Beltaos et al., 2012, Chapter 3). A recent field study (Chapter 3) has shown that along the Mahakam River sharp bends strongly correlate with deep scours and are a ubiquitous feature along an alluvial reach of the river with no consolidated outcrops. The scours found along a tropical river are similar to scours found in an Arctic region, in the Mackenzie Delta (Gharabaghi et al., 2007; Beltaos et al., 2012). These field observations strongly challenge our present knowledge of flow in sharp bends, which does not provide a satisfactory explanation for the formation of such scours.

In the present study, we investigate the flow at one of the sharp bends in the Mahakam River, Indonesia. Acoustic Doppler Current Profiler (ADCP) data are processed using a newly developed method (Chapter 4) that allows relaxation of the homogeneity assumption, which is likely to fail in the sheared flow conditions and large depths found in the bend under consideration. The field measurements are

complemented with results from a numerical model (Labeur & Wells, 2012). We show that the increase in cross-sectional area, occurring at sharp bends, can induce a strong adverse water surface gradient, which is one of the main drivers of flow reversal. A geometric analysis of the Mahakam River shows that increasing curvature results not only in an increase in scour depth, but also in the total cross-sectional area. The local increase of cross-sectional area results in a reversed Venturi effect, explaining recirculation at the banks.

5.2 Field measurements

Location

Flow data were collected in a sharp bend (Figure 5.1) of the Mahakam River, East Kalimantan, Indonesia. This bend is located in the Mahakam lakes region and is representative for a large number of sharp bends with deep scours found in this region (Chapter 3). The river bend features a minimum radius of curvature of 216 m and a mean width of about 235 m. Just before the point of maximum curvature the depth reaches a maximum of 43.5 m. The bend also widens until a maximum width of 307 m. The cross-sectional area increases from about 2200 m² up to 7000 m².

The flow data were collected using a 1200 kHz acoustic Doppler current profiler (ADCP), mounted on a vessel looking downward into the flow. The vessel sailed a track along seven cross-sections each of which was navigated 16 times (Figure 5.1). During the survey, the water level remained constant with an average discharge of about 1700 m³ s⁻¹. Bed samples taken in the bend were mostly composed of fine sands. In the deep scour several samples were taken containing mostly clay.

Geometric analysis

The river centreline was extracted from Landsat ETM+ images (Section 3.3). Given the Cartesian coordinates of the centerline x and y as a parametric function of s , the curvature C normalized by the width

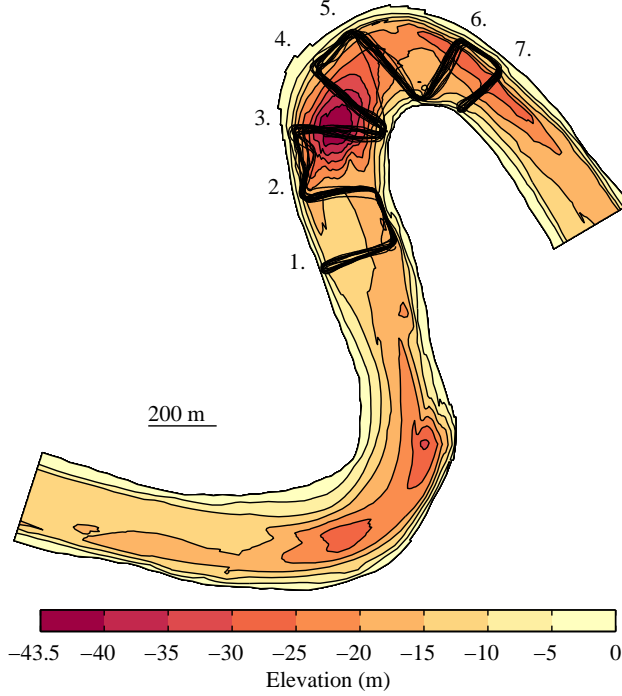


FIGURE 5.1. Track navigated by the research vessel during data collection. The color shades indicate the river bed elevation. The numbers next to the navigation track indicate the river crossing used for data processing.

W is computed as (Legleiter & Kyriakidis, 2006):

$$C = W \frac{x'y'' - y'x''}{(x'^2 + y'^2)^{\frac{3}{2}}}, \quad (5.1)$$

in which the prime (') denotes a derivative with respect to s .

The depth of the river, obtained with a single beam echo-sounder and corrected for water level fluctuations, was used to determine the depth-excess parameter D_{ex} . This parameter is defined as:

$$D_{\text{ex}} = \frac{D_{\text{max}}}{D_{\text{ls}}} - 1 \quad (5.2)$$

where D_{ls} is the regional mean depth, i.e. the mean depth low-pass filtered to retain the regional mean-depth fluctuations and D_{max} is defined as the local maximum depth. For example, this means that when this parameter is equal to one, the maximum depth is double the mean depth (Figure 3.3). From the depth, the cross-sectional area was determined. The cross-sectional area was used to define the area-excess parameter A_{ex} :

$$A_{ex} = \frac{A}{A_{ls}} - 1 \quad (5.3)$$

where A_{ls} is the regional cross-sectional area, i.e. the mean depth low-pass filtered to retain the regional area variation.

ADCP data processing

The collected ADCP data were processed with a method that allows to reduce the extent of the homogeneity assumption (Chapter 4). This assumption is needed when combining the raw radial components of velocity collected by an ADCP. Conventional processing techniques combine raw velocity components that are collected simultaneously at a significant distance. The method used in this study combines raw components collected in a predefined cell. This reduces the volume in which the flow is considered homogeneous from the distance between the beams to the size of a cell (Chapter 4).

5.3 Numerical modeling

The flow in the sharp bend was simulated using a finite element model (Labeur & Pietrzak, 2005; Labeur & Wells, 2007), which combines the upwinding possibilities of discontinuous Galerkin methods while preserving the low number of degrees of freedom typical of a continuous Galerkin approach (Labeur & Wells, 2007). The model is three-dimensional and can handle a non-hydrostatic pressure distribution. It has a moving surface boundary that allows to solve the free water surface (Labeur & Wells, 2009). Large eddy simulation was used as the turbulence closure solution.

The domain of the model includes an upstream bend and the bend under consideration. The banklines were defined at a water depth of 20 cm. The mesh was generated with a uniform mesh size

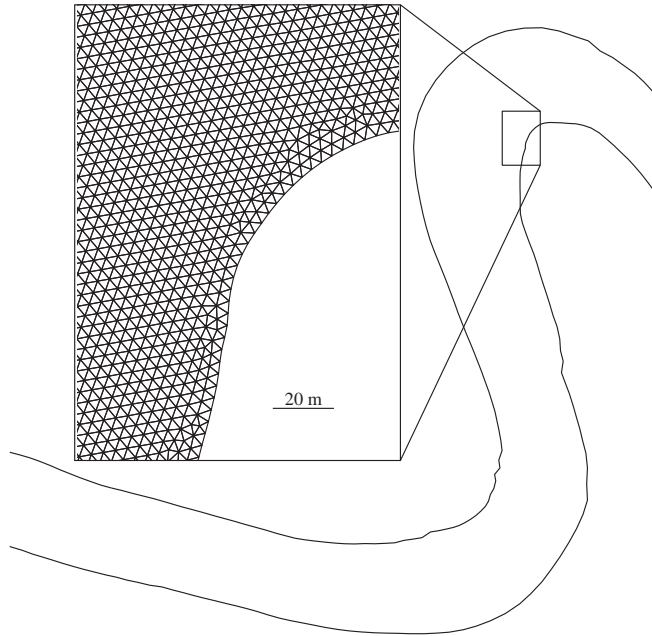


FIGURE 5.2. Detail of the computational mesh, generated with an element size of 4 m.

of 4 m (Figure 5.2). The upstream boundary conditions were set to a constant discharge of $1700 \text{ m}^3 \text{ s}^{-1}$ and the downstream boundary conditions were set to a fixed water level. Both were estimated from the ADCP measurements. Each computation simulated 7 h of flow with a time step of 3 s.

Model calibration

To allow for comparison between the model and the field measurements, the model results were linearly interpolated to the mesh used for field data analysis (Chapter 4). The model was calibrated changing the roughness parameterized by the Nikuradse length. The calibration focused on the scour region including cross-sections 2 through 4 (Figure 5.1). The root mean squared error was computed resulting in the lowest values for a Nikuradse length of 4 mm (Figure 5.3). The

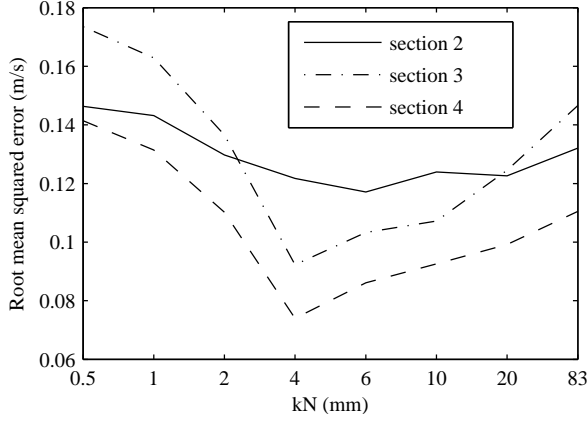


FIGURE 5.3. Calibration of the model for different roughness values (k_N). The lowest root mean squared error is obtained for a roughness of $k_N = 4$ mm

cross-stream flow components v and w correspond well with the observed values. The correspondence of the modeled and measured velocity components is limited for the longitudinal flow at cross-section 2, upstream of the scour. The correspondence improves for cross-sections 3 and 4 and is best for a Nikuradse length of 4 mm (Figure 5.4). The cross-stream flow components v and w correspond well with the observed values.

5.4 Results

Geometry

The depth excess and the area excess are compared with curvature. The curvature was used to define inter-quantile range classes to ensure an equal number of data in each class. For increasing curvature, both the depth excess and the area excess increase in a similar way (Figure 5.5). This shows that the cross-sectional area gradually increases for increasing bend sharpness. At sharply curved bends the cross-sectional area seems to become more constant, although a slight increase is still observable.

5. FLOW IN A SHARP AND WIDE BEND

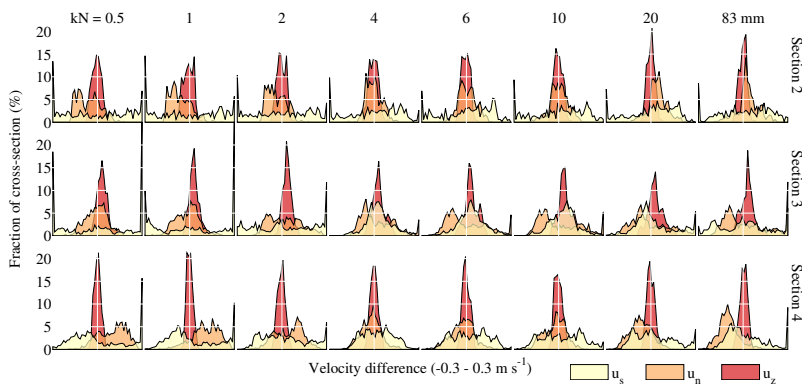


FIGURE 5.4. Histograms of the difference in velocity between the modeled and measured velocity components u_s , u_n and u_z . Every row corresponds to a cross-section (Figure 5.1), and each columns corresponds to a roughness k_N .

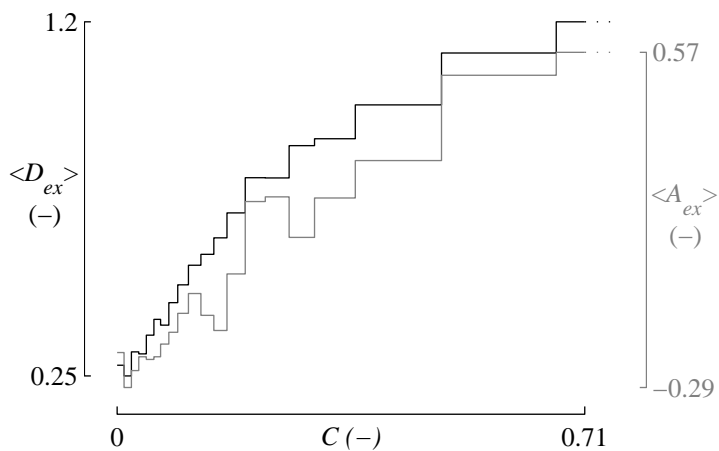


FIGURE 5.5. Depth excess and area excess averaged for interquantile range classes of curvatutre.

Depth-averaged flow structure

The depth-averaged flow features two large recirculation cells adjacent to the scour, just before the location where the highest curvature occurs (Figure 5.6). The two cells reduce the width of the cross-section carrying discharge. The incoming upstream flow converges horizontally, forming a jet-like structure between the two recirculating cells. After the scour, the flow strongly diverges horizontally. At the bend apex, the flow is nearly uniform over the width and near the inner bank the flow is directed to the downstream channel. After the apex, the flow restores a typical bend flow profile, with the core of the flow near the outer bank.

Adverse water surface gradients are a necessary, but not sufficient condition to cause separation of the flow (Blanckaert, 2010). The adverse water surface gradients are generated by sudden changes in curvature and are counteracted by the surface slope induced by roughness. This leads to the following relation (Blanckaert, 2010; Blanckaert et al., 2013):

$$\frac{\partial z_s}{\partial s} = -C_f Fr^2 + Fr^2 \frac{\partial}{\partial s} \left(\frac{H}{R} \right) n \quad (5.4)$$

where z_s is the water surface, s is the downstream distance along the centerline, C_f is a friction factor, Fr is the Froude number, H is the mean depth, R is the local radius of curvature and n is the transverse coordinate. The first term on the right hand side of Equation 5.4 is the effect of roughness and the second term is the adverse longitudinal gradient induced by transverse tilting of the water surface, caused by changes in curvature.

The curvature-induced adverse water surface gradient is a function of n , which means that in the outer side of the bend, it will cause an adverse gradient, while in the inner side it will decrease the downstream gradient. Apart from changing curvature an often observed phenomenon is the increase in cross-sectional area at sharply curved bends. The increasing cross-sectional area will decelerate the flow causing an increase in pressure which will result in an adverse water surface slope.

Including the effect of the increasing cross-sectional area we ob-

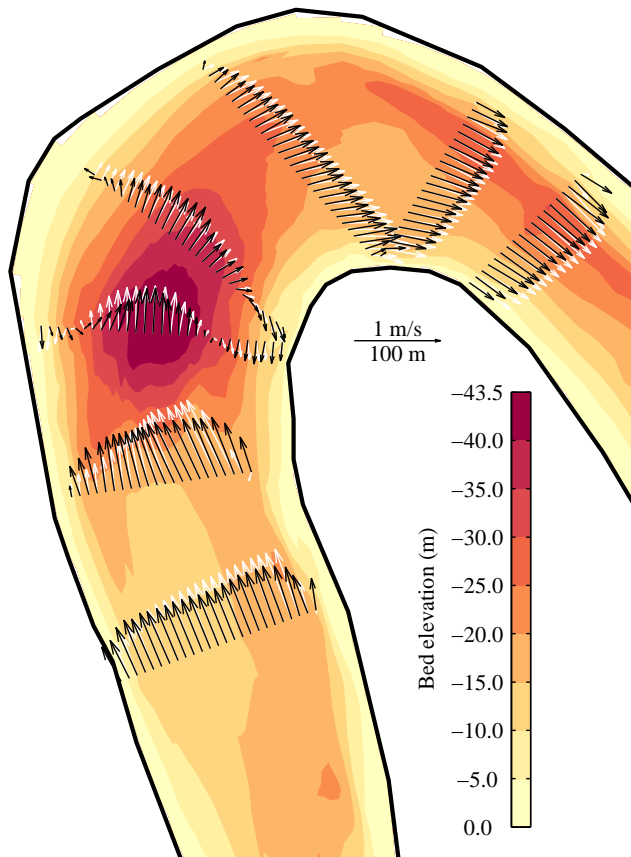


FIGURE 5.6. Measured and modeled depth-averaged velocity. The color shades indicate the bed elevation, the black arrows represent the measured depth-averaged flow and the white arrows indicate the modeled depth-averaged flow.

tain the following relation:

$$\frac{\partial z_s}{\partial s} = -C_f Fr^2 + Fr^2 \frac{\partial}{\partial s} \left(\frac{H}{R} \right) n + \frac{Fr^2}{W} \frac{\partial A}{\partial s} \quad (5.5)$$

where W is the river width and A is the cross-sectional area. This last term becomes important when significant changes in cross-sectional area occur in the longitudinal direction. We can quantify each of the terms above for the outer side of the bend considered here.

At the scour we can see both the effect of the changing curvature (Figure 5.7a) and the increase in cross-sectional area (Figure 5.7b) induce an adverse water surface gradient. The dramatic increase in cross-sectional area in this bend induces an adverse gradient which is steeper than the adverse gradient induced by curvature (Figure 5.7). This suggests that in this bend the non-uniformity induced by the increase in cross-sectional area is the dominant factor inducing flow recirculation at the outer side.

The changing curvature steers surface elevation contour lines to become more or less parallel to the streamwise coordinate. Variation in cross-section area causes a rise in the water level over the full width of the channel, overwhelming the curvature effect. The combined effect of friction, curvature and increase in cross-sectional area (Figure 5.7c) features an adverse gradient both in the inner and in the outer bend. The predicted water surface topography from Equation 5.5 is quite similar to the predictions of the numerical model. Variation in cross-sectional area is therefore expected to play a crucial role in the development of both the inner and outer bank recirculation.

Three-dimensional flow structure

Details in the flow through the seven cross-sections reveal a complex three-dimensional flow throughout the meander bend. At cross-section 1) (Figure 5.8), the longitudinal flow shows two areas of high flow, one near the left side and one on the right side (looking downstream). Near the core of the flow on the right side the cross-section is a bit deeper. This is considered to be the effect of the upstream bend. The downward directed flow vectors in the topmost cells in the cross-sections are a measuring artifact (Chapter 4).

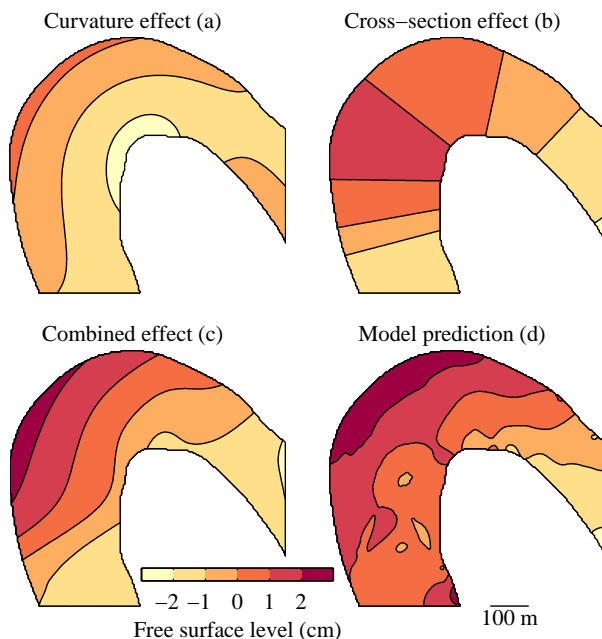


FIGURE 5.7. Water surface elevations based on Equation 5.5 and on the model results. (a) is the second right hand side term in Equation 5.5, (b) the third right hand side term, (c) the combined effect of the terms and (d) the water surface computed by the model.

Just upstream of the scour (Figure 5.8, cross-section 2) the flow converges horizontally and a small downward flow component develops, which is related to the downward slope of the bed at this location (Figure 5.1). At the scour (Figure 5.8, cross-section 3) the longitudinal flow is concentrated in the central part of the cross-section, with two recirculating zones next to it. The main longitudinal flow and the recirculating zones are separated by vertical shear layers. In the core of the flow the downward motion is intensified, reaching values of 12 cm s^{-1} .

A secondary cell is observed near the bed, at the inner bank side of the scour. A second, weaker, counter-rotating cell is observed near the surface at the outer bank side of the scour. In the area with strongest longitudinal velocity, the cross-flow is mostly directed

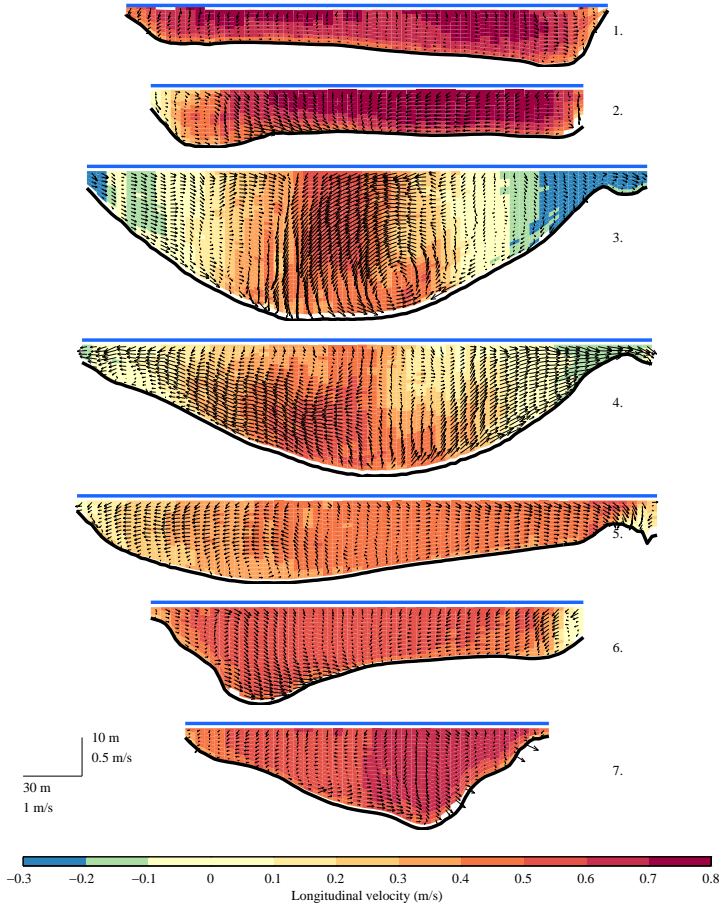


FIGURE 5.8. Measured velocity field at the seven cross-sections indicated in Figure 5.1. All profiles are plotted with the inner bank on the right side. The colored shades indicate the flow component in direction of the cross-sectionally averaged flow. The arrows indicate the flow orthogonal to the cross-sectionally averaged flow.

toward the outer bank, while in the recirculating area near the outer bank the cross-flow is predominantly directed to the inner bank. This indicates that the flow is still converging horizontally and is slowly being redirected to the outer bank.

At the downstream end of the scour (Figure 5.8, cross-section 4) the strong downward flow at the scour and the upward sloping bed both cause momentum to concentrate near the bed, where the core of the flow is found. The flow diverges again horizontally, causing the flow in the inner half of the cross-section to be directed into the outflow reach of the bend, while in the outer half it is directed to the outer bank. Although the flow is directed to the outer bank and is expected to impinge on it, no downward flow was observed near the outer bank. The impinging flow instead is recirculated upstream.

Near the bend apex (Figure 5.8, cross-section 5) the longitudinal flow is nearly uniform over the cross-section. A secondary cell is present near the bed. After the bend apex (Figure 5.8, cross-sections 6 and 7) the flow restores a typical mild bend flow pattern, with a recirculation cell representing outer bank directed flow near the surface and inner bank directed flow near the bed.

The strong vertical flow is expected to induce a non-hydrostatic pressure distribution near the scour, which is confirmed from the model results. At the cross-sections with strong vertical flow (cross-sections 3 and 4), the hydraulic head deviates from the head inferred from a hydrostatic distribution over a range of about 2 cm (Figure 5.9, cross-section 3). This is comparable to differences in the water surface level, ranging over about 1.5 cm at same cross-section. Since the modeled vertical flow velocity at cross-section 3 was underestimated, we can expect the occurring pressure to deviate even more from a hydrostatic pressure distribution than what is predicted from the model.

5.5 Discussion

The flow patterns observed in a very sharp bend of the Mahakam River is characterized by two zones of horizontal recirculation and high vertical flow velocity. These recirculations can be interpreted as a reversed Venturi effect essentially resulting from the local width increase. Similar flow patterns were previously observed, mainly in

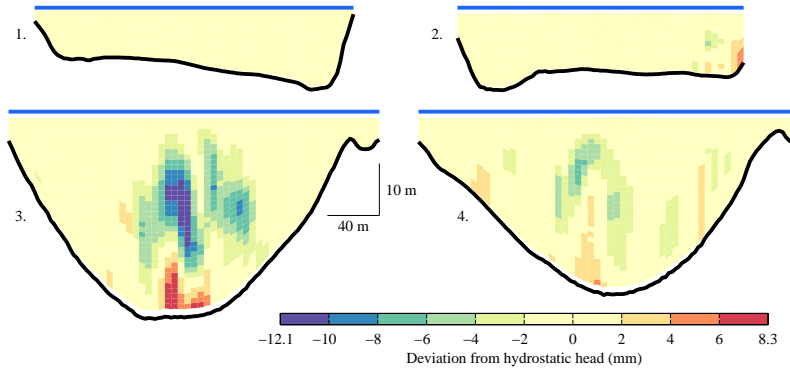


FIGURE 5.9. Modelled deviation of the piezometric head from a constant hydrostatic pressure distribution. Deviations from the hydrostatic pressure distribution are most pronounced near the scour where strong vertical velocity occurs.

small streams (Andrle, 1994; Nanson, 2010; Schnauder & Sukhodolov, 2012) and in a larger channel in the Mackenzie Delta (Gharabaghi et al., 2007; Beltaos et al., 2012). Often these flow patterns are associated with slow planimetric development (Beltaos et al., 2012, Chapter 3).

The model used in this study was able to properly reproduce the depth-averaged flow around the scour. The main shortcoming of the model was the reproduction of the strong vertical flow velocity, which was underestimated, and connected to this, the inability of properly reproducing the position of the core of the flow at the exit of the scour. The velocity core remains close to the surface in the model, while in the measurements the core is found near the bed. This shortcoming may be partly attributed to the LES turbulence closure approach. Curved shear layers and the associated production of turbulence kinetic energy in the interior of flow put the LES model to the test.

Existing criteria to determine possible flow separation near the banks (Blanckaert, 2010) do not take into account the effect of the increase in cross-sectional area. In the bend under consideration, the cross-sectional area becomes three times larger at the scour. When significant variation in cross-sectional area occurs, this becomes an

important mechanism causing adverse gradients and can readily be taken into account as a criterion for the inception of flow separation based on Equation 5.5. We show the cross-sectional area to increase gradually and systematically with increasing curvature. We expect flow reversal to become an increasingly dominant process for high curvature bends.

Although the flow pattern differs in many respects from what is usually observed in flume experiments on sharp bends, it is still possible to distinguish a main secondary flow cell located near the bed, and a second counter-rotating one near the surface. Typically, the main secondary cell has its core at about mid-depth (Blanckaert & de Vriend, 2004), while in this bend the core is located near the bed. Numerical simulations by Ferguson et al. (2003) also predict a secondary cell with its core near the bed. The counter-rotating cell, despite being weak, appears to be larger in size and located much closer to center of the channel. The main recirculation cell remains close to the bed until the exit of the bend, where it restores the typical position with its center at mid depth.

The secondary flow cell and the associated strong vertical flow velocity advects longitudinal flow momentum downwards, causing the core of the flow to be moved to the river bed at the downstream end of the scour. The downflow and the strong longitudinal velocity near the bed are expected to strongly increase the shear stress that the flow exerts on the river bed. Similar results were found by Blanckaert & de Vriend (2004); Ferguson et al. (2003); Schnauder & Sukhodolov (2012).

An important result from a modelling perspective is the non-hydrostatic distribution of pressure at the scour. A proper reproduction of the flow at such a scour requires a model that allows for a non-hydrostatic pressure distribution.

5.6 Conclusion

In this study we analyze the flow patterns of a sharply curved bend in the Mahakam River. The bend is characterized by an increase in cross-sectional area just before the bend apex, where the depth reaches three times the average depth. The increase in cross-sectional area is shown to play a crucial role in generating an adverse sur-

face gradient, a necessary condition for the formation of flow recirculation. A strong downflow develops near the scour that reaches 12 cm s^{-1} . This strong secondary flow distorts the vertical pressure distribution that is no longer hydrostatic. The vertical flow also advects longitudinal momentum moving the core of the flow to the bed of the channel, which is expected to locally increase the bed shear stress. This mechanism resulting in an increase in bed shear stress could be key to the maintenance of deep scours found along the lower parts of the Mahakam River (Chapter 3).

Coupled ADCPs can yield complete Reynolds stress tensor profiles in geophysical surface flows

Abstract

We introduce a new technique to measure profiles of each term in the Reynolds stress tensor using coupled acoustic Doppler current profilers (ADCPs). The technique is based on the variance method, which is extended to the case with eight acoustic beams. Methods to analyze turbulence from a single ADCP rely on questionable assumptions on turbulence anisotropy ratios and on the requirement of perfect vertical alignment, which are no longer necessary with the coupled system. We apply the technique successfully to data collected in the Mahakam River, East Kalimantan, Indonesia.

This chapter is based on: VERMEULEN, B., A. J. F. HOITINK, AND M. G. SASSI, 2011, Coupled ADCPs can yield complete Reynolds stress tensor profiles in geophysical surface flows, *Geophys. Res. Lett.*, 38(6), doi:10.1029/2011GL046684.

6.1 Introduction

Turbulence strongly controls the exchange of momentum, heat and suspended or dissolved matter in geophysical surface flows occurring in rivers, estuaries and the coastal ocean. In fluvial systems turbulence generates secondary currents both in straight channels (e.g. Colombini, 1993; Blanckaert et al., 2010) and curved channels (e.g. Blanckaert & de Vriend, 2005), and controls shear layers at river confluences (Rhoads & Sukhodolov, 2004), at the interface between a floodplain and a main channel (Tominaga & Nezu, 1991), and within floodplains that feature roughness heterogeneity (Vermaas et al., 2011). Field studies of river turbulence generally focus on small streams (Sukhodolov et al., 1998) where measurements at a high temporal and spatial resolution can be attained with a single point flow meter deployed at various positions in a frame. In estuaries and in the coastal ocean, turbulent fluxes are typically measured from a ship or from a bottom mounted rig (Smith et al., 2005; Mohrholz et al., 2008; Lueck et al., 2002). Especially in studies in larger scale systems, acoustic Doppler current profilers (ADCPs) offer a promising alternative to measure turbulent quantities (Stacey et al., 1999a; Wiles et al., 2006).

The most commonly used method to estimate Reynolds stresses with ADCPs is the so-called variance method (Lohrmann et al., 1990; Stacey et al., 1999a,b; Lu & Lueck, 1999a,b; Rippeth et al., 2002; Souza et al., 2004; Williams & Simpson, 2004; Peters & Johns, 2006; Whipple et al., 2006). Because of the spread between the acoustic beams of the ADCP, instantaneous estimates of velocity components from different beams cannot be combined directly. The spatial spreading can span several times the scale of turbulent motions. To overcome this problem, velocity fluctuations measured in each of the beams are often assumed to have the same statistical properties during the averaging period. The variances in velocity components, needed to estimate Reynolds stresses, are first determined in along-beam coordinates. Then these variances are combined to obtain estimates of Reynolds stress, turbulent kinetic energy (TKE), and other relevant properties of turbulence. However, a perfect alignment is necessary to avoid bias in the shear stresses and estimates of TKE rely on assumptions regarding the anisotropy ratio of normal Reynolds stresses.

Many authors (e.g. Stacey et al., 1999a,b; Lu & Lueck, 1999a,b; Pe-

ters & Johns, 2006) make assumptions about turbulence anisotropy ratios often based on work supported by laboratory and field evidence from relatively small systems, which is reviewed in the benchmark book by Nezu & Nakagawa (1993). Burchard et al. (2008) argues that this approach is not particularly satisfying, since the difference in the main anisotropy ratio between fully anisotropic and fully isotropic turbulence results in a six-fold difference in the value of TKE for an ADCP with a beam separation of 20° (Lohrmann et al., 1990). With a single ADCP such an assumption is needed since it is impossible to solve for the six independent terms in the Reynolds Stress tensor with only four acoustic beams.

In the present paper we introduce a new method which allows to estimate all the terms in the Reynolds stress tensor using two coupled ADCPs (operating in master-slave configuration such that they measure alternately). With eight beams, assumptions on anisotropy ratios become superfluous, and the resulting tensor can easily be rotated in space, increasing the flexibility during data collection. In Section 6.2 the extended variance method for two coupled ADCPs is explained and some considerations are made regarding the measuring setup. Errors are quantified in Section 6.3. Section 6.4 presents data collection and processing techniques. The results are described in Section 6.5, followed by conclusions in Section 6.6.

6.2 Variance method with two ADCPs

We consider a Cartesian coordinate system with its origin at the center of the four transducers of one of the ADCPs (the “master”). The z axis points upward, along the axis of the ADCP; the x axis points from transducer two to transducer one and the y axis from transducer four to transducer three (see Figure 6.1). The orientation of the second ADCP (the “slave”) is defined by three angles ϕ_3 , ϕ_1 and ϕ_2 , which describe the body rotation in right-handed direction around the z axis, around the x axis and around the y axis respectively (see Figure 6.1). The velocity measured along each beam of the ADCPs relates to the velocity vector in Cartesian components as

$$\vec{b} = \mathbf{T}\vec{u} \tag{6.1}$$

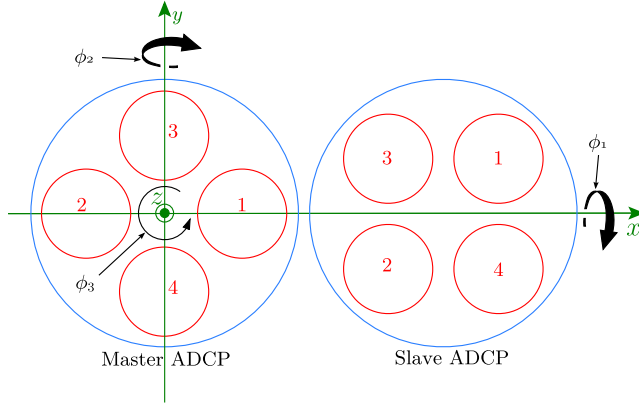


FIGURE 6.1. Definition of the Cartesian, right handed coordinate system with respect to the master ADCP and definition of the angles of rotation. In this case the slave ADCP is rotated 45° around the z axis ($\phi_3 = 45^\circ$). The z axis is pointing out of the paper. All the rotations are defined in right handed sense.

where \vec{b} is an eight-component vector with all the radial velocity components from the two coupled ADCPs, first the master and then the slave, with positive values towards the transducers, \vec{u} is the velocity vector in the Cartesian coordinate system and \mathbf{T} is a rotation matrix \mathbf{T} given by (sin and cos are replaced by s and c for brevity):

$$\mathbf{T} = \begin{pmatrix} \dots & & \\ -s\beta & 0 & -c\beta \\ s\beta & 0 & -c\beta \\ 0 & -s\beta & -c\beta \\ 0 & s\beta & -c\beta \end{pmatrix} \begin{pmatrix} c\phi_2 & 0 & -s\phi_2 \\ 0 & 1 & 0 \\ s\phi_2 & 0 & c\phi_2 \end{pmatrix} \begin{pmatrix} 1 & 0 & 0 \\ 0 & c\phi_1 & s\phi_1 \\ 0 & -s\phi_1 & c\phi_1 \end{pmatrix} \\ + \begin{pmatrix} c\phi_3 & s\phi_3 & 0 \\ -s\phi_3 & c\phi_3 & 0 \\ 0 & 0 & 1 \end{pmatrix} + \begin{pmatrix} -s\beta & 0 & -c\beta \\ s\beta & 0 & -c\beta \\ 0 & -s\beta & -c\beta \\ 0 & s\beta & -c\beta \\ \dots & & \end{pmatrix} \quad (6.2)$$

Here β is the angle between the axis of the acoustic beam and the axis of the instrument. The first right-hand-side term accounts for the transformation from radial components to Cartesian components of

velocity for the master ADCP. The second term on the right-hand-side accounts for transformation from radial to Cartesian components for the slave ADCP, and for the rotation to match with the Cartesian coordinate system of the master ADCP. The exact order of rotation is dictated by the specifications of the ADCP on how it measures tilts (Teledyne RD Instruments, 2010). Mean flow velocity in the Cartesian system is obtained by inverting Equation 6.1. The definition of the transformation matrix \mathbf{T} is instrument dependent and can be modified depending on the instrument specifications (e.g. number of available beams, beam angle) and the relative orientation of the ADCPs being used. In the description of the method and the error analysis we assume the use of two 4-beam ADCPs in Janus configuration (Teledyne RD Instruments, 2010).

The variance in along-beam components can be derived from Equation 6.1, written in covariance form as:

$$\text{var}(b_i) = \sum_{j=1}^3 \sum_{k=1}^3 T_{i,j} T_{i,k} \text{cov}(u_j, u_k) \quad (i = 1 \dots 8) \quad (6.3)$$

or in matrix form as:

$$\vec{v}_b = \mathbf{V} \vec{r} \quad (6.4)$$

where \vec{v}_b is a vector with the variance of the along-beam velocity components, \mathbf{V} is an eight by six matrix resulting from the product of the terms in \mathbf{T} , and \vec{r} is a vector with the six terms of the Reynolds stress tensor, including three normal stresses and three shear stresses. Equation 6.4 is overdetermined and can be solved in a least-squares sense using the generalized inverse of \mathbf{V} :

$$\vec{r} = (\mathbf{V}^T \mathbf{V})^{-1} \mathbf{V}^T \vec{v}_b = \mathbf{V}^+ \vec{v}_b \quad (6.5)$$

Solutions can be optimized by maximizing $\det(\mathbf{V}^T \mathbf{V})$ and become trivial if the latter variable approaches zero. An impression of how this term varies with varying tilt angles for the slave ADCP is given in Figure 6.2 showing that better solutions can be obtained for higher values of ϕ_3 . Although increasing ϕ_3 may improve the solution theoretically, sound reflected from the surface may corrupt the data. These reflections will decrease the range over which the tensor can be solved (see Figure 6.2). The choice for the best setup will mainly

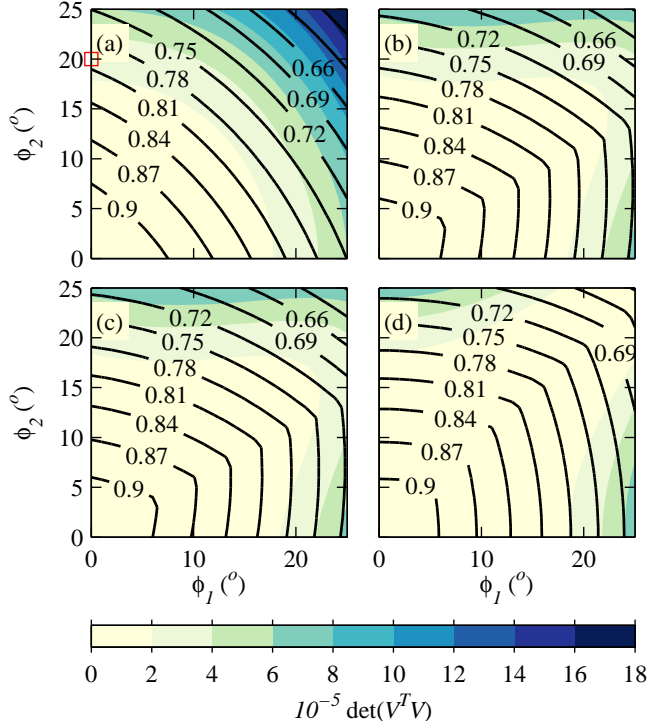


FIGURE 6.2. Colored shades indicate the value of $\det(V^T V)$ for $\phi_3 = 45^\circ$ (panel a), $\phi_3 = 30^\circ$ (panel b), $\phi_3 = 15^\circ$ (panel c) and $\phi_3 = 0^\circ$ (panel d) as a function of ϕ_1 and ϕ_2 . The black contours indicate the fraction of the water column, where a valid estimate of the Reynolds stress tensor can be obtained. This extent is determined by possible surface reflections. The red square in panel a indicates the setup used in this study.

depend on the needs of the user. The six-element vector \vec{r} can be rearranged to form the Reynolds stress tensor according to:

$$\mathbf{R} = \rho \begin{pmatrix} r_1 & r_4 & r_5 \\ r_4 & r_2 & r_6 \\ r_5 & r_6 & r_3 \end{pmatrix} = \rho \begin{pmatrix} \overline{u'^2} & \overline{u'v'} & \overline{u'w'} \\ \overline{u'v'} & \overline{v'^2} & \overline{v'w'} \\ \overline{u'w'} & \overline{v'w'} & \overline{w'^2} \end{pmatrix} \quad (6.6)$$

The overbar indicates averaging over a period spanning several times the largest time scale involved in turbulence. The full Reynolds stress tensor allows rotation in any direction in space. Given a rotation matrix \mathbf{Q}

$$\mathbf{R}' = \mathbf{Q}\mathbf{R}\mathbf{Q}^T \quad (6.7)$$

This relaxes the traditional requirement for the beams of the ADCP to be perfectly vertically aligned. Still, a rigidly mounted setup is preferred in order to avoid eddy-tilt correlations (Lu & Lueck, 1999b).

6.3 Error analysis

The error in estimating the variance of an ensemble of n measurements is given by (Williams & Simpson, 2004):

$$\sigma_{r,i}^2 = \frac{1}{n} \sum_{j=1}^8 (\mathcal{K}_j - 1) \gamma_j V_{i,j}^{+2} (v_{b,j})^2 \quad (i = 1 \dots 6) \quad (6.8)$$

in which γ is a function that accounts for the autocorrelation of \vec{v}_b and \mathcal{K} is the kurtosis of the residuals in unprocessed velocity. The covariance of \vec{v}_b between the beams can be assumed to be negligible compared to the variance of \vec{v}_b . This implies that instantaneous measurements of \vec{v}_b from different beams are assumed independent.

Considering the virtual case with only a contribution of noise in the along-beam velocity variance, Equation 6.8 can be used to study the effect of instrument noise (σ_N) by setting $v_{b,j} = \sigma_N^2$ for all beams. In that case $\gamma = 1$, since the noise has no autocorrelation, and $\mathcal{K} = 3$, assuming Gaussian-distributed noise. Equation 6.8 can be reduced to:

$$r_{i,\min}^2 = \frac{2\sigma_N^4}{n} \sum_{j=1}^8 V_{i,j}^{+2} \quad (i = 1 \dots 6) \quad (6.9)$$

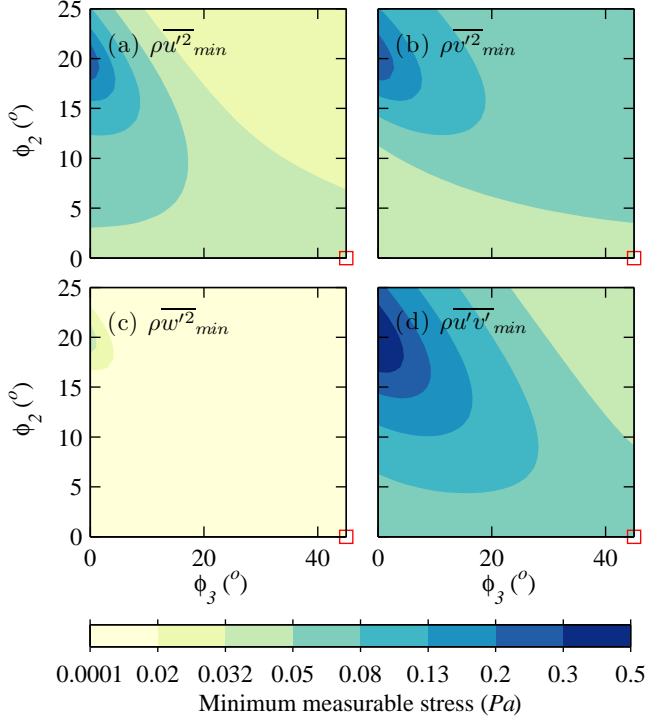


FIGURE 6.3. Minimum stress that can be detected using an averaging interval of 20 minutes for $\overline{\rho u'^2}$ (panel a), $\overline{\rho v'^2}$ (panel b), $\overline{\rho w'^2}$ (panel c) and $\overline{\rho u'v'}$ (panel d), as a function of ϕ_2 and ϕ_3 . ϕ_1 was kept constant to a value of 20° . The red square indicates the setup used in this study. $\overline{\rho u'w'}$ and $\overline{\rho v'w'}$ are not shown here, as they are insensitive to the position of the slave ADCP.

$r_{i,\min}^2$ represents the smallest stress that can be measured with the present technique. Terms containing horizontal components have a much higher detection threshold since the beams are mostly looking upward. The contribution of noise in each of the terms is therefore strongly dependent on the spatial configuration of the two coupled ADCPs. Figure 6.3 shows the change in the minimum detectable stress as a function of tilts. The two stresses $\overline{\rho u'w'}$ and $\overline{\rho v'w'}$, that could already be determined with the classical method, are insensitive to changes in orientation of the slave ADCP. The results of the error

analysis changes if different ADCP systems are used, but the method to assess the errors would remain unchanged.

6.4 Data collection and processing

Two coupled RDI Broadband 1200 KHz ADCPs were placed on a tripod frame, looking upward. The frame was lowered to the bottom of the Mahakam River, East Kalimantan, Indonesia, at the exit of a mild bend (Sassi et al., 2011b). The river width at the measuring location is 420 m. The frame was located 50 m away from the concave bank at a mean depth of 17 m. The flow is influenced by a mixed, mainly semi-diurnal tide, and no salt water intrusion was observed during the measuring period.

Data were collected over a 25 hour period, using a setup which prevents interference between the two instruments. A full measuring cycle, with the present setup, lasts 1.52 s. During this time both ADCPs collect single-ping data lasting 0.6 s each, composed of 5 sub-pings. Collecting these sub-pings allows to reduce the standard deviation in estimated velocity (Williams & Simpson, 2004; Nidzieko et al., 2006). A special cable connecting the two ADCPs allows them to communicate, ensuring they do not measure simultaneously. The heading difference ϕ_3 between the two instruments was 44.7° , the pitch difference was 20° (ϕ_1) and the roll difference was 0.4° (ϕ_2). In this configuration one beam points vertically upward. Surface reflections limited the valid range to the lowest 80% of the water column (see Figure 6.2). To ensure that the slave ADCP collected data in depth cells of similar vertical size as the master ADCP, the slave measured depth cells of 27 cm and the master cells of 25 cm.

The collected raw velocity in along-beam components was processed using a window spanning 20 minutes. Mean velocity and variance were determined for each of the radial velocity components. All measurements beyond the range at which sound is possibly reflected by the water surface were marked as bad. This range varies for each beam according to its orientation. Subsequently, the velocity from each of the slave beams was remapped to the exact position of the master using a nearest neighbor search. From these data, mean flow components and the Reynolds stress tensor were determined. Terms in the Reynolds stress tensor smaller than the detection limit

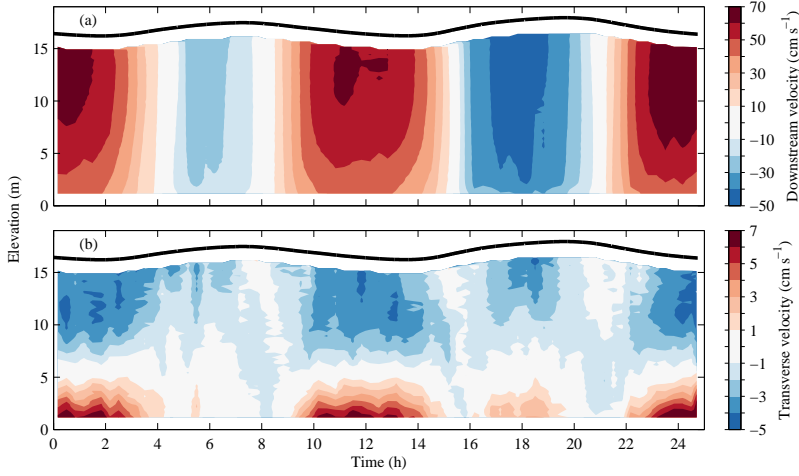


FIGURE 6.4. Mean flow velocity in downstream direction (panel a) and transverse direction (panel b), defined positive away from the concave bank

in Equation 6.9 were marked bad. The resulting tensors were rotated such that the x component matched the downstream direction, defined as the mean ebb-flow direction during ebb and the opposite of the mean flood direction during flood.

6.5 Results

The downstream component of velocity is nearly logarithmic and the highest water level lags about two hours behind flow reversal (see Figure 6.4, panel a). During ebb, the flow slightly decreases near the surface. This is probably due to the influence of the bank, causing momentum dissipation near the surface (Sassi et al., 2011b). The transverse flow (positive away from the concave bank) features a typical curvature-induced secondary flow profile (see Figure 6.4, panel b). The secondary circulation is most pronounced during ebb, due to the stronger downstream flow, but is also present during the second flood period. During the first flood the flow is too weak to develop secondary circulation. The vertical component of velocity, defined positive upward, is on average 0.02 ms^{-1} during ebb and

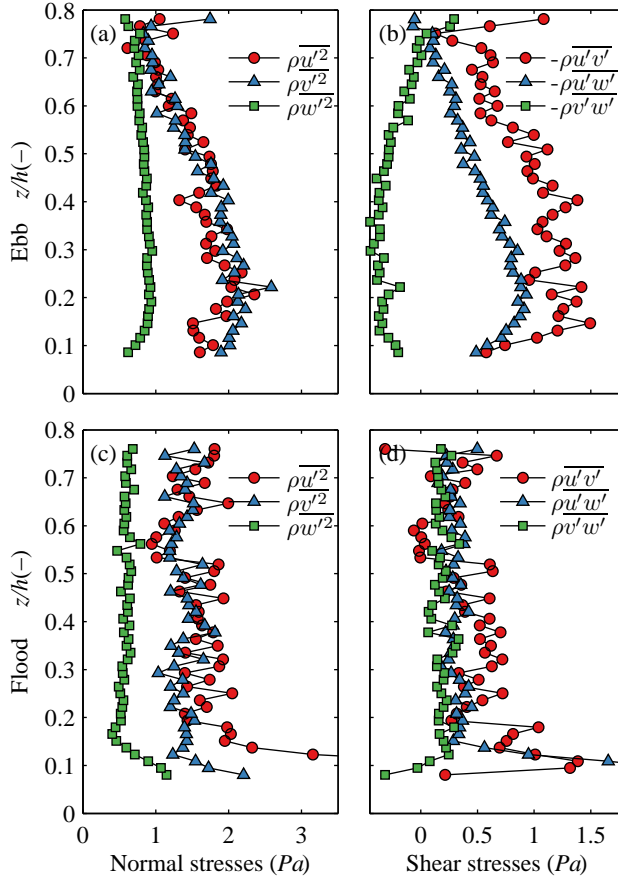


FIGURE 6.5. Profiles of normal and shear stresses during ebb and flood

-0.02 ms^{-1} during flood. This seems to be caused by the river bed which slopes slightly downward in upstream direction.

Normal and shear Reynolds stresses during ebb and during flood are shown in Figure 6.5 as a function of depth. During ebb the principal shear stress ($-\overline{\rho u'w'}$) is lower than the horizontal shear stress ($-\overline{\rho u'v'}$), but higher than the cross-vertical shear stress ($-\overline{\rho v'w'}$). A similar pattern was observed by Jamieson et al. (2010) in a mild bend at about 45° from the bend entrance in a laboratory flume. The pro-

file of principal shear stress during ebb increases linearly down to a relative depth of 0.2, then it decreases again toward the bottom. During flood the profile of principal shear stress is relatively uniform down to a relative depth of 0.15, after which it increases strongly toward the bottom. Both profiles can be ascribed to the upflow during ebb and downflow during flood (Nezu & Nakagawa, 1993). Similar profiles associated with upflow and downflow were observed by Blanckaert et al. (2010). At locations featuring upflow they observed a peak in the profile of principal shear stress at a relative depth up to 0.3.

To describe the anisotropy ratios, often used to determine turbulent kinetic energy (TKE) from the variance method, we determined the parameter $\alpha = \overline{w'^2} / (\overline{u'^2} + \overline{v'^2})$. In the classical method assumptions have to be made on the value of α which may introduce errors in the estimates of TKE or dissipation (Lohrmann et al., 1990). Both during ebb and during flood, α increases with distance from the bed (see Figure 6.6). During flood, values of α are around 0.2, which is similar to values reported by Nezu & Nakagawa (1993); Lu & Lueck (1999b); Stacey et al. (1999b). During ebb, α increases from 0.2 at the bottom to 0.4 near the surface.

6.6 Conclusions

Studies on turbulence in geophysical surface flows benefit from the use of acoustic Doppler current profilers. The variance method is commonly used to derive turbulent properties from ADCP data, which has several limitations when applied with a single ADCP. We extended the variance method to rigid deployments with two coupled ADCPs.

Measurements from a bend in the Mahakam River show that ratios between normal stresses can differ strongly from ratios measured in laboratory experiments (Nezu & Nakagawa, 1993) or small streams (Sukhodolov et al., 1998). This shows that assumptions made in estimating TKE and dissipation in the classical method are not always justifiable. The technique we present herein improves flexibility during data collection. With eight beams and six unknown terms, the Reynolds stress tensor can be completely estimated, without making other assumptions than homogeneity of the turbulence field between

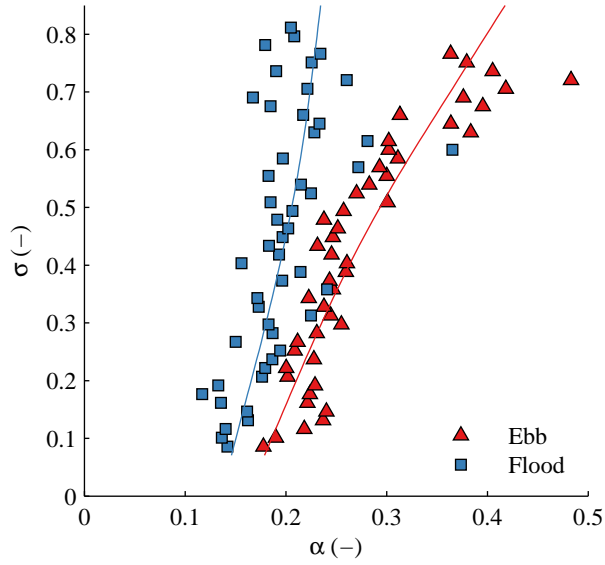


FIGURE 6.6. Profiles of the parameter α during ebb and flood

the beams. Obtaining the complete Reynolds stress tensor allows for rotation, which is needed in field studies where vertical alignment is difficult to achieve.

On the use of horizontal acoustic Doppler profilers for continuous bed shear stress monitoring

Abstract

Continuous monitoring of bed shear stress in large river systems may serve to better estimate alluvial sediment transport to the coastal ocean. Here we explore the possibility of using a horizontally deployed acoustic Doppler current profiler (ADCP) to monitor bed shear stress, applying a prescribed boundary layer model, previously used for discharge estimation. The model parameters include the local roughness length and a dip correction factor to account for sidewall effects. Both these parameters

This chapter is based on: VERMEULEN, B., A. HOITINK, AND M. SASSI, 2013, On the use of horizontal acoustic doppler profilers for continuous bed shear stress monitoring, *International Journal of Sediment Research*, 28(2), 260–268, doi:10.1016/S1001-6279(13)60037-2.

depend on river stage and on the position in the cross-section, and were estimated from shipborne ADCP data. We applied the calibrated boundary layer model to obtain bed shear stress estimates over the measuring range of the HADCP. To validate the results, co-located coupled ADCPs were used to infer bed shear stress, both from Reynolds stress profiles and from mean velocity profiles. From HADCP data collected over a period of 1.5 years, a time series of width profiles of bed shear stress was obtained for a tidal reach of the Mahakam River, East Kalimantan, Indonesia. A smaller dataset covering 25 hours was used for comparison with results from the coupled ADCPs. The bed shear stress estimates derived from Reynolds stress profiles appeared to be strongly affected by local effects causing upflow and downflow, which are not included in the boundary layer model used to derive bed shear stress with the horizontal ADCP. Bed shear stresses from the coupled ADCP are representative of a much more localized flow, while those derived with the horizontal ADCP resemble the net effect of the flow over larger scales. Bed shear stresses obtained from mean velocity profiles from the coupled ADCPs show a good agreement between the two methods, and highlight the robustness of the method to uncertainty in the estimates of the roughness length.

7.1 Introduction

Bed shear stress in natural environments cannot be measured directly and therefore it has to be estimated from other variables such as flow velocity or turbulent stresses. The need for estimates of bed shear stress is motivated by its importance to describe and model sediment transport and morphology (Wilcock, 1996) and to characterize rivers through the tightly related concept of stream power (Chang & Hill, 1977; Akhtar et al., 2011). Several methods are available to obtain estimates of bed shear stress (Biron et al., 2004): fitting a profile function to velocity measurements, extrapolating profiles of Reynolds-stress to the bottom, assuming a constant ratio between turbulent kinetic energy and bed shear stress or using spectral characteristics of the flow (Kim et al., 2000). All these methods provide bed shear stress estimates for a limited period, and are unsuitable to monitor bed shear stress continuously. Acoustic Doppler current profilers (ADCPs) can measure over longer periods and have the po-

tential to measure bed shear stress.

Two recent developments related to acoustic Doppler profilers offer a great potential for bed shear stress monitoring: (1) discharge measurements from horizontally deployed ADCPs (HADCPs) and (2) Reynolds stress estimation based on bed-mounted coupled ADCPs (CADCPs). HADCPs are generally mounted near a riverbank or on a bridge pier and look horizontally into the cross-section. They measure a velocity profile over the range of the instrument. CADCPs adopt a measuring setup that uses two coupled ADCPs mounted on the riverbed to measure profiles of the Reynolds stress tensor over depth.

During the years 2008 and 2009, we performed measurements with an HADCP, and for a smaller period of 25 hours we performed co-located measurements with an HADCP and CADCPs in a tidal river bend in the Mahakam River, East Kalimantan, Indonesia. We previously used these data to estimate discharge in a tidal river (Sassi et al., 2011b) and profiles of the Reynolds stress tensor expanding the variance method for ADCPs (Chapter 6). In the present contribution, we elaborate on existing theory to estimate bed shear stress from HADCPs and CADCPs, which we introduce in Section 7.2 and Section 7.3, respectively. In Section 7.4, we describe the data collection. We present and discuss results in Section 7.5 followed by conclusions in Section 7.6.

7.2 Bed shear stress from HADCPs

Recent contributions (Nihei & Kimizu, 2008; Le Coz et al., 2008; Hoitink et al., 2009; Sassi et al., 2011b; Hidayat et al., 2011) have laid out a new technique to monitor discharge using HADCPs. The approach by Hoitink et al. (2009), improved by Sassi et al. (2011b), is composed of a deterministic part in which a well-calibrated boundary layer model is used to translate velocity at a single depth into a depth mean velocity. In a similar fashion, the boundary layer model is suitable to obtain bed shear stresses from a single depth velocity. We will briefly review the boundary layer model and its calibration following the approach of Sassi et al. (2011b). From this, we readily obtain bed shear stress. Flow affected by sidewalls usually features a deflection in the velocity profile near the surface, often referred

to as a velocity-dip. Considering a steady, uniform and fully developed turbulent flow a velocity profile function can be derived that accounts for this sidewall effect. The velocity profile reads (Yang & McCorquodale, 2004):

$$u(z) = \frac{u_*}{\kappa} \ln \left(\frac{z}{z_0} \right) + \frac{u_*}{\kappa} \alpha \ln \left(1 - \frac{z}{H} \right) \quad (7.1)$$

where u is the longitudinal velocity, z is the vertical coordinate, u_* is the shear velocity, κ is the von Karman constant, z_0 is the roughness length, H the water depth and α is a parameter that accounts for the side-wall effect. α relates to the location of maximum velocity in the vertical z_{\max} as:

$$\frac{z_{\max}}{H} = \frac{1}{1 + \alpha} \quad (7.2)$$

The adopted boundary layer model implies a Reynolds-stress profile that reads:

$$\frac{\overline{u'w'}}{u_*^2} = 1 - (1 + \alpha) \frac{z}{H} \quad (7.3)$$

Sidewall effects thus tend to steepen the vertical profile of Reynolds-stress. To calculate a depth-averaged velocity, starting from a single depth velocity measurement from the HADCP, Sassi et al. (2011b) calibrated α and z_0 using ship-borne velocity data collected during several flow conditions. This resulted in width profiles of α and z_0 where the latter is also dependent on tidally averaged river level (Sassi et al., 2011b). Based on these parameters we can estimate bed shear stress as:

$$\tau = \rho \left(\frac{\kappa u}{\ln(\sigma_c H) + \alpha \ln(1 - \sigma_c) - \ln(z_0)} \right)^2 \quad (7.4)$$

7.3 Bed shear stress from coupled ADCPs

To derive bed shear stress from CADCPS, we obtained profiles of the Reynolds stress tensor following the approach in Chapter 6, using two coupled ADCPs measuring asynchronously. We will shortly review the main points of this method and explain how we obtained bed shear stresses. This method is based on the variance method (Lohrmann et al., 1990; Stacey et al., 1999a,b; Lu & Lueck, 1999a,b; Peters & Johns, 2006), which we extended for configurations with

more than four beams. The benefit of the second ADCP is that it allows estimating all six terms in the Reynolds stress tensor. We consider a Cartesian coordinate system with its origin at the center of the four transducers of one of the ADCPs (the “master”). The z-axis points upward, along the central axis of the ADCP. The x-axis points from transducer two to transducer one and the y-axis from transducer four to transducer three (see Figure 6.1). We derived Reynolds-stresses relative to this coordinate system. The tensor can be easily rotated to any other Cartesian coordinate system. The position of the second ADCP (the “slave”) is defined with respect to the master ADCP-centered coordinate system by three angles ϕ_3 , ϕ_1 and ϕ_2 , which describe the right-handed rotation of the slave ADCP around the z-axis, around the x-axis and around the y-axis, respectively. All of the velocity components measured by the two ADCPs can be expressed as a function of the Cartesian velocity components as:

$$\vec{b} = \mathbf{T}\vec{u} \quad (7.5)$$

where \vec{b} is an eight-component vector with all the radial velocity components from the two coupled ADCPs. \mathbf{T} is a transformation matrix and \vec{u} is the velocity vector in the Cartesian coordinate system. The mean flow velocity in the Cartesian system is obtained by inverting Equation 7.5. Since we cannot determine and combine instantaneous fluctuations of velocity obtained from Equation 7.5 for turbulence calculations we will first determine the variance in the beam velocity as a function of the variance and covariance in the Cartesian components of velocity (i.e. the Reynolds stresses). Calculating the variance of the beam components of velocity from Equation 7.5, we obtain:

$$\text{var}(b_i) = \sum_{j=1}^3 \sum_{k=1}^3 T_{i,j} T_{i,k} \text{cov}(u_j, u_k) \quad (i = 1 \dots 8) \quad (7.6)$$

or in matrix form as:

$$\vec{v_b} = \mathbf{V}\vec{r} \quad (7.7)$$

where $\vec{v_b}$ is a vector containing the variance of the along-beam velocity components, \mathbf{V} is an eight by six matrix resulting from the product of the terms in \mathbf{T} , and \vec{r} is a vector with the six terms of

the Reynolds stress tensor including three normal stresses and three shear stresses. Equation 7.7 is solved in a least-squares sense using the generalized inverse of \mathbf{V} :

$$\vec{r} = (\mathbf{V}^T \mathbf{V}) \mathbf{V}^T \vec{v}_b = \mathbf{V}^+ \vec{v}_b \quad (7.8)$$

The six-element vector \vec{r} can be rearranged to form the Reynolds stress tensor.

To calculate bed shear stress, we fitted a linear model to the profiles of Reynolds-stresses starting from the three lowermost measurements and consecutively adding data points until the optimal goodness of fit is reached. We defined the goodness of fit as:

$$\chi = \frac{1}{\text{df}} \frac{\sum \left(\overline{u'w'}_o - \overline{u'w'}_f \right)^2}{\text{var} \left(\overline{u'w'}_o \right)} \quad (7.9)$$

where χ is the goodness of fit, df is the number of degrees of freedom, $\overline{u'w'}_o$ is the observed Reynolds stress and $\overline{u'w'}_f$ is the fitted Reynolds stress. On average, we fitted six points from the bed to obtain bed shear stress. The largest number of points was fitted during flood, which indicates that near-bed profiles of main shear stress best resemble a linear profile during flood. To determine bed-shear stresses based on the velocity profiles from the coupled ADCPs we fitted the same boundary layer model presented in Section 7.2. We fitted α , z_0 and u_* freely using a linear regression. Afterwards, we determined the median values for α and z_0 during ebb and flood and re-performed the fitting of u_* , keeping the values of α and z_0 fixed. This was done to avoid unrealistic values of these parameters around slack water. Sensitivity of estimates was determined by performing the same fit using the 25% and 75% quantile values of $\ln(z_0)$.

7.4 Data collection and processing

Horizontal ADCP

A Horizontal 600 kHz ADCP was placed on a solid jetty near the bank of a 420 m wide section of the Mahakam River (Figure 7.1). In this relatively straight section, located between two mild bends, the flow

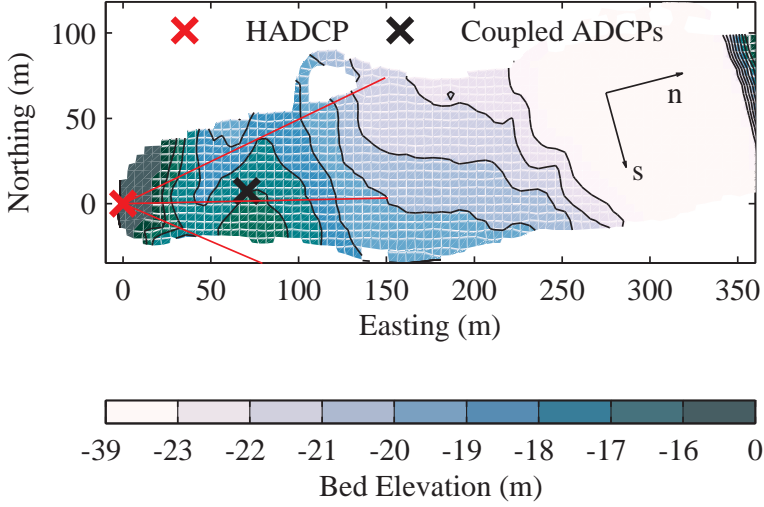


FIGURE 7.1. Bed elevation and location of coupled ADCPs (black square) and the HADCP (red square). Ebb flow is in southward direction. The CADCPs are located on top of a bedform.

is influenced by a mixed, mainly semi-diurnal tide. No salt-water intrusion was observed during the measuring period. We collected two datasets: (1) a long-term dataset covering 1.5 years of flow profiles averaged over 10 minutes and sampled every 30 minutes, and (2) a short dataset covering 25 hours at a frequency of 1 Hz. These data were collected simultaneously with measurements from the CADCP, which was placed within the range of the HADCP.

The Horizontal ADCP was mounted 5 m above the bed and its measuring range covered around one third of the local channel width. Data were collected in depth cells of 1 m. Pitch, roll and heading remained constant during the measuring period with a value of 0.0° , -0.5° and 88.7° respectively. Along (*s*) and across (*n*) coordinate at this section were determined based on the bathymetry following (Hoitink et al., 2009). The coordinate is defined as the directions in which variations in bathymetry are minimal. Sassi et al. (2011b) found that this minimum value corresponds to an orientation of 165° from the

north. Velocity in s and n direction were determined by transforming the along beam velocity of beam one and three.

To calibrate α and z_0 in Equation 7.4, vessel mounted velocity data were used. Bedload sediment transport under high flow conditions can bias the estimated ship velocity from an ADCP feature called bottom-tracking. To overcome this issue, velocity data was corrected for ship movements using bottom-tracking velocity for low flow conditions and GPS-based ship velocity during high flow conditions, when significant bedload transport occurs. Velocity was interpolated to a vertical grid in the normalized coordinates $\sigma = z/H$ and $\beta = n/W$. F was determined as the ratio between the HADCP velocity and the depth-averaged velocity found from the transect data. α was determined from the point of maximum velocity in depth and z_0 was obtained by fitting Equation 7.1 to the vertical profiles of velocity. Further details of the calibration procedure can be found in Sassi et al. (2011b)

Coupled ADCPs

The two coupled ADCPs were connected using a cable that allows them to communicate, ensuring they do not collect data simultaneously. The master first sends a synchronization pulse to the slave and waits long enough for the slave to take a profile measurement. The slave receives the synchronization pulse and collects one profile of velocity. Then the master measures a velocity profile and sends again a synchronization pulse to the slave. The whole cycle lasts 1.52 s. Each profile recorded by the ADCPs is an average of five profiles (taken from sub-pings). This averaging over sub-pings reduces the standard deviation in the measured velocity. The profiles were collected in cells of 25 cm for the master and 27 cm for the slave, to obtain vertical cells of a similar size, once the slave ADCP was tilted. The heading difference (ϕ_3) was 44.7° , the pitch difference (ϕ_1) was 20° and the roll difference (ϕ_2) was 0.4° . This setup ensures that one beam of the slave ADCP measures vertically upward.

The collected velocity data were processed to remove all cells that could possibly be influenced by surface reflections. For the beam with the highest tilting angle the upper 20% of the data had to be removed. The remaining raw radial velocity was filtered using a first-order Loess filter (Cleveland, 1979) with a span of two hours,

to separate the mean flow from turbulence and noise. The resulting mean velocity and velocity variance from the slave were remapped to match the vertical position of the depth cells of the master using a nearest neighbor search. The noise level was determined from the lowest measured variance in the velocity and used to correct the bias in the normal stresses (Stacey et al., 1999a). The obtained variance in toward beam velocity is filtered in space using a first-order Loess filter with a span of five depth cells. Variance and mean velocity are then transformed to a Cartesian coordinate system aligned with the master ADCP, yielding the Reynolds stresses. Any Reynolds stress below the detection threshold was filtered out. The Mean flow vector and the Reynolds stress tensor are rotated to align the x-component in the downstream direction. The downstream direction is defined as the mean ebb-flow direction during ebb and the opposite of the mean flood-flow direction during flood.

7.5 Results and discussion

The temporal variation of bed shear stresses obtained from the HADCP (Figure 7.2) closely follows the mean flow pattern. Subtidal variations in bed shear stress show higher stresses during neap tide than during spring tide, which may be associated to the occurrence of fortnightly tides such as MSf (Buschman et al., 2009). Long-term variations in bed shear stress are the consequence of river floods that increase flow velocity and therefore bed shear stress. The width profiles of bed shear stress in the range of the HADCP mainly reflect the effect of the decreasing velocity toward the banks.

For the 25 hour dataset the velocity profiles in Figure 7.3 are rotated such that the downstream velocity matches with the depth-mean velocity vector during ebb and with the opposite of the depth mean velocity vector during flood. As observed by Sassi et al. (2011b) velocity profiles in the bend at Samarinda feature a velocity dip profile that can be attributed to side-wall effects (see Figure 7.3a). This is best visible when the velocity magnitude is highest. The transverse velocity features typical profiles of secondary flow (see Figure 7.3b). Secondary flow is most pronounced during the ebb. During the first flood period, the flow is not strong enough to develop a significant secondary flow, while during the second flood the secondary flow

7. BED SHEAR STRESS MONITORING WITH AN HADCP

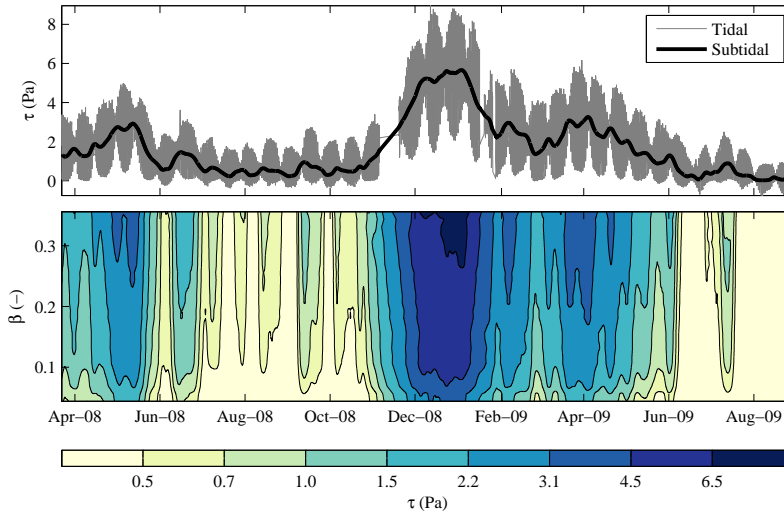


FIGURE 7.2. Bed shear stress estimated from the HADCP measurements. The upper panel shows the tidal (thin gray line) and subtidal (solid black line) variation of the profile averaged bed shear stress. The lower panel shows the subtidal variation of bed shear stress over the range across the tidal river covered by the HADCP.

clearly develops. Mostly during ebb, but also during flood, upward velocity is observed near the bed. This probably occurs due to the bed form (Figure 7.1), which influences the local flow.

During the development of secondary flow during ebb, the profiles of principal shear stress (see Figure 7.4e) slowly develop from a concave to a convex profile. The location of maximum shear stress moves from near the bed, in the beginning of the ebb, toward a relative depth of 0.35 during peak flow and back to the bed at the end of the flood. This pattern matches with the slight upflow that causes velocity gradients to be smaller near the bed, decreasing Reynolds stresses near the bed. Blanckaert et al. (2010) observed similar profiles in a laboratory flume. During flood, the principal shear stress always reaches its maximum value near the bed, but this maximum strongly increases at the peak of the flood, rendering the profile increasingly concave. The increase in shear stress near the bed matches

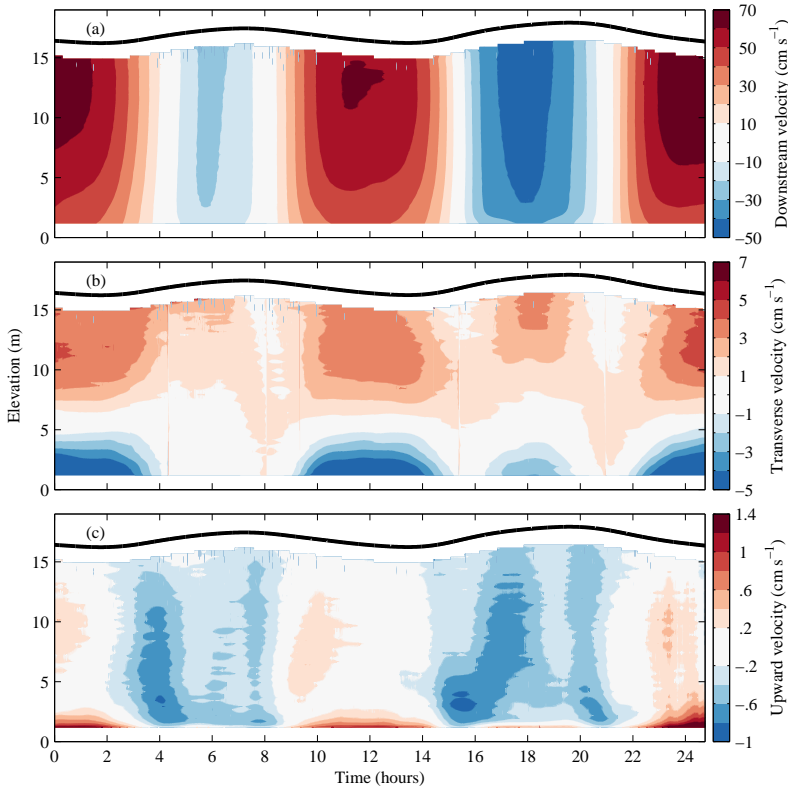


FIGURE 7.3. Downstream (a), transverse (b) and upward (c) components of mean velocity obtained from the ADCPs.

with profiles of downstream velocity (Figure 7.5). These profiles are almost bilinear with a strong increase in vertical shear towards the bed. This increase in velocity gradient near the bed may be related to the subtle down-flow that causes compression of the isovels near the bed. Normal stresses are highest during flood, just below mid-depth. Remarkable is the strong increase in normal stresses and turbulent kinetic energy near the bed during flood.

Bed shear stress was estimated for the 25-hour measuring period using the horizontal ADCP based technique, using the profiles of Reynolds-stress from the coupled ADCPs and with the mean ve-

7. BED SHEAR STRESS MONITORING WITH AN HADCP

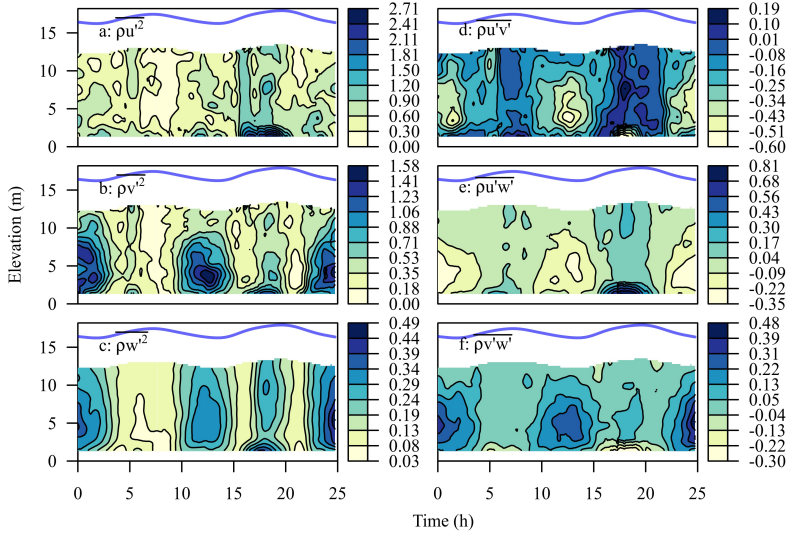


FIGURE 7.4. Profiles of $\overline{\rho u'^2}$ (a), $\overline{\rho v'^2}$ (b), $\overline{\rho w'^2}$ (c), $\overline{\rho u'v'}$ (d), $\overline{\rho u'w'}$ (e), $\overline{\rho v'w'}$ (f) obtained from the CADCPs. Color map labels are in units of Pa.

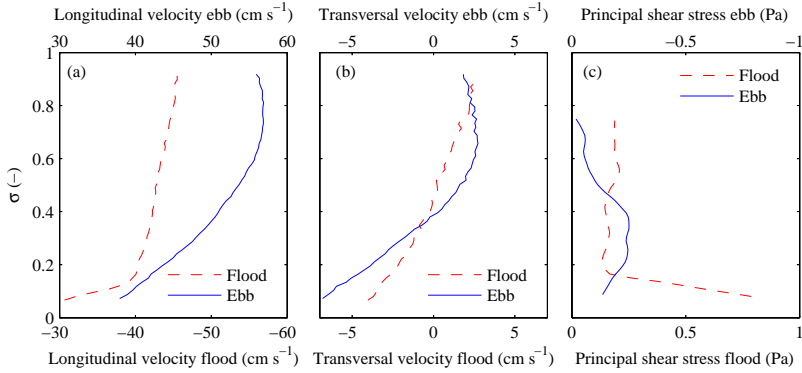


FIGURE 7.5. Detail of a typical profile of CADCPs derived downstream velocity (a), transverse velocity (b) and principal shear stress ($-\rho \overline{u'v'}$) (c) during the second ebb (solid, blue line) and second flood phase (dashed, red line).

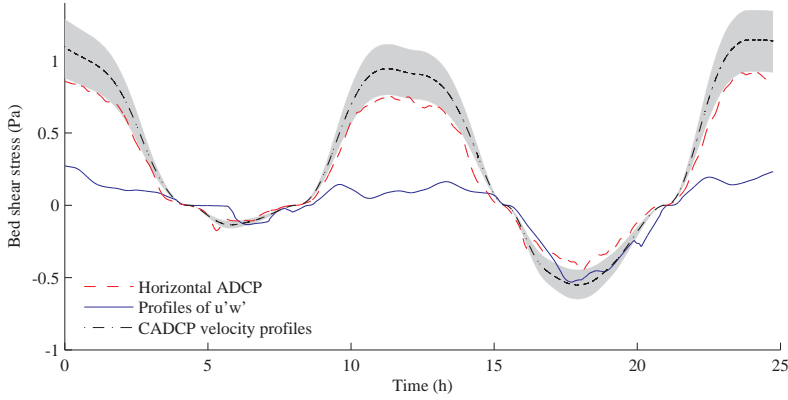


FIGURE 7.6. Bed shear stress estimated based on HADCP velocity data (red, dashed line), with profiles of vertical shear stress (blue, solid line) from the CADCP and from vertical velocity profiles from the CADCP (black, dash-dotted). The gray shaded area indicates the range of shear stresses for z_0 varying in the interquartile range.

locity profiles from the coupled ADCPs. Bed shear stress based on the Reynolds stress profiles from the coupled ADCP show an increase during ebb up to the point where upflow develops (Figure 7.6). The change of the Reynolds-stress profile from concave to convex during the development of the secondary currents is reflected in the bed shear stress, which increases up to a certain threshold after which it remains constant. A completely different trend is observed during flood. Bed shear stress does not reach a threshold since no upflow is present.

The estimates of bed shear stress based on the velocity profiles from the coupled ADCPs agree reasonably well with the values obtained from the HADCP. The slight discrepancy between the two is attributed to slightly different values for z_0 used in the estimates. The sensitivity of the estimates of bed shear stress to the estimated values of z_0 is determined by re-computing the bed-shear stress using the 25% and 75% quantile values for $\ln z_0$, which were determined from the velocity profile fits. The estimates are found to be rather insensitive to the estimated z_0 . The discrepancy between the bed shear

stress estimates from velocity profiles and from Reynolds stress profiles is attributed to the fact that estimates based on velocity profiles are representative for much larger scales than the ones obtained from Reynolds stress profiles.

7.6 Conclusions

Two recently developed methodologies have been expanded making them suitable to monitor bed shear stress. HADCPs can yield continuous estimates of profiles of bed shear stress over the width of a channel while ADCPs estimate bed shear stress at a single point. The two techniques were applied to a tidal bend in the Mahakam River where co-located measurements were obtained. Good agreement is found between the HADCP based bed shear stresses and those estimated from the velocity profiles of the coupled ADCPs. Larger differences are found with the Reynolds stress profile based estimates. This discrepancy is mainly attributed to the different methodologies used. The Reynolds stress-based bed shear stresses represent localized flow conditions, while the velocity profile-based estimates are expected to be representative for a much larger area with an approximate size of the adaptation length of the streamwise velocity.

The results presented here show horizontal ADCPs may be useful instruments to continuously monitor bed shear stresses over the width covered by the acoustic signal. The method is shown to be relatively insensitive to changes in roughness length. Bed shear stress inferred from vertical velocity profiles represent a much larger area than local bed shear stress estimates from extrapolated Reynolds stress profiles, which explains the substantial differences between the alternative approaches.

Synthesis

In this thesis new methods and concepts have been introduced that elucidate processes governing complex river flow and morphology .

8.1 Main findings

Non-harmonic meanders occurring along the Mahakam River ([Chapter 2](#)) are strongly related to scouring of the river bed near the meander apex, resulting in an exceptional increase in cross-sectional area ([Chapter 3](#)). The large cross-sectional area strongly affects the flow pattern inducing horizontal recirculation and strong vertical flows ([Chapter 5](#)). These features occur in a region with no consolidated outcrops, but where soil forming processes consolidate the banks with Iron and Manganese concretions. All of these results are indicative of a morphological regime in which the river, through the development of a complex three-dimensional flow, excavates deep scours. This excavating regime contrasts with a classic meandering regime in which pools and point bars develop.

The Mahakam River is not the only river in which this regime was observed. This regime was also observed along the middle Fly river, featuring dog-leg shaped meanders with limited planimetric development ([Dietrich et al., 1999](#)), deep scours ([Aalto et al., 2010](#)),

and iron concretions that consolidate the banks (Dietrich et al., 1999). The excavating regime does not seem to be a tropical lowland river prerogative. Similar regimes have also been found in small streams in temperate regions (Andrle, 1994; Nanson, 2010; Blanckaert, 2011) and in a large river in the Arctic (Beltaos et al., 2012). Common elements in all of these systems are low bed-slopes, high loads of suspended sediments, and high resistance to erosion of the substrate. These environmental factors may therefore be the key ingredients leading to a different functioning of meander bends.

New measuring and analysis techniques developed throughout this thesis provide valuable tools to increase our understanding of the excavating regime and many other poorly understood fluvial phenomena. A new wavelet-based method to quantify meander shape (Chapter 2) is expected to provide the means to discriminate between different meandering regimes solely based on channel planform, allowing to identify non-harmonic meanders. Principal component analysis of PALSAR images can detect the meander belt of a river (Chapter 3), showing the area in which the river has been freely migrating. An improved method to monitor mean flow (Chapter 4) and a method to profile Reynolds stresses (Chapter 6) in large fluvial systems are expected to offer new field-based insights into the flow and environmental conditions that shape deep scours, beyond the case of strongly curved flows.

Profiles of Reynolds stresses, measured with two coupled ADCPs (Chapter 6), show that commonly used assumptions on turbulence anisotropy, based on laboratory experiments, can fail under field conditions. Also, vertical profiles of the principal Reynolds shear stress (Chapter 7), often used to infer bed shear stress, can differ from the expected behavior. Natural scouring in rivers can lead to flow patterns which are affected by a non-hydrostatic pressure distribution (Chapter 5). These results question common practices in hydrodynamic modeling and data interpretation, and stress the need for caution when applying laboratory-based insights to the field. Computational models can be improved based on new insights that can be obtained from the newly introduced measuring techniques, which have the potential to bridge the gap between detailed results from controlled laboratory conditions and coarse observations obtained under natural field conditions.

8.2 Future research directions

Genesis of deeply scoured bends

The ubiquity of sharp bends and associated scour holes calls for an explanation on how and under which circumstances such bends develop. The proposed method to quantify meander shape ([Chapter 2](#)) can be used to analyze a large number of river planforms easily obtained from satellite images, to relate shape properties to specific environmental factors such as stream-power, soil erodibility or to the climate. Monitoring the flow through bends at different stages in the transition from a mild bend regime to the deeply scoured sharp bend regime, can provide information on why bends develop these complex three-dimensional flow patterns. This could also be achieved by simulating a set of river bends with varying curvature with a Large Eddy Simulation ([Labeur & Wells, 2012](#)).

Field validation of turbulence closure schemes in gradually varied flow

The application of turbulence closure schemes, predominantly validated in laboratory conditions and small scale streams, to models in large rivers still needs proper validation data. The method introduced in [Chapter 6](#) is able to profile the Reynolds stress tensor and can provide the data necessary for turbulence closure validation in large rivers. The data can also be used to validate the effect of secondary flow on Reynolds stresses and the generation of secondary cells by turbulence.

Turbulence scaling in the field

Sharp bends and deep scours occur in small streams as well as in large rivers ([Chapter 3](#)). This suggests that this phenomenon is scale independent. Mean downstream flow is known to scale independently of the Reynolds number, within the turbulent range, but for lateral flow and turbulent exchange this is not the case ([Wei & Willmarth, 1989](#)). The possibility to study turbulence properties in large rivers allows to investigate the scale-dependence of turbulence occurring in scour flow and how this affects the development of scours. Laboratory experiments on small scale scour can complement field

based measurements, to test the scale-dependency over several orders of magnitude.

8.3 Implications for water management

Scour holes

Scours induced by natural processes are known to develop at confluences, bends, channel constrictions or due to a change in the general hydraulic regime of a system (Hoffmans & Verheij, 1997). They also develop near constructions such as culverts, spillways and bridge piers, which cause a plunging or horizontal jet to develop which will lead to increased shear stress, and eventually to the development of the scour (Hoffmans, 1998). Examples of such scours are those observed near the Eastern Scheldt storm-surge barrier. Prediction of the initiation and development of these scours is essential to develop plans to properly manage the storm-surge barrier (van Noortwijk & Klatter, 1999). The prediction of scours, however, is still difficult. In particular, the behavior of the upstream slope of scours remains poorly understood (Pilarczyk, 2011). The newly developed methods (Chapter 6 and Chapter 4) are expected to provide new means to further improve our models, adding to the ability to predict the scour process.

Stream restoration

Stream restoration often involves several rehabilitation phases, including the recreation of a sinuous channel. In this phase it is necessary to rely on old maps, or on existing knowledge on meander planforms. Poorly designed meander planforms can lead to undesirable morphological behavior, such as erosion and deposition, bank destabilization, etc. The methods developed in Chapter 2 can contribute to describe the shape of meanders with a few parameters, which can be used to reconstruct a meander planform for stream restoration. It can also serve as a means to identify certain meander behavior in relation to environmental factors such as soil type, channel slope, stream power, etc.

Reduced order models

Operational models used for flood predictions or morphological response, are usually reduced-order models. These models use parameterizations for processes occurring at the sub-grid scale or in a dimension not included in the model. Current models use parameterizations often based on knowledge from laboratory experiments or from temperate region rivers. In [Chapter 3](#) and [Chapter 5](#), we show that large rivers can have bends that function differently than what can be expected based on the existing literature. The flow found in these bends is not captured by reduced order models. Therefore, care should be taken when applying models to large rivers in which such bends occur. Also, the presence of bank embayments can influence the roughness and lateral erosion ([Darby et al., 2010](#)). The complex flow processes described in this thesis require new parameterizations to be included in existing computational models.

Bibliography

- AALTO, R., J. W. LAUER & W. E. DIETRICH (2008). Spatial and temporal dynamics of sediment accumulation and exchange along Strickland River floodplains (Papua New Guinea) over decadal-to-centennial timescales. *J. Geophys. Res.*, 113, F01S04. doi:10.1029/2006JF000627.
- AALTO, R. E., M. GRENFELL & J. W. LAUER (2010). Imaging beneath the skin of large tropical rivers: Clay controls on system morphodynamics revealed by novel CHIRP sub-surface sonar and deep coring along the Fly and Strickland Rivers, Papua New Guinea (Invited). In *AGU Fall Meeting 2010 Abstracts*, page B3. American Geophysical Union.
- ABAD, J. D. & M. H. GARCIA (2009a). Experiments in a high-amplitude Kinoshita meandering channel: 1. Implications of bend orientation on mean and turbulent flow structure. *Water Resour. Res.*, 45(2). doi:10.1029/2008WR007016.
- ABAD, J. D. & M. H. GARCIA (2009b). Experiments in a high-amplitude Kinoshita meandering channel: 2. Implications of bend orientation on bed morphodynamics. *Water Resour. Res.*, 45(2). doi:10.1029/2008WR007017.
- ABREU, V., M. SULLIVAN, C. PIRMEZ & D. MOHRIG (2003). Lateral accretion packages (LAPs): an important reservoir element in deep water sinuous channels. *Mar. Petrol. Geol.*, 20(6–8), 631–648. doi:10.1016/j.marpetgeo.2003.08.003.
- AKHTAR, M. P., N. SHARMA & C. S. P. OJHA (2011). Braiding process and bank erosion in the Brahmaputra River. *International Journal of Sediment Research*, 26(4), 431 – 444. doi:10.1016/S1001-6279(12)60003-1.
- ALFORD, J. J., R. H. BAUMANN & A. J. LEWIS (1982). Circular meander pools. *Earth Surf. Process. Landforms*, 7, 183–188. doi:10.1002/esp.3290070210.
- ANDRLE, R. (1994). Flow structure and development of circular meander pools. *Geomorphology*, 9, 261–270. doi:10.1016/0169-555X(94)90049-3.
- ANDRLE, R. (1996). Measuring channel planform of meandering rivers. *Phys. Geogr.*, 17(3), 270–281. doi:10.1080/02723646.1996.10642585.

BIBLIOGRAPHY

- ASHWORTH, P. J. & J. LEWIN (2012). How do big rivers come to be different? *Earth-Science Reviews*, 114(1–2), 84–107. doi:10.1016/j.earscirev.2012.05.003.
- BAKER, V. R. (2001). Water and the martian landscape. *Nature*, 412(6843), 228–236. doi:10.1038/35084172.
- BELTAOS, S., B. KRISHNAPPAN, R. ROWSELL, T. CARTER, R. PILLING & P. BERGERON (2012). Flow structure and channel stability at the site of a deep scour hole, Mackenzie Delta, Canada. *ARCTIC*, 65(2), 182–194. doi:10.14430/arctic4199.
- VAN BEMMELEN, R. W. (1949). *The geology of Indonesia - General geology of Indonesia and adjacent archipelagos*. Government Printing Office, The Hague; sole agents, Nijhoff.
- BEST, J. L. & P. J. ASHWORTH (1997). Scour in large braided rivers and the recognition of sequence stratigraphic boundaries. *Nature*, 387(6630), 275–277. doi:10.1038/387275a0.
- BIRON, P. M., C. ROBSON, M. F. LAPOINTE & S. J. GASKIN (2004). Comparing different methods of bed shear stress estimates in simple and complex flow fields. *Earth Surf. Process. Landforms*, 29(11), 1403–1415. doi:10.1002/esp.1111.
- BLANCKAERT, K. (2009). Saturation of curvature-induced secondary flow, energy losses, and turbulence in sharp open-channel bends: Laboratory experiments, analysis, and modeling. *J. Geophys. Res.: Earth Surf.*, 114(F3). doi:10.1029/2008JF001137.
- BLANCKAERT, K. (2010). Topographic steering, flow recirculation, velocity redistribution and bed topography in sharp meander bends. *Water Resour. Res.*, 46, W09506. doi:10.1029/2009WR008303.
- BLANCKAERT, K. (2011). Hydrodynamic process in sharp meander bends and their morphological implications. *J. Geophys. Res.*, 116, F01003. doi:10.1029/2010JF001806.
- BLANCKAERT, K., A. DUARTE & A. J. SCHLEISS (2010). Influence of shallowness, bank inclination and bank roughness on the variability of flow patterns and boundary shear stress due to secondary currents in straight open-channels. *Adv. Water Resour.*, 33(9), 1062–1074. doi:10.1016/j.advwatres.2010.06.012.
- BLANCKAERT, K. & W. H. GRAF (2001). Mean flow and turbulence in open-channel bend. *J. Hydraul. Eng.*, 127(10), 835–847. doi:10.1061/(ASCE)0733-9429(2001)127:10(835).
- BLANCKAERT, K., M. G. KLEINHANS, S. J. McLELLAND, W. S. J. UIJTTEWAAL, B. J. MURPHY, A. VAN DE KRUIJS, D. R. PARSONS & Q. CHEN (2013). Flow separation at the inner (convex) and outer (concave) banks of constant-width and widening open-channel bends. *Earth Surf. Process. Landforms*, 38(7), 696–716. doi:10.1002/esp.3324.
- BLANCKAERT, K. & H. J. DE VRIEND (2004). Secondary flow in sharp open-channel bends. *J. Fluid Mech.*, 498, 353–380. doi:10.1017/S0022112003006979.
- BLANCKAERT, K. & H. J. DE VRIEND (2005). Turbulence structure in sharp open-channel bends. *J. Fluid Mech.*, 536, 27–48. doi:10.1017/S0022112005004787.

- BRICE, J. C. (1974). Evolution of meander loops. *Geol. Soc. Am. Bull.*, 85(4), 581–586. doi:10.1130/0016-7606(1974)85<581:EOML>2.0.CO;2.
- BURCHARD, H., P. D. CRAIG, J. R. GEMMRICH, H. VAN HAREN, P.-P. MATHIEU, H. E. M. MEIER, W. A. M. N. SMITH, H. PRANDKE, T. P. RIPPETH, E. D. SKYLLINGSTAD, W. D. SMYTH, D. J. S. WELSH & H. W. WIJESKERA (2008). Observational and numerical modeling methods for quantifying coastal ocean turbulence and mixing. *Prog. Oceanogr.*, 76(4), 399–442. doi:10.1016/j.pocean.2007.09.005.
- BUSCHMAN, F. A., A. J. F. HOITINK, S. M. DE JONG, P. HOEKSTRA, H. HIDAYAT & M. G. SASSI (2012). Suspended sediment load in the tidal zone of an Indonesian river. *Hydrol. Earth Syst. Sci.*, 16(11), 4191–4204. doi:10.5194/hess-16-4191-2012.
- BUSCHMAN, F. A., A. J. F. HOITINK, M. VAN DER VEGT & P. HOEKSTRA (2009). Subtidal water level variation controlled by river flow and tides. *Water Resour. Res.*, 45(10). doi:10.1029/2009WR008167.
- BUSCHMAN, F. A., M. VAN DER VEGT, A. J. F. HOITINK & P. HOEKSTRA (2013). Water and suspended sediment division at a stratified tidal junction. *J. Geophys. Res.: Oceans*, 118(3). doi:10.1002/jgrc.20124.
- CAREY, C. W. (1969). Formation of flood plain lands. *J. Hydraul. Div. ASCE*, 95(HY3), 981–994.
- CHANG, H. H. & J. C. HILL (1977). Minimum stream power for rivers and deltas. *Journal of the Hydraulics Division*, 103(12), 1375–1389.
- CLEVELAND, W. S. (1979). Robust locally weighted regression and smoothing scatterplots. *Journal of the American Statistical Association*, 74(368), 829–836. doi:10.2307/2286407.
- COLEMAN, J. M. (1969). Brahmaputra river: Channel processes and sedimentation. *Sediment. Geol.*, 3(2-3), 129–239. doi:10.1016/0037-0738(69)90010-4.
- COLOMBINI, M. (1993). Turbulence-driven secondary flows and formation of sand ridges. *J. Fluid Mech.*, 254, 701–719. doi:10.1017/S0022112093002319.
- CONSTANTINESCU, G., S. KASHYAP, T. TOKYAY, C. D. RENNIE & R. D. TOWNSEND (2013). Hydrodynamic processes and sediment erosion mechanisms in an open channel bend of strong curvature with deformed bathymetry. *J. Geophys. Res.: Earth*, 118(2), 480–496. doi:10.1002/jgrf.20042.
- DARBY, S. E., H. Q. TRIEU, P. A. CARLING, J. SARKKULA, J. KOPONEN, M. KUMMU, I. CONLAN & J. LEYLAND (2010). A physically based model to predict hydraulic erosion of fine-grained riverbanks: The role of form roughness in limiting erosion. *J. Geophys. Res.: Earth Surf.*, 115(F4). doi:10.1029/2010JF001708.
- DE BOOR, C. (1978). *A practical guide to splines*, volume 27. Springer-Verlag New York.
- DIETRICH, W. E., G. DAY & G. PARKER (1999). The Fly River, Papua New Guinea: Inferences about river dynamics, floodplain sedimentation and fate of sediment. In A. J. Miller & A. Gupta (editors), *Variety of fluvial forms*, pages 345–376. John Wiley & Sons Ltd.

BIBLIOGRAPHY

- DIETRICH, W. E. & J. D. SMITH (1983). Influence of the point bar on flow through curved channels. *Water Resour. Res.*, 19(5), 1173–1192.
- DINEHART, R. L. & J. R. BURAU (2005a). Averaged indicators of secondary flow in repeated acoustic Doppler current profiler crossings of bends. *Water Resour. Res.*, 41, W09405. doi:10.1029/2005WR004050.
- DINEHART, R. L. & J. R. BURAU (2005b). Repeated surveys by acoustic Doppler current profiler for flow and sediment dynamics in a tidal river. *Journal of Hydrology*, 314(1–4), 1–21. doi:10.1016/j.jhydrol.2005.03.019.
- DIVISION OF SOIL SURVEY (1993). *Soil survey manual*. U. S. Dept. of Agriculture, Washington, D. C.
- FERGUSON, R. I., D. R. PARSONS, S. N. LANE & R. J. HARDY (2003). Flow in meander bends with recirculation at the inner bank. *Water Resour. Res.*, 39(11). doi:10.1029/2003WR001965.
- FORNARI, D. (1986). Submarine lava tubes and channels. *Bull. Volcanol.*, 48(5), 291–298. doi:10.1007/BF01081757.
- FROTHINGHAM, K. M. & B. L. RHOADS (2003). Three-dimensional flow structure and channel change in an asymmetrical compound meander loop, Embarras River, Illinois. *Earth Surf. Proc. Land.*, 28(6), 625–644. doi:10.1002/esp.471.
- GARGETT, A. E. (1994). Observing turbulence with a modified Acoustic Doppler Current Profiler. *J. Atmos. Oceanic Technol.*, 11(6), 1592–1610. doi:10.1175/1520-0426(1994)011<1592:OTWAMA>2.0.CO;2.
- VAN GERVEN, L. P. A. & A. J. F. HOITINK (2009). Analysis of river planform geometry with wavelets: application to the Mahakam River reveals geographical zoning. In C. Vionnet, M. H. García, E. M. Latrubesse, & G. M. E. Perillo (editors), *River, Coastal and Estuarine Morphodynamics. RCEM2009*. Santa Fe City, Argentina. CRC Press.
- G HARABAGHI, B., C. INKRATAS, S. BELTAOS & B. KRISHNAPPAN (2007). Modelling of three-dimensional flow velocities in a deep hole in the east channel of the Mackenzie Delta, Northwest Territories. *Can. J. Civ. Eng.*, 34(10), 1312–1323. doi:10.1139/l07-054.
- GONZÁLEZ-CASTRO, J. & M. MUSTE (2007). Framework for estimating uncertainty of ADCP measurements from a moving boat by standardized uncertainty analysis. *J. Hydraul. Eng.*, 133(12), 1390–1410. doi:10.1061/(ASCE)0733-9429(2007)133:12(1390).
- GORDON, R. (1989). Acoustic measurement of river discharge. *J. Hydraul. Eng.*, 115(7), 925–936. doi:10.1061/(ASCE)0733-9429(1989)115:7(925).
- GREELEY, R. (1971). Lunar Hadley rille: considerations of its origin. *Science*, 172(3984), 722–725. doi:10.1126/science.172.3984.722.
- GRENFELL, M., R. AALTO & A. NICHOLAS (2012). Chute channel dynamics in large, sand-bed meandering rivers. *Earth Surface Processes and Landforms*, 37(3), 315–331. doi:10.1002/esp.2257.

- GÜNERALP, İ. & B. L. RHOADS (2009). Empirical analysis of the planform curvature-migration relation of meandering rivers. *Water Resour. Res.*, 45(9). doi:10.1029/2008WR007533.
- GÜNERALP, İ. & B. L. RHOADS (2011). Influence of floodplain erosional heterogeneity on planform complexity of meandering rivers. *Geophys. Res. Lett.*, 38(14), L14401. doi:10.1029/2011GL048134.
- HARDEN, D. R. (1990). Controlling factors in the distribution and development of incised meanders in the central Colorado Plateau. *Geol. Soc. Am. Bull.*, 102(2), 233–242. doi:10.1130/0016-7606(1990)102<0233:CFITDA>2.3.CO;2.
- HARRIS, J., J. L. HIRST & M. J. MOSSINGHOFF (2008). *Combinatorics and graph theory*. Springer. doi:10.1007/978-0-387-79711-3.
- HICKIN, E. J. (1986). Concave-bank benches in the floodplains of Muskwa and Fort Nelson rivers, British Columbia. *The Canadian Geographer*, 30(2), 111–122. doi:10.1111/j.1541-0064.1986.tb01036.x.
- HICKIN, E. J. & G. C. NANSON (1984). Lateral migration rates of river bends. *J. Hydraul. Eng.*, 110(11), 1557–1567. doi:10.1061/(ASCE)0733-9429(1984)110:11(1557).
- HIDAYAT, H., D. H. HOEKMAN, M. A. M. VISSERS & A. J. F. HOITINK (2012). Flood occurrence mapping of the middle Mahakam lowland area using satellite radar. *Hydrol. Earth Syst. Sci.*, 16(7), 1805–1816. doi:10.5194/hess-16-1805-2012.
- HIDAYAT, H., B. VERMEULEN, M. G. SASSI, P. J. J. F. TORFS & A. J. F. HOITINK (2011). Discharge estimation in a backwater affected meandering river. *Hydrol. Earth Syst. Sci.*, 15(8), 2717–2728. doi:10.5194/hess-15-2717-2011.
- HODSKINSON, A. & R. I. FERGUSON (1998). Numerical modelling of separated flow in river bends: model testing and experimental investigation of geometric controls on the extent of flow separation at the concave bank. *Hydrological Processes*, 12, 1323–1338. doi:10.1002/(SICI)1099-1085(19980630)12:8<1323::AID-HYP617>3.0.CO;2-S.
- HOEKMAN, D. H., M. A. M. VISSERS & N. WIELAARD (2010). Palsar wide-area mapping of Borneo: Methodology and map validation. *IEEE J. Sel. Topics Appl. Earth Observ. Remote Sens.*, 3(4), 605–617. doi:10.1109/JSTARS.2010.2070059.
- HOFFMANS, G. (1998). Jet scour in equilibrium phase. *J. Hydraul. Eng.*, 124(4), 430–437. doi:10.1061/(ASCE)0733-9429(1998)124:4(430).
- HOFFMANS, G. J. C. M. & H. J. VERHEIJ (1997). *Scour Manual*. A. A. Balkema, Rotterdam.
- HOITINK, A. J. F. (2004). Tidally-induced clouds of suspended sediment connected to shallow-water coral reefs. *Marine Geology*, 208(1), 13 – 31. doi:10.1016/j.margeo.2004.04.021.
- HOITINK, A. J. F., F. A. BUSCHMAN & B. VERMEULEN (2009). Continuous measurements of discharge from a horizontal acoustic Doppler current profiler in a tidal river. *Water Resour. Res.*, 45(11). doi:10.1029/2009WR007791.

BIBLIOGRAPHY

- HOITINK, A. J. F. & P. HOEKSTRA (2005). Observations of suspended sediment from ADCP and OBS measurements in a mud-dominated environment. *Coastal Eng.*, 52(2), 103 – 118. doi:10.1016/j.coastaleng.2004.09.005.
- HOOKE, J. (2003). River meander behaviour and instability: a framework for analysis. *Trans. Inst. Br. Geogr.*, 28(2), 238–253. doi:10.1111/1475-5661.00089.
- HOOKE, J. M. (2007). Complexity, self-organisation and variation in behaviour in meandering rivers. *Geomorphology*, 91(3–4), 236–258. doi:10.1016/j.geomorph.2007.04.021.
- HOWARD, A. D. & A. T. HEMBERGER (1991). Multivariate characterization of meandering. *Geomorphology*, 4(3–4), 161–186. doi:10.1016/0169-555X(91)90002-R.
- IKEDA, S., G. PARKER & K. SAWAI (1981). Bend theory of river meanders. Part 1. Linear development. *J. Fluid Mech.*, 112, 363–377. doi:10.1017/S0022112081000451.
- IUSS WORKING GROUP WRB (2007). *World reference base for soil resources 2006, first update 2007*. Number 103 in World soil resources reports. Food and Agriculture Organization of the United Nations, Rome.
- JAMIESON, E. C., G. POST & C. D. RENNIE (2010). Spatial variability of three-dimensional Reynolds stresses in a developing channel bend. *Earth Surf. Process. Landforms*, 37, 1029–1043. doi:10.1002/esp.1930.
- JAMIESON, E. C., C. D. RENNIE, R. B. JACOBSON & R. D. TOWNSEND (2011). 3-D flow and scour near a submerged wing dike: ADCP measurements on the Missouri River. *Water Resour. Res.*, 47(7). doi:10.1029/2010WR010043.
- JOHNSON, R. A. & D. W. WICHERN (2007). *Applied multivariate statistical analysis*. Pearson Prentice Hall, Pearson Education International, Upper Saddle River.
- KARLSTROM, L., P. GAJJAR & M. MANGA (2013). Meander formation in supraglacial streams. *J. Geophys. Res.: Earth Surf.*, 118(3), 1897–1907. doi:10.1002/jgrf.20135.
- KAWANISI, K. (2004). Structure of turbulent flow in a shallow tidal estuary. *J. Hydraul. Eng.*, 130(4), 360–370. doi:10.1061/(ASCE)0733-9429(2004)130:4(360).
- KIM, D., M. MUSTE, D. S. MUELLER & M. WINKLER (2009). A quick tutorial for using VMS. http://chl.erdc.usace.army.mil/Media/1/1/2/0/VMS_quick_tutorial.pdf.
- KIM, S. C., C. FRIEDRICHS, J. P.-Y. MAA & L. D. WRIGHT (2000). Estimating bottom stress in tidal boundary layer from acoustic doppler velocimeter data. *J. Hydraul. Eng.*, 126(6), 399–406. doi:10.1061/(ASCE)0733-9429(2000)126:6(399).
- KINOSHITA, R. (1961). *An investigation of channel migration in the Ishikari river*. Technical Report 13, Department of Resources, Office of Science and Technology, Japan, Japan.
- KOLLA, V., H. W. POSAMENTIER & L. J. WOOD (2007). Deep-water and fluvial sinuous channels – characteristics, similarities and dissimilarities, and modes of formation. *Mar. Petrol. Geol.*, 24(6–9), 388–405. doi:10.1016/j.marpetgeo.2007.01.007.

- KOMATSU, G. & V. R. BAKER (1994). Meander properties of Venusian channels. *Geology*, 22(1), 67–70. doi:10.1130/0091-7613(1994)022<0067:MPOVC>2.3.CO;2.
- KOSTASCHUK, R., J. BEST, P. VILLARD, J. PEAKALL & M. FRANKLIN (2005). Measuring flow velocity and sediment transport with an acoustic Doppler current profiler. *Geomorphology*, 68(1–2), 25–37. doi:10.1016/j.geomorph.2004.07.012.
- KREB, D. & BUDIONO (2005). Conservation management of small core areas: key to survival of a critically endangered population of Irrawaddy river dolphins *Orcaella brevirostris* in Indonesia. *Oryx*, 39(2), 178–188. doi:10.1017/S0030605305000426.
- KUIJPER, A. (2004). On detecting all saddle points in 2D images. *Pattern. Recogn. Lett.*, 25(15), 1665–1672. doi:10.1016/j.patrec.2004.06.017.
- LABEUR, R. & G. WELLS (2012). Energy stable and momentum conserving hybrid finite element method for the incompressible navier-stokes equations. *SIAM Journal on Scientific Computing*, 34(2), A889–A913. doi:10.1137/100818583.
- LABEUR, R. J. & J. D. PIETRZAK (2005). A fully three dimensional unstructured grid non-hydrostatic finite element coastal model. *Ocean Model.*, 10(1–2), 51–67. doi:10.1016/j.ocemod.2004.06.008.
- LABEUR, R. J. & G. N. WELLS (2007). A Galerkin interface stabilisation method for the advection–diffusion and incompressible Navier–Stokes equations. *Comp. Method. Appl. M.*, 196(49–52), 4985–5000. doi:10.1016/j.cma.2007.06.025.
- LABEUR, R. J. & G. N. WELLS (2009). Interface stabilised finite element method for moving domains and free surface flows. *Comp. Method. Appl. M.*, 198(5–8), 615–630. doi:10.1016/j.cma.2008.09.014.
- LANE, S. N., D. R. PARSONS, J. L. BEST, O. ORFEO, R. A. KOSTASCHUK & R. J. HARDY (2008). Causes of rapid mixing at a junction of two large rivers: Río Paraná and Río Paraguay, Argentina. *J. Geophys. Res.: Earth Surf.*, 113(F2). doi:10.1029/2006JF000745.
- LATRUBESSE, E. M., J. C. STEVAUX & R. SINHA (2005). Tropical rivers. *Geomorphology*, 70, 187–206. doi:10.1016/j.geomorph.2005.02.005.
- LAZARUS, E. D. & J. A. CONSTANTINE (2013). Generic theory for channel sinuosity. *P. Natl. Acad. Sci. USA*, 110(21), 8447–8452. doi:10.1073/pnas.1214074110.
- LE BOT, P., C. KERMAISON, P. LHERMINIER & F. GAILLARD (2011). *CASCADE V6.1: Logiciel de validation et de visualisation des mesures ADCP de coque*. Technical Report OPS/LPO 11-01, Ifremer, Centre de Brest, France.
- LE COZ, J., M. MICHALKOVÁ, A. HAUET, M. ČOMAJ, G. DRAMAIS, K. HOLUBOVÁ, H. PRÉ-GAY & A. PAQUIER (2010). Morphodynamics of the exit of a cutoff meander: experimental findings from field and laboratory studies. *Earth Surf. Proc. Land.*, 35(3), 249–261. doi:10.1002/esp.1896.

BIBLIOGRAPHY

- LE COZ, J., G. PIERREFEU & A. PAQUIER (2008). Evaluation of river discharges monitored by a fixed side-looking Doppler profiler. *Water Resour. Res.*, 44(4). doi:10.1029/2008WR006967.
- LE GRAND-PITEIRA, N., A. DAERR & L. LIMAT (2006). Meandering rivulets on a plane: A simple balance between inertia and capillarity. *Phys. Rev. Lett.*, 96, 254503. doi:10.1103/PhysRevLett.96.254503.
- LEGLEITER, C. J. & P. C. KYRIAKIDIS (2006). Forward and inverse transformations between cartesian and channel-fitted coordinate systems for meandering rivers. *Math. Geol.*, 38(8), 927–958. doi:10.1007/s11004-006-9056-6.
- LIMAYE, A. B. S. & M. P. LAMB (2014). Numerical simulations of bedrock valley evolution by meandering rivers with variable bank material. *J. Geophys. Res.: Earth Surf.*, 119(4), 927–950. doi:10.1002/2013JF002997.
- LOHRMANN, A., B. HACKETT & L. P. RØED (1990). High resolution measurements of turbulence, velocity and stress using a pulse-to-pulse coherent sonar. *J. Atmos. Oceanic Technol.*, 7(1), 19–37. doi:10.1175/1520-0426(1990)007<0019:HRMOTV>2.0.CO;2.
- LU, Y. & R. G. LUECK (1999a). Using a broadband ADCP in a tidal channel. Part I: Mean flow and shear. *J. Atmos. Oceanic Technol.*, 16, 1556–1567. doi:10.1175/1520-0426(1999)016<1556:UABAIA>2.0.CO;2.
- LU, Y. & R. G. LUECK (1999b). Using a broadband ADCP in a tidal channel. Part II: Turbulence. *J. Atmos. Oceanic Technol.*, 16(11), 1568–1579. doi:10.1175/1520-0426(1999)016<1568:UABAIA>2.0.CO;2.
- LUECK, R., F. WOLK & H. YAMAZAKI (2002). Oceanic velocity microstructure measurements in the 20th century. *J. Oceanogr.*, 58, 153–174. doi:10.1023/A:1015837020019.
- MAKASKE, B. & H. J. T. WEERTS (2005). Muddy lateral accretion and low stream power in a sub-recent confined channel belt, Rhine-Meuse delta, central Netherlands. *Sedimentology*, 52, 651–668. doi:10.1111/j.1365-3091.2005.00713.x.
- MALIN, M. C. & K. S. EDGETT (2003). Evidence for persistent flow and aqueous sedimentation on early Mars. *Science*, 302(5652), 1931–1934. doi:10.1126/science.1090544.
- MARANI, M., S. LANZONI, D. ZANDOLIN, G. SEMINARA & A. RINALDO (2002). Tidal meanders. *Water Resour. Res.*, 38(11), 1225. doi:10.1029/2001WR000404.
- MARSDEN, R. F. & Y. GRATTON (1997). A method for correcting vertical velocities measured from a vessel-mounted acoustic Doppler current profiler. *J. Atmos. Oceanic Technol.*, 14(6), 1533–1538. doi:10.1175/1520-0426(1997)014<1533:AMFCVV>2.0.CO;2.
- MARSDEN, R. F. & R. G. INGRAM (2004). Correcting for beam spread in acoustic Doppler current profiler measurements. *J. Atmos. Oceanic Technol.*, 21(9), 1491–1498. doi:10.1175/1520-0426(2004)021<1491:CFBSIA>2.0.CO;2.

- MESHKOVA, L. V. & P. A. CARLING (2012). The geomorphological characteristics of the Mekong River in northern Cambodia: A mixed bedrock-alluvial multi-channel network. *Geomorphology*, 147-148(0), 2-17. doi:10.1016/j.geomorph.2011.06.041.
- MOHRHOLZ, V., H. PRANDKE & H. U. LASS (2008). Estimation of TKE dissipation rates in dense bottom plumes using a Pulse Coherent Acoustic Doppler Profiler (PC-ADP) – Structure function approach. *J. Mar. Syst.*, 70(3-4), 217 – 239. doi:10.1016/j.jmarsys.2007.03.004.
- MONTGOMERY, D. R. (1997). River management: What's best on the banks? *Nature*, 388(6640), 328-329.
- MOORE, S. A., J. L. COZ, D. HURTER & A. PAQUIER (2012). On the application of horizontal ADCPs to suspended sediment transport surveys in rivers. *Continental Shelf Research*, 46(0), 50 – 63. doi:10.1016/j.csr.2011.10.013.
- MUSTE, M., D. KIM & J. GONZÁLEZ-CASTRO (2010). Near-transducer errors in ADCP measurements: Experimental findings. *J. Hydraul. Eng.*, 136(5), 275-289. doi:10.1061/(ASCE)HY.1943-7900.0000173.
- MUSTE, M., K. YU, T. PRATT & D. ABRAHAM (2004a). Practical aspects of adcp data use for quantification of mean river flow characteristics; Part II: Fixed-vessel measurements. *Flow Meas. Inst.*, 15(1), 17-28. doi:10.1016/j.flowmeasinst.2003.09.002.
- MUSTE, M., K. YU & M. SPASOJEVIC (2004b). Practical aspects of adcp data use for quantification of mean river flow characteristics; Part I: Moving-vessel measurements. *Flow Meas. Inst.*, 15(1), 1-16. doi:10.1016/j.flowmeasinst.2003.09.001.
- NANSON, R. A. (2010). Flow fields in tightly curving meander bends of low width-depth ratio. *Earth Surf. Process. Landforms*, 35(2), 119-135. doi:10.1002/esp.1878.
- NANSON, R. A., G. C. NANSON & H. Q. HUANG (2010). The hydraulic geometry of narrow and deep channels; evidence for flow optimisation and controlled peatland growth. *Geomorphology*, 117(1-2), 143-154. doi:10.1016/j.geomorph.2009.11.021.
- NAQSHBAND, S., J. S. RIBBERINK, D. HURTER & S. J. M. H. HULSCHER (2014). Bed load and suspended load contributions to migrating sand dunes in equilibrium. *J. Geophys. Res.: Earth*, 119(5), 1043-1063. doi:10.1002/2013JF003043.
- NEZU, I. (2005). Open-channel flow turbulence and its research prospect in the 21st century. *J. Hydraul. Eng.*, 131(4), 229-246. doi:10.1061/(ASCE)0733-9429(2005)131:4(229).
- NEZU, I. & H. NAKAGAWA (1993). *Turbulence in Open-Channel Flows*. A. A. Balkema, Rotterdam.
- NIDZIEKO, N. J., D. A. FONG & J. L. HENCH (2006). Comparison of Reynolds stress estimates derived from standard and fast-ping ADCPs. *J. Atmos. Oceanic Technol.*, 23(6), 854-861. doi:10.1175/JTECH1885.1.

BIBLIOGRAPHY

- NIHEI, Y. & A. KIMIZU (2008). A new monitoring system for river discharge with horizontal acoustic Doppler current profiler measurements and river flow simulation. *Water Resour. Res.*, 44(4). doi:[10.1029/2008WR006970](https://doi.org/10.1029/2008WR006970).
- VAN NOORTWIJK, J. & H. KLATTER (1999). Optimal inspection decisions for the block mats of the Eastern-Scheldt barrier. *Reliability Engineering & System Safety*, 65(3), 203 – 211. doi:[http://dx.doi.org/10.1016/S0951-8320\(98\)00097-0](http://dx.doi.org/10.1016/S0951-8320(98)00097-0).
- NYSTROM, E. A., C. R. REHMANN & K. A. OBERG (2007). Evaluation of mean velocity and turbulence measurements with ADCPs. *J. Hydraul. Eng.*, 133(12), 1310–1318. doi:[10.1061/\(ASCE\)0733-9429\(2007\)133:12\(1310\)](https://doi.org/10.1061/(ASCE)0733-9429(2007)133:12(1310)).
- ODGAARD, A. J. (1981). Transverse bed slope in alluvial channel bends. *Journal of Hydraulics Division*, 107(12), 1677–1694.
- O'NEILL, M. P. & A. D. ABRAHAMS (1986). Objective identification of meanders and bends. *J. Hydrol.*, 83(3–4), 337–353. doi:[10.1016/0022-1694\(86\)90160-5](https://doi.org/10.1016/0022-1694(86)90160-5).
- OTTEVANGER, W., K. BLANCKAERT, W. S. J. UIJTTEWAAL & H. J. DE VRIEND (2013). Meander dynamics: A reduced-order nonlinear model without curvature restrictions for flow and bed morphology. *Journal of Geophysical Research: Earth Surface*, 118(2), 1118–1131. doi:[10.1002/jgrf.20080](https://doi.org/10.1002/jgrf.20080).
- OTTEVANGER, W., K. BLANCKAERT & W. S. J. UIJTTEWAAL (2012). Processes governing the flow redistribution in sharp river bends. *Geomorphology*, 163–164(0), 45–55. doi:[10.1016/j.geomorph.2011.04.049](https://doi.org/10.1016/j.geomorph.2011.04.049).
- PAGE, K. & G. C. NANSON (1982). Concave-bank benches and associated floodplain formation. *Earth Surf. Process. Landforms*, 7, 529–543. doi:[10.1002/esp.3290070603](https://doi.org/10.1002/esp.3290070603).
- PARKER, G., P. DIPLAS & J. AKIYAMA (1983). Meander bends of high amplitude. *J. Hydraul. Eng.*, 109(10), 1323–1337. doi:[10.1061/\(ASCE\)0733-9429\(1983\)109:10\(1323\)](https://doi.org/10.1061/(ASCE)0733-9429(1983)109:10(1323)).
- PARKER, G., K. SAWAI & S. IKEDA (1982). Bend theory of river meanders. Part 2. Non-linear deformation of finite-amplitude bends. *J. Fluid Mech.*, 115, 303–314.
- PARSONS, D. R., J. L. BEST, O. ORFEO, R. J. HARDY, R. KOSTASCHUK & S. N. LANE (2005). Morphology and flow fields of three-dimensional dunes, Rio Paraná, Argentina: Results from simultaneous multibeam echo sounding and acoustic Doppler current profiling. *J. Geophys. Res.: Earth Surf.*, 110(F4). doi:[10.1029/2004JF000231](https://doi.org/10.1029/2004JF000231).
- PARSONS, D. R., P. R. JACKSON, J. A. CZUBA, F. L. ENGEL, B. L. RHOADS, K. A. OBERG, J. L. BEST, D. S. MUELLER, K. K. JOHNSON & J. D. RILEY (2013). Velocity mapping toolbox (VMT): a processing and visualization suite for moving-vessel ADCP measurements. *Earth Surf. Proc. Land.* doi:[10.1002/esp.3367](https://doi.org/10.1002/esp.3367).
- PEAKALL, J., B. MCCAFFREY & B. KNELLER (2000). A process model for the evolution, morphology, and architecture of sinuous submarine channels. *J. Sediment. Res.*, 70(3), 434–448. doi:[10.1306/2DC4091C-0E47-11D7-8643000102C1865D](https://doi.org/10.1306/2DC4091C-0E47-11D7-8643000102C1865D).
- PETERS, H. & W. E. JOHNS (2006). Bottom layer turbulence in the Red Sea outflow plume. *J. Phys. Oceanogr.*, 36(9), 1763–1785. doi:[10.1175/JPO2939.1](https://doi.org/10.1175/JPO2939.1).

- PILARCZYK, K. W. (2011). *Coastal and ocean engineering practice*, volume 1 of *Series on coastal and ocean engineering practice*, chapter Impact of the Delta Works on the Recent Developments in Coastal Engineering, pages 1–37. World Scientific.
- REICHEL, G. & H. P. NACHNEBEL (1994). Suspended sediment monitoring in a fluvial environment: advantages and limitations applying an acoustic doppler current profiler. *Water Resources*, 28(4), 751–761. doi:10.1016/0043-1354(94)90083-3.
- RENNIE, C., R. MILLAR & M. CHURCH (2002). Measurement of bed load velocity using an acoustic Doppler current profiler. *J. Hydraul. Eng.*, 128(5), 473–483. doi:10.1061/(ASCE)0733-9429(2002)128:5(473).
- RHOADS, B. L. & A. N. SUKHODOLOV (2001). Field investigation of three-dimensional flow structure at stream confluences: 1. Thermal mixing and time-averaged velocities. *Water Resour. Res.*, 37(9), 2393–2410. doi:10.1029/2001WR000316.
- RHOADS, B. L. & A. N. SUKHODOLOV (2004). Spatial and temporal structure of shear layer turbulence at a stream confluence. *Water Resour. Res.*, 40, W06304. doi:10.1029/2003WR002811.
- RICHARDSON, W. & C. R. THORNE (2001). Multiple thread flow and channel bifurcation in a braided river: Brahmaputra–Jamuna River, Bangladesh. *Geomorphology*, 38(3–4), 185 – 196. doi:10.1016/S0169-555X(00)00080-5.
- RINALDI, M. & P. JOHNSON (1997). Characterization of stream meanders for stream restoration. *J. Hydraul. Eng.*, 123(6), 567–570. doi:10.1061/(ASCE)0733-9429(1997)123:6(567).
- RIPPETH, T. P., E. WILLIAMS & J. H. SIMPSON (2002). Reynolds stress and turbulent energy production in a tidal channel. *J. Phys. Oceanogr.*, 32(4), 1242–1251. doi:10.1175/1520-0485(2002)032<1242:RSATEP>2.0.CO;2.
- ROWLAND, J. C. (2007). *Tie Channels*. Ph.D. thesis, University of California.
- ROWLAND, J. C., W. E. DIETRICH, G. DAY & G. PARKER (2009). Formation and maintenance of single-thread tie channels entering floodplain lakes: Observations from three diverse river systems. *J. Geophys. Res.: Earth Surf.*, 114(F2). doi:10.1029/2008JF001073.
- RUBIN, D. M., J. C. SCHMIDT & J. N. MOORE (1990). Origin, structure and evolution of reattachment bar, Colorado River, Grand Canyon, Arizona. *J. Sediment. Petrol.*, 60(6), 982–991. doi:10.1306/D426765E-2B26-11D7-8648000102C1865D.
- SASSI, M. G., A. J. F. HOITINK, B. BRYE, B. VERMEULEN & E. DELEERSNIJDER (2011a). Tidal impact on the division of river discharge over distributary channels in the Mahakam Delta. *Ocean Dynam.*, 61(12), 2211–2228. doi:10.1007/s10236-011-0473-9.
- SASSI, M. G., A. J. F. HOITINK & B. VERMEULEN (2012). Impact of sound attenuation by suspended sediment on ADCP backscatter calibrations. *Water Resour. Res.*, 48(9). doi:10.1029/2012WR012008.

BIBLIOGRAPHY

- SASSI, M. G., A. J. F. HOITINK, B. VERMEULEN & HIDAYAT (2011b). Discharge estimation from H-ADCP measurements in a tidal river subject to sidewall effects and a mobile bed. *Water Resour. Res.*, 47(6). doi:10.1029/2010WR009972.
- SASSI, M. G., A. J. F. HOITINK, B. VERMEULEN & H. HIDAYAT (2013). Sediment discharge division at two tidally influenced river bifurcations. *Water Resour. Res.*, 49(4). doi:10.1002/wrcr.20216.
- SCHNAUDER, I. & A. N. SUKHODOLOV (2012). Flow in a tightly curving meander bend: effects of seasonal changes in aquatic macrophyte cover. *Earth Surf. Process. Landforms*, 37(11), 1142–1157. doi:10.1002/esp.3234.
- SCHUMM, S. A. (1967). Meander wavelength of alluvial rivers. *Science*, 157(3796), 1549–1550. doi:10.1126/science.157.3796.1549.
- SEMINARA, G. (2006). Meanders. *J. Fluid Mech.*, 554, 271–297. doi:10.1017/S0022112006008925.
- SEMINARA, G. & M. TUBINO (2001). Sand bars in tidal channels. Part 1. Free bars. *J. Fluid Mech.*, 440, 49–74. doi:10.1017/S0022112001004748.
- SIMARMATA, R. (2010). Legal complexity in natural resource management in the frontier Mahakam Delta of East Kalimantan, Indonesia. *The Journal of Legal Pluralism and Unofficial Law*, 42(62), 115–146. doi:10.1080/07329113.2010.10756652.
- SMITH, W. A. M. N., J. KATZ & T. R. OSBORN (2005). On the structure of turbulence in the bottom boundary layer of the coastal ocean. *J. Phys. Oceanogr.*, 35(1), 72–93. doi:10.1175/JPO-2673.1.
- SOULSBY, R. L. (1980). Selecting record length and digitization rate for near-bed turbulence measurements. *J. Phys. Oceanogr.*, 10(2), 208–219. doi:10.1175/1520-0485(1980)010<0208:SRLADR>2.0.CO;2.
- SOUZA, A. J., L. G. ALVAREZ & T. D. DICKEY (2004). Tidally induced turbulence and suspended sediment. *Geophys. Res. Lett.*, 31, L20309. doi:10.1029/2004GL021186.
- STACEY, M. T., S. G. MONISMITH & J. R. BURAU (1999a). Measurements of Reynolds stress profiles in unstratified tidal flow. *J. Geophys. Res.: Oceans*, 104(C5), 10933–10949. doi:10.1029/1998JC900095.
- STACEY, M. T., S. G. MONISMITH & J. R. BURAU (1999b). Observations of turbulence in a partially stratified estuary. *J. Phys. Oceanogr.*, 29, 1950–1970. doi:10.1175/1520-0485(1999)029<1950:OOTIAP>2.0.CO;2.
- STARK, C. P., J. R. BARBOUR, Y. S. HAYAKAWA, T. HATTANJI, N. HOVIUS, H. CHEN, C.-W. LIN, M.-J. HORNG, K.-Q. XU & Y. FUKAHATA (2010). The climatic signature of incised river meanders. *Science*, 327(5972), 1497–1501. doi:10.1126/science.1184406.
- STORMS, J. E. A., R. M. HOOGENDOORN, R. A. C. DAM, A. J. F. HOITINK & S. B. KROONENBERG (2005). Late-holocene evolution of the Mahakam delta, East Kalimantan, Indonesia. *Sedimentary geology*, 180, 149–166.

- SUKHODOLOV, A. N. (2014). Hydrodynamics of groyne fields in a straight river reach: insight from field experiments. *J. Hydraul. Res.*, 52(1), 105–120. doi:10.1080/00221686.2014.880859.
- SUKHODOLOV, A. N., M. THIELE & H. BUNGARTZ (1998). Turbulence structure in a river reach with sand bed. *Water Resour. Res.*, 34(5), 1317–1334. doi:10.1029/98WR00269.
- SZUPIANY, R., M. AMSLER, J. BEST & D. PARSONS (2007). Comparison of fixed- and moving-vessel flow measurements with an aDp in a large river. *J. Hydraul. Eng.*, 133(12), 1299–1309. doi:10.1061/(ASCE)0733-9429(2007)133:12(1299).
- SZUPIANY, R. N., M. L. AMSLER, J. HERNANDEZ, D. R. PARSONS, J. L. BEST, E. FORNARI & A. TRENTO (2012). Flow fields, bed shear stresses, and suspended bed sediment dynamics in bifurcations of a large river. *Water Resour. Res.*, 48(11). doi:10.1029/2011WR011677.
- SÖZER, R. & V. NIJMAN (2005). Effects of enso-induced forest fires and habitat disturbance on the abundance and spatial distribution of an endangered riverine bird in borneo. *Animal Conservation*, 8(1), 27–31. doi:10.1017/S1367943004001787.
- TARRAB, L., C. M. GARCÍA, M. I. CANTERO & K. OBERG (2012). Role of turbulence fluctuations on uncertainties of acoustic Doppler current profiler discharge measurements. *Water Resour. Res.*, 48(6). doi:10.1029/2011WR011185.
- TARYA, A., A. J. F. HOITINK & M. VAN DER VEGT (2010). Tidal and subtidal flow patterns on a tropical continental shelf semi-insulated by coral reefs. *Journal of Geophysical Research: Oceans*, 115(C9). doi:10.1029/2010JC006168.
- TELEDYNE RD INSTRUMENTS (2010). *ADCP Coordinate Transformation - Formulas and Calculations*. San Diego, California.
- THOMPSON, A. (1986). Secondary flows and the pool-riffle unit: A case study of the processes of meander development. *Earth Surf. Proc. Land.*, 11(6), 631–641. doi:10.1002/esp.3290110606.
- THORNE, C. R. (1998). *Stream Reconnaissance Handbook: Geomorphological Investigation and Analysis of River Channel*. John Wiley and Sons, New York.
- THORNE, P. D. & D. M. HANES (2002). A review of acoustic measurement of small-scale sediment processes. *Continental Shelf Research*, 22(4), 603 – 632. doi:10.1016/S0278-4343(01)00101-7.
- TOKYAY, T., G. CONSTANTINESCU & J. GONZALEZ-CASTRO (2009). Investigation of two elemental error sources in boat-mounted acoustic Doppler current profiler measurements by large eddy simulations. *J. Hydraul. Eng.*, 135(11), 875–887. doi:10.1061/(ASCE)HY.1943-7900.0000083.
- TOMINAGA, A. & I. NEZU (1991). Turbulent structure in compound open-channel flows. *J. Hydraul. Eng.*, 117(1), 21–41. doi:10.1061/(ASCE)0733-9429(1991)117:1(21).
- TORRENCE, C. & G. P. COMPO (1998). A practical guide to wavelet analysis. *B. Am. Meteorol. Soc.*, 79(1), 61–78. doi:10.1175/1520-0477(1998)079<0061:APGTWA>2.0.CO;2.

BIBLIOGRAPHY

- VERMAAS, D. A., W. S. UIJTTEWAAL & A. J. F. HOITINK (2011). Lateral transfer of streamwise momentum caused by a roughness transition across a shallow channel. *Water Resour. Res.* doi:10.1029/2010WR010138.
- WEI, T. & W. W. WILLMARTH (1989). Reynolds-number effects on the structure of a turbulent channel flow. *J. Fluid Mech.*, 204, 57–95. doi:10.1017/S0022112089001667.
- WERNER, B. T. (1999). Complexity in natural landform patterns. *Science*, 284(5411), 102–104. doi:10.1126/science.284.5411.102.
- WHIPPLE, A., R. LUETTICH & H. SEIM (2006). Measurements of Reynolds stress in a wind-driven lagoonal estuary. *Ocean Dynam.*, 56, 169–185. doi:10.1007/s10236-005-0038-x.
- WILCOCK, P. R. (1996). Estimating local bed shear stress from velocity observations. *Water Resour. Res.*, 32(11), 3361–3366. doi:10.1029/96WR02277.
- WILES, P. J., T. P. RIPPETH, J. H. SIMPSON & P. J. HENDRICKS (2006). A novel technique for measuring the rate of turbulent dissipation in the marine environment. *Geophys. Res. Lett.*, 33, L21608. doi:10.1029/2006GL027050.
- WILLIAMS, E. & J. H. SIMPSON (2004). Uncertainties in estimates of Reynolds stress and TKE production rate using the ADCP variance method. *J. Atmos. Oceanic Technol.*, 21, 347–357. doi:10.1175/1520-0426(2004)021<0347:UUEORS>2.0.CO;2.
- WITKIN, A. P. (1984). Scale-space filtering: A new approach to multi-scale description. In *Acoustics, Speech, and Signal Processing, IEEE International Conference on ICASSP '84*, volume 9, pages 150–153. doi:10.1109/ICASSP.1984.1172729.
- WOODYER, K. D. (1975). Concave-bank benches on Barwon river, N. S. W. *Australian Geographer*, 13(1), 36–40. doi:10.1080/00049187508702676.
- YANG, S.-Q. & J. A. MCCORQUODALE (2004). Determination of boundary shear stress and reynolds shear stress in smooth rectangular channel flows. *J. Hydraul. Eng.*, 130(5), 458–462. doi:10.1061/(ASCE)0733-9429(2004)130:5(458).
- ZOLEZZI, G. & G. SEMINARA (2001). Downstream and upstream influence in river meandering. Part 1. General theory and application to overdeepening. *J. Fluid Mech.*, 438, 183–211. doi:10.1017/S002211200100427X.

Acknowledgments

Het is zo'n acht jaar geleden dat Ton mij vroeg of ik interesse had in een promotietraject waarin ik de Mahakam rivier zou gaan bestuderen. Met de beelden nog op het netvlies van een prachtig tropisch eiland waar ik mijn afstudeeronderzoek had gedaan was de keuze snel gemaakt. Helaas moest ik de kraakheldere riffen wel omruilen voor een modderige rivier, maar het onderzoek wat ik heb mogen doen is me meer en meer gaan interesseren en fascineren. Ton, zonder alle tijd, de passie en het enthousiasme waarmee je mij als promovendus hebt begeleid had dit proefschrift er niet gelegen. Bedankt voor alle gesprekken en discussies waarin jouw scherpe en ambitieuze kijk mijn ideeën heeft gevormd en mij heeft uitgedaagd om verder en dieper te gaan in het onderzoek. Bedankt voor het vertrouwen dat je in me hebt gesteld om veel (dwaze) ideeën uit te kunnen werken en dat je me zo nu en dan ook hebt tegengehouden om niet af te dwalen en zo mijn focus te houden.

Remko, in de afgelopen jaren heb ik het voorrecht gehad om bij de HWM groep te werken. De ontspannen en gezellige sfeer binnen de groep is voor een groot deel aan jouw ontspannenheid en persoonlijke betrokkenheid te danken. Bedankt ook voor het doornemen van mijn teksten, soms tot in de kleine uurtjes, en het waardevolle commentaar.

Hidayat and Maxi, I am very grateful for the time we spent together in Indonesia and the continued collaboration in the years after. Each of us comes from a different continent and our cultures are as different as it gets, but the fieldwork we did together could not have been better. Hidayat, I enjoyed your humor and got impressed by your perseverance during fieldwork. What a hard worker you are! Maxi, thanks a lot for all the conversations we had, the assados, play-

ing basketball, etc. Somehow I always feel a bit back in Italy when you are around. I would like to thank all my (ex-)colleagues at the HWM group for the great time I had in the past years. Paul, thanks for all the help and discussions on statistics, mathematics, etc. Roel, thanks for your support during the startup of the fieldwork.

Ik ben ontzettend dankbaar voor al het kundige werk van Pieter Hazenberg, Johan Römelingh en Herman Jansen, bij de voorbereidingen en tijdens het veldwerk. During the fieldwork I got great support from Budi Sulistioadi and Wawan Kustiawan (Mulawarman University), Ibu Gadis, Unggul Handoko and Fajar Setiawan (LIPI), and several students from Mulawarman University. Dank aan Rijks-waterstaat, NIOZ en Universiteit Utrecht voor alle meetapparatuur die we konden gebruiken in het veld. Ik heb het voorrecht gehad om een aantal studenten te mogen begeleiden in hun BSc en MSc traject. In het bijzonder wil ik Sonja van Berkum en Jan Gooijer bedanken voor hun bijdrage tijdens het veldwerk. Al waren jullie niet direct betrokken bij het Mahakam project, Marcel van Maarseveen, Frans Buschman en David Vermaas, bedankt voor alles wat ik van, en met jullie heb mogen leren over veldwerk, ADCPs, duiken, enz. in de Berau. Een deel van het werk in deze thesis was niet mogelijk geweest zonder de hulp van Robert Jan Labeur. Bedankt dat ik gebruik kon maken van Finlab en dat je er zoveel tijd in hebt gestopt om het model aan te passen. Ik heb het erg leuk gevonden om een week in Delft samen aan het model te werken en ik heb veel geleerd van jouw inzicht in de vloeistofmechanica. I am thankful to Eric Deleersnijder for the time I spent in his group learning how to use the SLIM model. I would like to thank Prof. Safwan Hadi (Institute of Technology Bandung) for his contribution to the project. Many thanks for the help and interaction we had to all researchers in the East Kalimantan Programme, and in particular to Prof. Salomon Kroonoberg as the leader of the Mahakam Cluster. Dirk Hoekman is acknowledged for providing us with the PALSAR images.

Jerke, ontzettend bedankt voor je vriendschap. Ik ben heel dankbaar voor jouw openheid, dat je durft te confronteren, altijd weer een stap dieper wilt gaan en bespreekbaar maakt wat maar weinigen durven te bespreken. Michele grazie per un'amicizia così preziosa e unica. Non so come fai, ma le circostanze non ti impediscono mai di portare tanta allegria e di far sentire chiunque a suo agio. Dagli ultimi anni di liceo, alla realizzazione di questa tesi, e sono convinto

anche per il resto della mia vita, so di poter contare su di un grande amico! Machiel, heel erg bedankt voor het mooie ontwerp van de kaft van dit proefschrift, maar nog veel meer voor wie je bent en wat je voor me betekent. Je bruist van ideeën, durft nieuwe uitdagingen aan en bent kritisch op een heel prettige manier. Ik heb veel steun ervaren doordat je altijd hebt geloofd in mijn meest wilde ideeën rondom mijn proefschrift en je altijd geïnteresseerd bent geweest in mijn onderzoek.

Mijn ouders, zussen en schoonfamilie wil ik graag bedanken voor alle gezellige momenten die we regelmatig met elkaar hebben. Bedankt voor jullie interesse in mijn werk en alle steun die ik van jullie heb ervaren. Pa en Ma, bedankt dat jullie in de opvoeding zoveel van jezelf aan mij hebben doorgegeven, door vooral jezelf te zijn en altijd te staan voor waar jullie in geloven en er naar te handelen. Pa, ik heb erg genoten van alle gezellige Ardennen weekenden samen. Ik wil Vader God danken als mijn belangrijkste bron van inspiratie en relativering. Evelien, Naomi en Lianne, ik ben ontzettend trots op jullie en heel erg dankbaar voor alle tijd en ruimte die jullie mij hebben gegeven om mijn proefschrift te kunnen afronden. Bij jullie zijn is altijd thuis zijn, en even lekker afstand nemen van mijn werk! Evelien, bedankt voor al jouw steun, liefde, begrip en alle gezellige momenten samen. Hoe waardevol je voor me bent en hoeveel steun ik bij je vind is iets wat dagelijks groeit en waar ik me over blijf verbazen.

Bart Vermeulen
Wageningen, November 2014

Summary

Rivers in tropical regions often challenge our geomorphological understanding of fluvial systems. Hairpin bends, natural scours, bifurcate meander bends, tie channels and embayments in the river bank are a few examples of features ubiquitous in tropical rivers. Existing observation techniques fall short to grasp the complex governing processes of flow and morphology. In this thesis new observational techniques are introduced and applied to study the Mahakam River, East Kalimantan, Indonesia. The observations reveal a new type of morphological regime, characterized by non-harmonic meanders, scour and strong variation of the cross-sectional area. The anomalous geometry induces a complex three-dimensional flow pattern causing longitudinal flow to be concentrated near the bed of the river.

In **Chapter 2** a wavelet based technique is introduced to characterize meander shape in a quantitative, objective manner. A scale space forest composed of a set of rooted trees represents the meandering planform. Based on the rooted trees, the locally dominant meander wavelengths are defined along the river. Sub-meander scale spectral density in the wavelet transform is used to determine a set of metrics quantifying bend skewness and fattening. Negative fattening parameterizes the so-called non-harmonic or hairpin bend character of meanders. The super-meander scale tree represents the embedding of meanders into larger-scale fluctuations, spanning from double-headed meander scales until the scale of the valley thalweg. The new approach is used to quantify the anomalous planform geometry of the Mahakam River in a comparison with the Red River and the Purus River.

The geometry of the Mahakam River is analyzed into more detail in [Chapter 3](#), where the highly curved non-harmonic meanders are related to deep scours in the river bed. A total of 35 scours is identified which exceed three times the average river depth, and four scours exceed the river depth over four times. The maximum scour depth strongly correlates with channel curvature and systematically occurs half a river width upstream of the bend apex. Most scours occur in a freely meandering zone of the river. A systematic reconnaissance of the river banks reveals a switch of erosion-deposition patterns at high curvature. Advancing banks normally observed at the inner side of a bend are mostly found at the outer side of high-curvature reaches, while eroding banks switch from the outer side for mildly curved bends to the inner side for bends with high curvature. The overall lateral migration rate of the river is low. These results indicate a switch of morphological regime at high curvatures, which requires detailed flow measurements to unravel the underlying physical processes.

Taking flow measurements in the deep scours of the Mahakam River presents a challenge to contemporary methods in hydrography. Acoustic Doppler Current Profilers (ADCPs) are capable of profiling flow velocity over large distances from a research vessel, but the existent data processing techniques assume homogeneity of the flow between the divergent acoustic beams. This assumption fails for complex three dimensional flows as found in the scours. In [Chapter 4](#) a new ADCP data processing technique is developed that strongly reduces the extent over which the flow needs to be assumed homogeneous. The new method is applied to flow measurements collected in a river bend with a scour exceeding 40 m depth. Results based on the new approach reveal secondary flow patterns which remain invisible adopting the conventional method.

[Chapter 5](#) aims to better understand flow in sharp bends, by combining analyses of the flow measurements from a deep scour with Large Eddy Simulations of the flow. The three-dimensional flow field is strongly dominated by horizontal circulations at both sides of the scour. The dramatic increase in cross-sectional area (from 2200 m² to 7000 m²) plays a crucial role in the generation of the two horizontal recirculation cells. An existing formulation to predict water surface gradients in bends is extended to include the effect of cross-sectional area variations, next to the effect of curvature changes. Variation in

the cross-sectional area develops adverse water surface gradients explaining the flow recirculation. The depth increase toward the scour causes a strong downward flow (up to 12 cm s^{-1}) creating a non-hydrostatic pressure distribution, steering the core of the flow toward the bed. The latter aspect is poorly reproduced by the Large Eddy Simulations, which may relate to the representation of turbulent shear stresses.

In **Chapter 6** a novel technique is introduced to better monitor turbulence properties in complex river flows from ADCP measurements, exploiting what is discarded in observations of the mean flow. It extends the so-called variance method, using two ADCPs instead of one. The availability of eight acoustic beams, four from each ADCP, changes an otherwise unsolvable set of equations with six unknowns into an overdetermined system of eight equations with six unknowns. This allows to solve for the complete Reynolds stress tensor, yielding profiles of Reynolds stresses over almost the entire water column. Widely applied assumptions on turbulence anisotropy ratios are shown to be incorrect, which reveals a knowledge gap in open channel turbulence.

Chapter 7 uses the technique developed in **Chapter 6** to investigate the degree in which bed shear stress can be monitored continuously from an ADCP mounted horizontally at the river bank (HADCP). A calibrated boundary layer model is applied to estimate time-series of cross-river bed-shear stress profiles from HADCP velocity measurements. It is concluded the HADCP measurement can represent the regional bed shear stresses, as inferred from a logarithmic velocity profile, reasonably well. These regional bed-shear stresses, in turn, poorly represent the local estimates obtained from coupled ADCP measurements, which are more directly related to processes of sediment transport and complex river morphology. Detailed observations of turbulence properties may be the key to improve our understanding of complex river flow and morphology.

Samenvatting

Tropische rivieren vormen een uitdaging voor ons geomorfologische begrip van rivieren. Haarspeldbochten, ontgrondingskuilen, splitsende rivierbochten en oever-inhammen zijn slechts een paar voorbeelden van veel voorkomende fenomenen in tropische rivieren. Bestaande meettechnieken zijn slecht in staat om de stroming en morfologische processen te observeren die deze fenomenen veroorzaken. In dit proefschrift worden nieuwe meettechnieken voorgesteld en toegepast op de Mahakam rivier, Oost Kalimantan, Indonesië. Uit de metingen blijkt dat de rivier morfologisch gedrag vertoont dat gekenmerkt wordt door niet-harmonische meanders, ontgrondingskuilen en sterke toename in doorstroomoppervlak. De afwijkende geometrie veroorzaakt een complexe drie-dimensionale stroming, waarbij de sterkste stroomsnelheden optreden dichtbij de rivierbodem.

In **Hoofdstuk 2** wordt een op wavelets gebaseerde techniek geïntroduceerd waarmee de vorm van meanders op een kwantitatieve en objectieve manier kan worden vastgesteld. De verschillende schalen in een meanderende vorm worden beschreven en gelokaliseerd met behulp van een boomstructuur. Op basis van de boomstructuur wordt de lokaal dominante meanderschaal bepaald langs de rivier. De spectrale dichtheid op kleinere schalen dan de meanderschaal vormen de basis voor een aantal parameters die de scheefheid en ronding van meanders beschrijven. Negatieve ronding komt overeen met niet-harmonische meanders, ook wel haarspeldbochten genoemd. De boomstructuur boven de meanderschaal beschrijft hoe meanderbochten deel uitmaken van grotere structuren, variërend van dubbele meanders tot de rivier schaal. De nieuwe methode kwantificeert de afwijkende vorm van de Mahakam Rivier in vergelijking met de Red River en de Rio Purus.

De geometrie van de rivier wordt nader onderzocht in **Hoofdstuk 3**, waarin scherpe, niet-harmonische bochten worden gerelateerd aan diepe ontgrondingskuilen. Vijfendertig kuilen blijken dieper te zijn dan drie keer de gemiddelde diepte en vier kuilen dieper dan vier keer de gemiddelde diepte. De diepte van de ontgrondingskuilen is sterk gecorreleerd met de kromming van de rivier. De maximum diepte wordt doorgaans bereikt op een halve rivierbreedte bovenstrooms van de maximale kromming. De meeste ontgrondingskuilen zijn gevonden in een gebied waarin de rivier vrij meandert. Een systematische verkenning van de rivieroever toont aan dat erosie- en sedimentatiepatronen omkeren bij sterk gekromde delen van de rivier. Waar sedimentatie meestal plaatsvindt in de binnenbocht, komt deze, voor sterk gekromde bochten, vooral voor in de buitenbocht. Het omgekeerde gebeurt voor erosie. Deze vindt meestal plaats in de buitenbocht, maar voor sterk gekromde bochten vooral in de binnenbocht. De laterale migratie van de rivier is beperkt. Deze resultaten tonen afwijkend morfologisch gedrag, waarvoor een fysische verklaring gevonden kan worden met behulp van detailmetingen van de stroming.

Het meten van de stroming in de diepe ontgrondingskuilen van de Mahakam is een uitdaging met de huidige technieken. Acoustic Doppler Current Profilers (ADCP's) meten profielen van de stroomsnelheid tot op grote afstand van de meetboot. Bestaande technieken voor het verwerken van de data gaan uit van homogeniteit in de stroming tussen de divergerende akoestische bundels. Deze aanname gaat niet op voor complexe drie-dimensionale stroming zoals in de ontgrondingskuilen. In **Hoofdstuk 4** wordt een nieuwe techniek ontwikkeld die het gebied waarover homogeniteit verondersteld wordt sterk reduceert. De nieuwe methode wordt toegepast op metingen die gedaan zijn in een rivierbocht met een ontgrondingskuil van meer dan 40 m diepte. De nieuwe methode maakt cellen van secundaire stroming zichtbaar die onopgemerkt zouden blijven met bestaande methodes.

Het doel van **Hoofdstuk 5** is een beter begrip te krijgen van de stroming door scherpe bochten, gebruik makend van stromingsmetingen en Large Eddy Simulations van de stroming. De stroming wordt sterk bepaald door twee horizontale recirculatiecellen aan weerszijden van de ontgrondingskuil. De sterke toename in doorstroomoppervlak (van 2200 m² tot 7000 m²) is van cruciaal belang voor het

ontstaan van de recirculatiecellen. Een bestaande formulering om de langsgradiënt van het wateroppervlak te bepalen is uitgebreid, zodanig dat het effect van veranderingen in doorstroomoppervlak wordt meegenomen, naast het effect van veranderingen in kromming. Verandering in doorstroomoppervlak veroorzaakt een tegengestelde gradiënt in het wateroppervlak. Dit verklaart het ontstaan van de recirculaties. De toename in waterdiepte richting de ontgrondingskuil veroorzaakt een neerwaartse stroming (met een maximum snelheid van 12 cm s^{-1}) die, op haar beurt, de hydrostatische drukverdeling verstoort waardoor de kern van de stroming zich concentreert nabij de bodem van de rivier. Dit mechanisme kan niet goed worden nagebootst met het model, hetgeen te maken zou kunnen hebben met de modellering van de turbulente schuifspanningen.

In **Hoofdstuk 6** wordt een nieuwe techniek geïntroduceerd die het mogelijk maakt om turbulentieeigenschappen van de stroming beter te observeren door gebruik te maken van data die bij het bepalen van de gemiddelde stroming worden uitgemiddeld. De zogenaamde variantie-methode wordt uitgebreid door twee ADCP's in plaats van één ADCP te gebruiken. De beschikbaarheid van acht akoestische bundels, vier voor elke ADCP, maakt dat een anders onderbepaald stelsel van vier vergelijkingen met 6 onbekenden verandert in een overbepaald stelsel van acht vergelijkingen met zes onbekenden. Hierdoor kunnen alle termen van de Reynolds spanningstensor opgelost worden, waardoor de metingen profielen van Reynolds spanningen opleveren over vrijwel de gehele waterkolom. Toepassing van de methode toont aan dat veelgebruikte aannames over de ratio's in turbulente anisotropie onjuist zijn, hetgeen duidt op een kennisleemte in de bestaande theorie van open-water turbulentie.

In **Hoofdstuk 7** wordt de methode ontwikkeld in **Hoofdstuk 6** gebruikt om te bepalen in hoeverre het mogelijk is om bodemschuifspanningen continu te monitoren met behulp van een aan de oever geplaatste horizontale ADCP (HADCP). Een gecalibreerd grenslaagmodel wordt toegepast om tijdreeksen van dwarsprofielen van bodemschuifspanning te bepalen. Metingen uit HADCP's geven een redelijk goede weergave van de regionale bodemschuifspanning, zoals bepaald uit gemiddelde snelheidsprofielen. De regionale bodemschuifspanningen komen, op hun beurt, slecht overeen met de lokale bodemschuifspanning, bepaald uit gekoppelde ADCP metingen, die

sterker gekoppeld blijken te zijn aan het lokale sedimenttransport en de daaraan gekoppelde complexe riviermorfologie. Gedetailleerde observaties van turbulentie eigenschappen zijn een mogelijke sleutel tot een beter begrip van complexe stroming en morfologie.



*Netherlands Research School for the
Socio-Economic and Natural Sciences of the Environment*

D I P L O M A

For specialised PhD training

The Netherlands Research School for the
Socio-Economic and Natural Sciences of the Environment
(SENSE) declares that

Bart Vermeulen

born on 30 December 1983 in Amersfoort, The Netherlands

has successfully fulfilled all requirements of the
Educational Programme of SENSE.

Wageningen, 8 December 2014

the Chairman of the SENSE board

Prof. dr. Huub Rijnaarts

the SENSE Director of Education

Dr. Ad van Dommelen

The SENSE Research School has been accredited by the Royal Netherlands Academy of Arts and Sciences (KNAW)



K O N I N K L I J K E N E D E R L A N D S E
A K A D E M I E V A N W E T E N S C H A P P E N



The SENSE Research School declares that Mr Bart Vermeulen has successfully fulfilled all requirements of the Educational PhD Programme of SENSE with a work load of 42.8 EC, including the following activities:

SENSE PhD Courses

- o Environmental Research in Context (2009)
- o Research Context Activity: Co-organising Symposium 'Role of laboratory experiments in water and sediment dynamics research', Wageningen (2010)

Other PhD and Advanced MSc Courses

- o Complex flows, turbulence, morphodynamics and ecology in rivers (2009)
- o High-Impact Writing Course (2013)

External training at a foreign research institute

- o Setting up SLIM numerical model, UCL Louvain-La-Neuve, Belgium (2010)

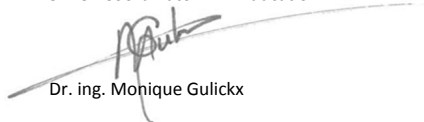
Management and Didactic Skills Training

- o Supervision four MSc and two BSc theses

Selection of oral Presentations

- o *Development of a finite-element, multi-scale model of the Mahakam Delta (Indonesia).* Joint Numerical Sea Modelling Group, 11 May 2010, Delft, The Netherlands
- o *Coupled ADCPs can yield complete Reynolds stress tensor profiles in geophysical surface flows.* SENSE symposium 'Modelling and observing earth system compartments', 22 February 2011, Wageningen, The Netherlands
- o *Measuring profiles of the Reynolds Stress Tensor with two coupled ADCPs.* River, Coastal and Estuarine Morphodynamics: RCEM, 5-7 September 2011, Beijing, China
- o *Sharp bends in the Mahakam River: A morphological analysis.* AGU Fall Meeting 2011, 1-5 December 2011, San Francisco, United States
- o *Attenuation in ADCP backscatter calibrations.* Hydraulic Measurements and Experimental Methods, 12-15 August 2012, Snowbird, United States
- o *Improved processing of vessel mounted ADCP data.* Netherlands Center for River studies Days (NCR-Days), 3-4 October 2013, Delft, The Netherlands

SENSE Coordinator PhD Education



Dr. ing. Monique Gulickx

This research was funded by NWO-WOTRO (WT76-269)

Cover design by:
too many words
www.toomanywords.nl



$$F = \frac{[\psi_s]_{max} \int_0^\pi \psi_s f_F \partial \phi}{[\psi_s]_{min} \int_0^\pi f_F^2 \partial \phi}$$